Chapter 1

Theory of neutrino physics

Neutrinos were first theoretically proposed by Wolfgang Pauli [1, 2] as very light electrically neutral particles with a half-integer spin and a possible magnetic moment [3]. They formed a crucial part of Enrico Fermi's successful theory of β decays [4, 5], which solidified their importance in particle physics even before their first experimental detection. Fermi's theory developed into the Standard Model (SM) of particle physics [6–8], which in its current form contains three generations of fermions. Each generation involves two leptons: one charged lepton and one neutrino, which has no mass, nor magnetic moment.

The SM is mathematically described by a Lagrangian, in which neutrinos are represented by a two-component left-handed chiral fields $\nu_{\alpha L}$, where $\alpha = e, \mu, \tau$ denotes the three neutrino generations, also called flavours [9–11]. Neutrino fields form weak isospin doublets $L_\alpha = \begin{pmatrix} \nu_{\alpha_L} \\ \alpha_L \end{pmatrix}$ with their associated left-handed charged lepton fields α_L. Unlike for the charged leptons, there is no right-handed chiral neutrino singlet field in the SM. This means that neutrinos cannot obtain a mass term, since the fermion mass terms arise from the Higgs mechanism [12–14] via the Yukawa coupling of the fermion and the Higgs fields[1] [15], which requires a combination of left-handed and right-handed chiral fields [16]. Additionally, since neutrinos are massless in the SM, all the neutrinos are left-handed helicity particles, and all the antineutrinos $(\overline{\nu})$ are right-handed helicity antiparticles. Therefore, neutrinos and antineutrinos are mutually related not only by a charge conjugation, but by a combined Charge conjugation - Parity (CP) symmetry: $\nu \xleftrightarrow{CP} \overline{\nu}$.

The interaction terms for neutrinos can be separated into two parts, describing the Charged Current (CC) interactions with the W_μ gauge field and the Neutral Current (NC) interaction with the Z_μ gauge field, which are coupled to the $W^\pm$ and Z^0 gauge

[1]Further discussion about possible neutrino mass terms in Sec. 1.4

bosons respectively. Neglecting the non-neutrino components, the two neutrino interaction terms are [16]

$$\mathcal{L}_{\text{CC}}^{\text{SM}} = -\frac{g_w}{\sqrt{2}} \sum_{\alpha=e,\mu,\tau} \overline{\nu}_{\alpha L} \gamma^{\mu} \alpha_L W_{\mu}^{+} + \text{h.c. and} \tag{1.1}$$

$$\mathcal{L}_{\text{NC}}^{\text{SM}} = -\frac{g_w}{2\cos(\theta_W)} \sum_{\alpha=e,\mu,\tau} \overline{\nu}_{\alpha L} \gamma^{\mu} \nu_{\alpha L} Z_{\mu}^{0}. \tag{1.2}$$

Here g_w is the weak coupling constant, θ_W is the Weinberg angle and γ^{μ} $(\mu = 0, 1, 2, 3)$ are the four Dirac gamma matrices. The $\overline{\nu}_{\alpha L}$ denotes the Dirac adjoint of $\nu_{\alpha L}$ and h.c. the hermitian conjugate. These two terms describe all the possible SM neutrino interaction vertices. Figure 1.1 shows the CC and the NC interaction of neutrinos and antineutrinos and, in case of the CC diagram, can also be flipped around the vertical axis to show the production of neutrinos from the weak interaction (or decays) of leptons. They can also be rotated $90°$ to either show the annihilation, or the production of the neutrino-lepton (for CC), or neutrino-antineutrino (for NC) pairs.

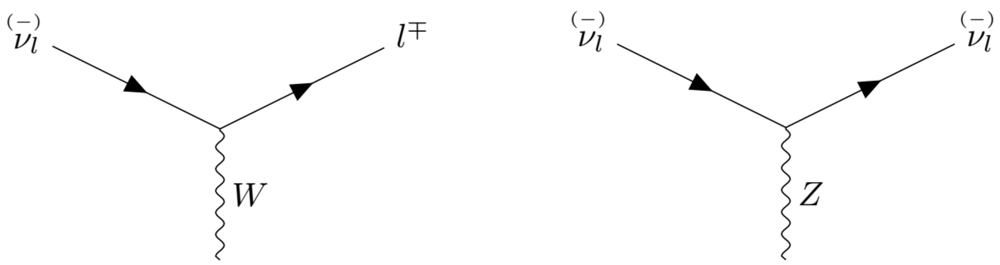

Figure 1.1: Neutrino interaction vertices in the SM via the weak charged currents (left) and the neutral currents (right).

1.1 Neutrino Production

Some of the most common neutrino and antineutrino production channels include nucleon transitions via CC weak interactions. Specifically, the transition of a neutron into a proton, either as the decay of a free neutron, or as the β^- decay for neutrons bound in nucleus, produces an electron and an electron antineutrino:

$$n \to p + e^- + \overline{\nu}_e. \tag{1.3}$$

The study of the electron spectrum from β^- decay was the reason Pauli proposed the existence of the neutrino [1]. Additionally, this channel is an abundant source of $\overline{\nu}_e$ from nuclear reactors, which were the first artificial sources of neutrinos, significantly increasing the flux of high energy neutrinos compared to the naturally occurring sources, thus enabling the first ever detection of a neutrino [17–19].

Similarly, the production of an electron neutrino together with a positron via the transition of a proton into a neutron can occur inside the nucleus either as the β^+ decay:

$$p \to n + e^+ + \nu_e, \tag{1.4}$$

or via the electron capture:

$$p + e^- \to n + \nu_e. \tag{1.5}$$

This channel occurs in stars and in the first phase of supernovae [16]. However, most supernovae neutrinos are created via a thermal pair production via NC interaction

$$e^- + e^+ \to \nu_\alpha + \overline{\nu}_\alpha \tag{1.6}$$

producing neutrinos and antineutrinos of all flavours. Neutrino pair production via the decay of Z^0 was studied in great detail [20], since the magnitude of the Z^0 decay width depends on the number of neutrino flavours (N_ν) that can couple to Z^0, with the current best fit $N_\nu = 2.9840 \pm 0082$ [21]. Therefore, there should be exactly three light active neutrino flavours.

An abundant source of ν_μ and $\overline{\nu}_\mu$ is the decay of pions and muons

$$p + X \to \pi^\pm \to \mu^\pm + \nu_\mu \left(\overline{\nu}_\mu\right) \tag{1.7}$$

$$\mu^\pm \to e^\pm + \overline{\nu}_\mu \left(\nu_\mu\right) + \nu_e \left(\overline{\nu}_e\right), \tag{1.8}$$

which naturally occurs in Earth's atmosphere from the interaction of cosmic ray protons. It is notable, that if all the muons decay by the time they reach Earth's surface, the ratio of $(\nu_\mu + \overline{\nu}_\mu) : (\nu_e + \overline{\nu}_e)$ should be exactly 2:1. The same process is also used in the modern accelerator-based neutrino sources, which use protons from accelerators with desired energies, impinge them onto a fixed target, and focus the resulting hadrons (mostly π) to achieve a highly pure and precise source of ν_μ or $\overline{\nu}_\mu$ [22, 23].

Heavier hadrons, such as kaons and charmed particles, can be produced from accelerated protons and other particles, either from natural or artificial origins. These hadrons then also produce neutrinos, including ν_τ and $\overline{\nu}_\tau$ if their energies are high enough [24, 25].

1.2 Neutrino Interactions

The interaction of neutrinos with matter can either be categorized based on the target, which is generally either an atomic electron or a nucleus, or the neutrino energy.

Neutrino-electron interactions occur either via elastic scattering, which result in a neutrino and an electron, or via the inverse muon (or tau) decay, which contains a muon (or tau) in the final state. Both of these interactions at the lowest order involve only free leptons and are very well understood theoretically. The elastic scattering has no energy threshold and can occur for any neutrino. On the other hand, due to the large difference between m_e and m_μ/m_τ, the inverse muon decay has an energy threshold of $E_{\nu_\mu} > 10.92\,\mathrm{GeV}$, and the inverse tau decay $E_{\nu_\tau} > 3\,\mathrm{TeV}$ [16, 26].

Neutrino-nucleus interactions can be, to an extent, approximated by the interaction of a neutrino with quasi-free nucleons inside the nucleus [27]. These interactions can be separated into different interaction channels based on what happens to the nucleon and therefore on the resulting particles. The interaction channels depend on the neutrino incident energy, as illustrated on the case of ν_μ CC interactions in Fig. 1.2.

At lower energies, neutrino-nucleon interactions result in the production of either a nucleon together with a neutrino in the case of NC elastic scattering, or a nucleon with a charged lepton in the case of CC Quasi-Elastic (QE) interactions. The CCQE interaction of an antineutrino on a proton

$$\overline{\nu}_\alpha + p \rightarrow n + \alpha^+ \tag{1.9}$$

is called the inverse β decay and was used for the first ever detection of neutrinos (specifically $\overline{\nu}_e$ from a nuclear reactor) [17, 18]. Together with the interaction of a neutrino on a neutron

$$\nu_\alpha + n \rightarrow p + \alpha^- \tag{1.10}$$

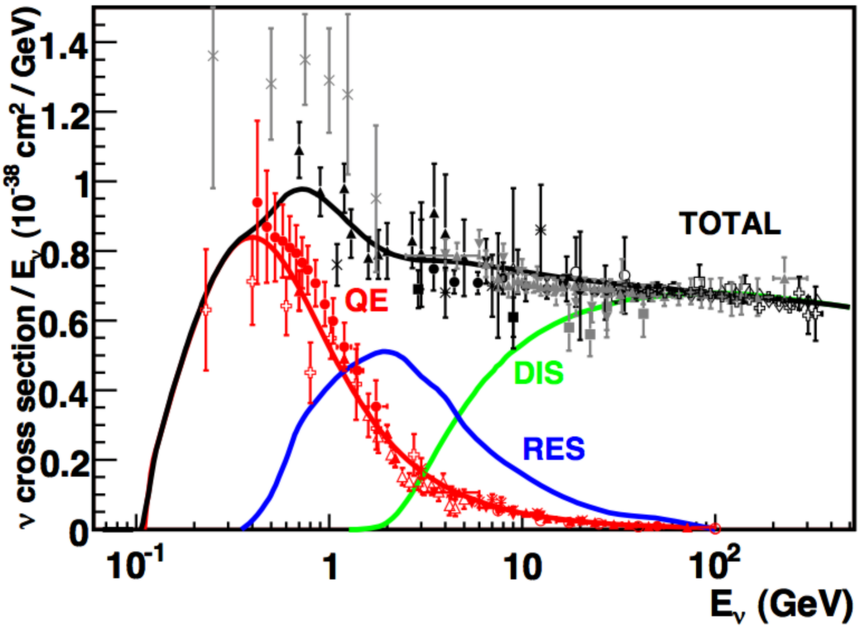

Figure 1.2: Neutrino CC cross sections on an isolated nucleon divided by the neutrino energy based on the interaction types: Quasi-Elastic (QE), Resonant baryon production (Res) and Deep Inelastic Scattering (DIS). Figure is from [28] and compares the measured data [27] and the prediction provided by the NUANCE generator [29].

they serve as fundamental processes for neutrino detection [24, 30, 31]. There is no low energy threshold for the ν_e CCQE interaction, however, there is a threshold for $\overline{\nu}_e$: $E_{\overline{\nu}_e} \gtrsim 1.8\,\mathrm{MeV}$ and for the other neutrino and antineutrino flavours: $E_{\nu_\mu} \gtrsim 110\,\mathrm{MeV}$ and $E_{\nu_\tau} \gtrsim 3.5\,\mathrm{GeV}$.

At higher energies, neutrinos can transfer enough energy to the outgoing nucleon to excite it into a resonant baryon, which then decays back into the original nucleon and into one or more additional particles. This Resonant baryon production (Res) has a threshold of about $270\,\mathrm{MeV}$ for ν_μ and can be distinguished by the presence of an additional π on top of the CCQE products, or, at higher energies, even of multiple additional π's or other hadrons. Increasing the neutrino incident energy even higher means that neutrinos can start probing the quark contents of the individual nucleons in the Deep Inelastic Scattering (DIS), as can be seen in Fig. 1.2.

Even though the approximation of nuclei as collections of quasi-free nucleons is useful, it has been shown [32] there are important nuclear effects that have to be considered. For example the Fermi motion of nucleons and their binding inside the nucleus, or Pauli's exclusion principle resulting in nucleon energy levels [33]. Another important example is the two particle - two hole (2p2h) interaction [34–36], which occurs when neutrinos interact with a correlated pair of nucleons and can significantly increase the QE cross section [33]. The 2p2h interaction often occurs via the Meson Exchange Current (MEC), where the meson effectively propagates the interaction between the two correlated nucleons. Furthermore, the products of all of the aforementioned interactions can re-interact inside of the nucleus in Final State Interactions (FSIs), which can alter the particle content observed in the detector.

Additionally, if the total energy transferred to the nucleus is small neutrinos can interact with the entire nucleus coherently, where the contributions from each individual nucleon are added together. At low energies, neutrinos can interact via the Coherent Elastic ν-Nucleus Scattering (CEvNS) [37], which results in the excitation of the nucleus. At higher energies, neutrinos can interact via the Coherent π (COHπ) production, which produces a single π without transferring much momentum to the nucleus. In case of the NCCOHπ production the produced π is neutral and for the CCCOHπ there is an additional charged lepton and the produced π is positive (negative) for (anti)neutrinos. As the produced π receives most of the transferred momentum from the neutrinos, it generally travels in the same direction as the initial neutrino and can be difficult to distinguish, especially from e and γ signals in a detector [33].

1.3 Neutrino Oscillation

The idea that neutrinos can oscillate originates as a possibility of transitions between neutrinos and antineutrinos [38, 39], analogically to the already known oscillations of $K^0 \leftrightarrow \overline{K^0}$. This was adapted to the oscillations between different neutrino flavours [40, 41], by considering that the flavour neutrino states ν_α, which are the eigenstates of weak interactions described in Eq. 1.1 and 1.2, are not identical to the mass neutrino states ν_k, which are the eigenstates of the vacuum Hamiltonian $\mathcal{H}_0$:

$$\mathcal{H}_0 \left|\nu_k\right\rangle = E_k \left|\nu_k\right\rangle, k = 1, 2, 3, ..., \tag{1.11}$$

with energy E_k. Instead, the neutrino flavour and mass eigenstates are related as

$$\left|\nu_\alpha\right\rangle = \sum_k U^*_{\alpha k} \left|\nu_k\right\rangle, \tag{1.12}$$

where U is the Pontecorvo-Maki-Nakagawa-Sakata (PMNS) matrix, named after the authors [16, 42]. U is defined as unitary, which makes the inverse relation simply

$$|\nu_k\rangle = \sum_{\alpha} U_{\alpha k} |\nu_\alpha\rangle . \tag{1.13}$$

Using the Schrödinger equation

$$i\frac{d}{dt} |\nu_k(t)\rangle = \mathcal{H} |\nu_k(t)\rangle , \tag{1.14}$$

the evolution of massive neutrino states in vacuum ($\mathcal{H} = \mathcal{H}_0$) can be described by plane waves

$$|\nu_k(t)\rangle = e^{-iE_k t} |\nu_k\rangle . \tag{1.15}$$

The energy of a neutrino state with mass m_k and momentum $\overrightarrow{p}$

$$E_k = \sqrt{\overrightarrow{p}^2 + m_k^2} \tag{1.16}$$

can be approximated as

$$E_k \xrightarrow{m^2 \ll p^2 \approx E^2} E + \frac{m_k^2}{2E}, \tag{1.17}$$

assuming small neutrinos masses and for ultra-relativistic neutrinos [16]. Additionally, as it is generally easier to measure the distance neutrinos travel (L), rather than the time (t), and given the notation $c \equiv 1$, where c is the speed of light in vacuum, it is common to interchange $L \leftrightarrow t$.

Given the orthogonality of neutrino states, $\langle \nu_k | \nu_j \rangle = \delta_{kj}$ and $\langle \nu_\alpha | \nu_\beta \rangle = \delta_{\alpha\beta}$, and using Eq. 1.15, 1.12 and 1.13, the amplitude of the oscillation (transition) from $\nu_\alpha \to \nu_\beta$ over the 'baseline' L can be written as

$$A_{\nu_\alpha \to \nu_\beta}(L) \equiv \langle \nu_\beta | \nu_\alpha(L) \rangle = \sum_k U_{\alpha k}^* U_{\beta k} e^{-iE_k L} \tag{1.18}$$

and the probability as

$$P_{\nu_\alpha \to \nu_\beta}(L) = \left| A_{\nu_\alpha \to \nu_\beta}(L) \right|^2 = \sum_{k,j} U_{\alpha k}^* U_{\beta k} U_{\alpha j} U_{\beta j}^* e^{-i(E_k - E_j)L}. \tag{1.19}$$

Using Eq. 1.17 and by defining the neutrino mass splitting (also called the mass squared difference) as

$$\Delta m_{kj}^2 \equiv m_k^2 - m_j^2, \tag{1.20}$$

the oscillation probability can be expressed as

$$P_{\nu_\alpha \to \nu_\beta}(L) = \sum_{k,j} U_{\alpha k}^* U_{\beta j} U_{\alpha j} U_{\beta j}^* e^{-i\frac{\Delta m_{kj}^2 L}{2E}}. \tag{1.21}$$

So far no assumption has been made as to the specific number of neutrino mass or flavour states. However, as was described above in Sec. 1.1, from the decay of Z^0 we know there are probably exactly three active neutrino flavour states, ν_e, ν_μ and ν_τ. Consequently, it is common to also consider exactly three neutrino mass states. This is often called the three neutrino paradigm. Therefore, the PMNS matrix can be written as [16]:

$$U = \begin{pmatrix} U_{e1} & U_{e2} & U_{e3} \\ U_{\mu 1} & U_{\mu 2} & U_{\mu 3} \\ U_{\tau 1} & U_{\tau 2} & U_{\tau 3} \end{pmatrix} =$$

$$= \begin{pmatrix} 1 & 0 & 0 \\ 0 & c_{23} & s_{23} \\ 0 & -s_{23} & c_{23} \end{pmatrix} \begin{pmatrix} c_{13} & 0 & s_{13}e^{-i\delta} \\ 0 & 1 & 0 \\ -s_{13}e^{i\delta} & 0 & c_{13} \end{pmatrix} \begin{pmatrix} c_{12} & s_{12} & 0 \\ -s_{12} & c_{12} & 0 \\ 0 & 0 & 1 \end{pmatrix}, \tag{1.22}$$

where $c_{ij} \equiv \cos\theta_{ij}$ and $s_{ij} \equiv \sin\theta_{ij}$. The matrix is parametrized using three mixing angles θ_{12}, θ_{13} ,and θ_{23} and one phase[2], often denoted δ_{CP}. This phase describes a possible CP symmetry violation in neutrino oscillations, which would result in a difference between the neutrino and antineutrino oscillation probabilities.

When neutrinos pass through matter, their evolution changes due to coherent elastic CC and NC scattering. However, since the NC scattering affects all neutrino flavours equivalently, it does not have any effect on neutrino oscillations. Additionally, as electrons are the only charged leptons present in matter, only the relative difference between the CC interactions of ν_e and of the other flavours needs to be considered. The effective interaction potential of neutrinos passing through matter

[2] If neutrinos are Majorana particles, they can have two additional phases, which however do not enter into neutrino oscillation probabilities

with an electron density N_e can be written as

$$V_{\mathrm{CC}} = \pm\sqrt{2}G_F N_e. \tag{1.23}$$

Here G_F is the Fermi coupling constant and the plus or minus sign is for neutrinos or antineutrinos respectively. The electron density (and therefore the interaction potential) can change along the neutrino path, as it does in the Sun, which can resonantly increase the probability of oscillations, as described by the Mikheyev-Smirnov-Wolfenstein (MSW) effect [43, 44]. However, in accelerator based experiments, where neutrinos only pass through the surface of the Earth, the N_e can be approximated as a constant.

The effect of neutrinos passing through matter on oscillation probabilities can be expressed as shifts to mixing angles and to mass squared differences, proportional to the V_{CC}. Since the matter effect differs for neutrinos and antineutrinos, it needs to be carefully considered especially for the δ_{CP} measurement, which relies on the comparison of neutrino to antineutrino oscillations [16].

The first experimental signs of neutrino oscillations appeared as an apparent deficit of solar neutrinos compared to their predicted flux [30]. However, due to low confidence in the prediction of the solar neutrino flux, no conclusion could have been drawn. Similarly, experiments measuring atmospheric neutrinos [45–48] saw a disagreement between the measurement and the prediction for the $\nu_\mu : \nu_e$ fraction of the atmospheric neutrino flux. This *atmospheric neutrino anomaly* was finally resolved by the Super-Kamiokande (SK) experiment [49], reporting the first experimental evidence for neutrino oscillations. The *solar neutrino anomaly* was resolved shortly after by the Sudbury Neutrino Observatory (SNO) experiment [50], which compared the NC rate, unaffected by neutrino oscillations, to the rate of CC neutrino interactions. This was proof that solar neutrinos oscillate without reliance on the model of the Sun. This result also confirmed the importance of accounting for the matter effect in neutrino oscillations, especially for the oscillation of solar neutrinos, due to the large matter density in the Sun.

The difference between the frequency of solar neutrino oscillations and that observed in atmospheric neutrinos proves that there are at least two mass splittings governing neutrino oscillations. As a result, there must be at least three separate neutrino mass states, with at least two of them possessing non-zero masses. This is in direct contradiction to the SM and is to-date the only laboratory-based observation of physics Beyond Standard Model (BSM) [51].

Currently, the three neutrino paradigm of oscillations between three neutrino flavour states via three neutrino mass states is well established [52, 53]. The magnitudes of both the neutrino mass splittings and of two mixing angles, θ_{12} and θ_{13}, are measured within 3%. The third mixing angle θ_{23} is measured to be close to the maximum mixing value of $45°$. However, there are three main questions yet to be determined for neutrino oscillations [51]:

1. What is the sign of the larger neutrino mass splitting? Is the electron neutrino made up of the lightest neutrino mass states (normal ordering), or the heaviest (inverted ordering)?

2. Is $\theta_{23} < 45°$ or $\theta_{23} > 45°$? These two options determine the $\nu_\mu : \nu_\tau$ relative contributions to the neutrino mass states and are also referred to as the upper and the lower octant respectively.

3. Is there CP violation in neutrino oscillations? What is the value of δ_{CP}? If neutrinos oscillate differently than antineutrinos, this could be an important part of the matter-antimatter asymmetry in the Universe.

All three of these questions are jointly investigated in the current Long Baseline (LBL) accelerator neutrino oscillation experiments, namely the NuMI Off-axis ν_e Appearance (NOvA) [54] and the Tokai to Kamioka (T2K) [55] experiments. Both use precise ν_μ and $\overline{\nu}_\mu$ beams, affected by the matter effect, and compare the rates of ν_μ and $\overline{\nu}_\mu$ disappearance and ν_e and $\overline{\nu}_e$ appearance to constrain neutrino oscillation parameters [51]. The same methods will be used in the next generation LBL neutrino oscillation experiments, namely the Deep Underground Neutrino Experiment (DUNE) [56] and the Hyper-Kamiokande (HK) [57] experiment, which should give the final answers to all three neutrino oscillation questions [51].

1.4 Neutrino Mass

The absolute values of neutrino masses are currently not known and cannot be directly measured in neutrino oscillation experiments. However, results from experiments measuring the kinematic distribution of β decays [58], or from cosmology [59], currently set a limit for each neutrino mass to $< 1\,\mathrm{eV}$. This is several orders of magnitude smaller than the charged fermion masses, suggesting that BSM theories which introduce neutrino masses should have a different mechanism for their generation than the one used for the other fermions [52]. Furthermore, in order to introduce neutrino masses into the SM, it is necessary to either add new fields, break the renormalizability of the SM Lagrangian, or do both [42]. Also, massive neutrinos can no longer be described by Weyl spinors

The most straight-forward solution, often called the *minimally extended SM*, is to add the missing right-handed chiral neutrino fields, which would enable neutrino mass generation through Yukawa couplings with the Higgs field. These right-handed fields would however be singlets under all the SM gauge symmetries and would therefore not participate in any of the SM interactions. Neutrinos created by these fields are called *sterile* and could potentially mix with the *active* neutrinos via neutrino oscillations. There are however a few issues with the minimally extended SM. Since the mass generation mechanism is the same as for the charged fermions, there is no theoretical explanation for the relative smallness of neutrino masses. There is also currently no experimental confirmation of oscillations between active and sterile neutrinos [52], although there are some possible indications [60, 61]. Additionally, having to add new fields by hand makes the SM an incorrect description of reality even at low energies. This is an issue, as it is generally believed that SM is at least a good low energy effective theory of a more complex general theory and only breaks down at some New Physics (NP) threshold value Λ_{NP} [62].

Adding new non-renormalizable terms to the SM Lagrangian, which are suppressed by this NP scale as $1/\Lambda_{NP}$, would maintain the renormalizability (and validity) of the SM at energies well below Λ_{NP} [62]. It is possible to create such a term using only the existing SM fields and preserving the SM gauge symmetries, which after spontaneous symmetry breaking generates neutrino mass terms. Additionally, three of the newly generated masses are also suppressed as $1/\Lambda_{NP}$ and belong to mostly left-handed (active) fields, while the rest are very large ($\sim \Lambda_{NP}$) and belong to mostly sterile neutrinos, which are therefore also called Heavy Neutral Leptons (HNLs). This is called the see-saw mechanism [63] and provides a natural explanation for the smallness of neutrino masses. Furthermore, the large masses of HNL make them more likely to avoid experimental detection. However, neutrinos with masses produced by this mechanism all have to be Majorana particles [64].

If neutrinos are Majorana particles, they are equivalent to their own antiparticles (via charge conjugation). The particles described as antineutrinos in the previous sections are however still different to neutrinos, although for Majorana neutrinos they only differ by parity transformation. Therefore, Majorana neutrinos and antineutrinos can be seen as two different spin states of a two-state 'Majorana particle'. This is in contrast to neutrinos being Dirac particles, which have four independent states (neutrino/antineutrino, each with two independent spin states), same as the other fermions and as in the minimally extended SM [16]. It is possible for neutrinos to be Majorana particles as they have no electric charge. However, all the other additive quantum numbers, including the total lepton number, must vanish for Majorana neutrinos as well. This means that Majorana neutrinos can effectively annihilate with each other, violating the total lepton number by two units.

A sure way of finding out whether neutrinos are Majorana particles or not is an observation of a neutrino-less double β decay [62]. This is currently a subject of an extensive experimental investigation without a concrete conclusion [52]. Neutrinos being Majorana particles does not affect neutrino oscillations, however, other measurements could probe the nature of neutrinos, or possible theories BSM, such as the measurements of the possible neutrino magnetic moment [51].

Chapter 2

The NOvA experiment

The NOvA [65] is a long-baseline neutrino oscillation experiment based at the Fermi National Accelerator Laboratory (Fermilab) [66]. NOvA receives an off-axis ν_μ and $\overline{\nu}_\mu$ beam from Fermilab's Neutrinos from the Main Injector (NuMI) neutrino source (Sec. 2.1) and measures the ν_e or $\overline{\nu}_e$ appearance and the ν_μ or $\overline{\nu}_\mu$ disappearance between its two highly active and finely segmented detectors (Sec. 2.4) [67].

The capability to measure both the ν_e and the $\overline{\nu}_e$ appearance, coupled with a significant matter effect induced by its long baseline, allows NOvA to address some of the most important questions in neutrino physics to date, such as the neutrino mass ordering, the octant of θ_{23}, and the possible CP symmetry violation in the neutrino sector [54, 67–70]. NOvA data also enables measurements of θ_{13}, θ_{23} and $|\Delta m^2_{32}|$ [67], measurements of neutrino differential cross sections in the Near Detector (ND) [71–74], constraints on the possible sterile neutrino models [75, 76], monitoring for supernova neutrino activity [77, 78], searches for magnetic monopoles [79], or constraints on the neutrino electromagnetic properties (this thesis). Using two functionally identical detectors mitigates the dominant systematic uncertainties of neutrino oscillation measurements, described in Sec. 2.8.

NOvA started taking data in February 2014 and is expected to run through 2026 [80], or until Fermilab begins redirecting its efforts towards the startup of the upcoming DUNE experiment [81].

2.1 The Neutrino Beam

The neutrino beam for NOvA comes from the Fermilab-based NuMI neutrino source [82]. The schematic description of NuMI is shown in Fig. 2.1, starting on the left hand side with $120\,\mathrm{GeV}$ protons from the Main Injector (MI), part of the Fermilab accelerator complex. The proton beam is divided into $10\,\mu\mathrm{s}$ long pulses, with $\sim 5 \times 10^{13}$

Protons On Target (POT) per spill every $\sim 1.3\,\mathrm{s}$ long cycle time, resulting in a proton beam power of $\sim 800\,\mathrm{kW}$ (current record $959\,\mathrm{kW}$ [83]), with upgrades currently underway to surpass $1\,\mathrm{MW}$ [84].

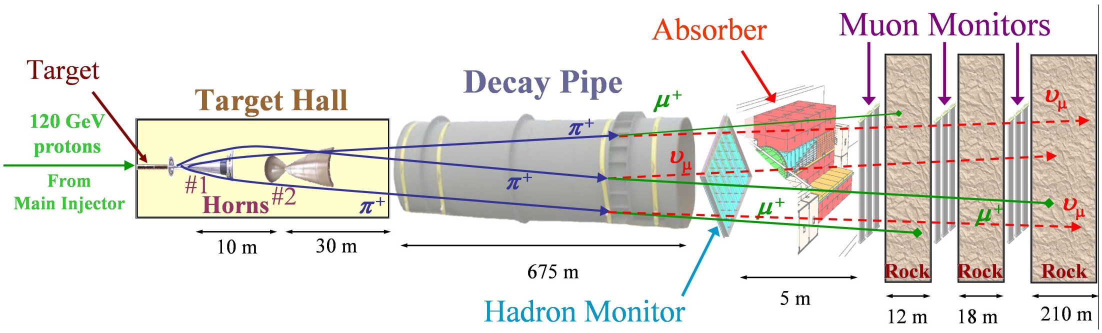

Figure 2.1: The NuMI neutrino beam starts on the left hand side with protons from the MI impinged on a graphite target producing mainly pions and kaons. These are then focused and charge-selected by two focusing horns, after which they decay inside the decay pipe into a high-purity ν_μ or $\overline{\nu}_\mu$ beam. The residual hadrons are stopped and monitored in the hadron absorber and the remaining muons are recorded with muon monitors and absorbed inside the rock. Figure from [82].

The proton beam passes through a collimating baffle before hitting a $\sim 1.2\,\mathrm{m}$-long (equal to about two interaction lengths) graphite target [85], producing hadrons, predominantly pions and kaons [82]. These are then focused and selected by two parabolic magnetic ‘horns’. The focused hadrons pass through a $675\,\mathrm{m}$-long decay pipe filled with helium to create a low density environment for hadrons to propagate and decay in flight into either neutrinos or antineutrinos. High energy hadrons that do not decay in the decay pipe are absorbed within a massive aluminium, steel, and concrete hadron absorber and monitored with a hadron monitor. The leftover muons are ranged out in dolomite rock after the absorber and monitored using three muon monitors. The hadron and muon monitors are ionization chambers, used to monitor the quality, location and relative intensity of the beam.

Using a positive current inside the horns focuses positively charged particles, which then decay into neutrinos, and removes negatively charged particles. Reversing the horn current focuses negatively charged particles, which decay into antineutrinos, and defocuses positively charged particles. The neutrino mode is therefore called Forward Horn Current (FHC) and the antineutrino mode is called Reverse Horn Current (RHC). The composition of the neutrino beam for both these modes at the NOvA ND is shown in Fig. 2.2, displaying the very high purity of the ν_μ or $\overline{\nu}_\mu$

component in the FHC ro RHC beam respectively [82].

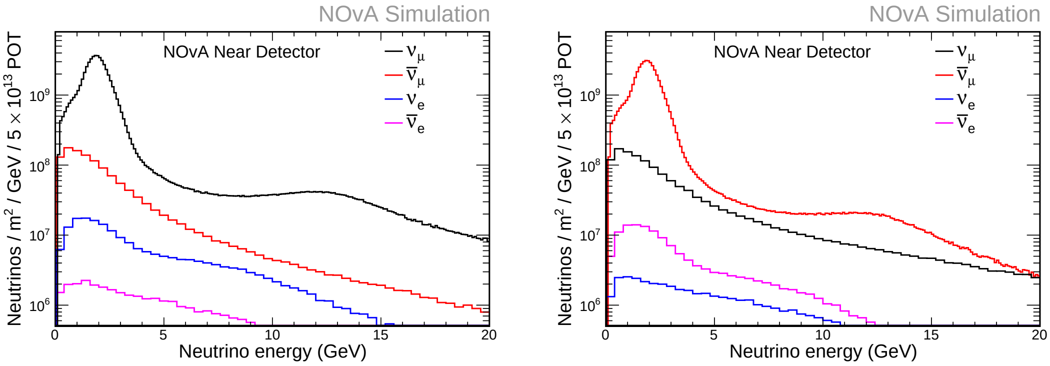

Figure 2.2: The components of the neutrino beam at the NOvA ND per one NuMI spill in the FHC regime shown on the left and the RHC regime on the right. The ν_μ ($\overline{\nu}_\mu$) composition in the FHC (RHC) regime is 93.8% (92.5%), with a wrong sign contribution of 5.3% (6.6%) and only 0.9% (0.9%) contamination by ν_e ($\overline{\nu}_e$), showing the high purity of ν_μ and $\overline{\nu}_\mu$ in the neutrino beam for NOvA. Beam composition values calculated for neutrinos with energies between $1-5\,\mathrm{GeV}$. Figures are from internal NOvA repository [86].

The resulting neutrino beam energy distribution is peaked at $\sim\ 7\,\mathrm{GeV}$ with a wide energy band. However, thanks to the kinematics of the dominant pion decay, by placing the NOvA ND and Far Detector (FD) $14.6\,\mathrm{mrad}$ ($\approx\ 0.8\,^\circ$) off the main NuMI beam axis, NOvA achieves a narrow band neutrino flux peaked at $1.8\,\mathrm{GeV}$ [54, 87], as can be seen in Fig. 2.3. Using an off-axis neutrino flux increases the neutrino beam around $2\,\mathrm{GeV}$ about 5-fold compared to the on-axis flux and narrow-band peak enhances background rejection for the ν_e appearance analysis [87].

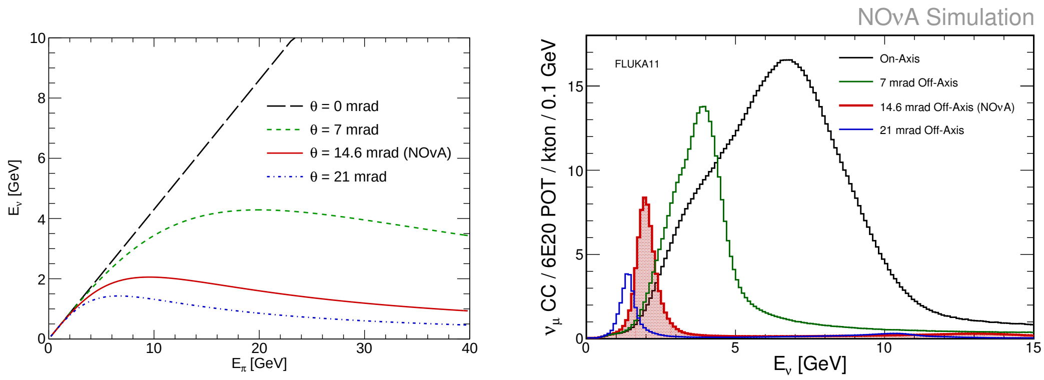

Figure 2.3: (Left) Dependence of the neutrino energy on the parent pion's energy and (right) neutrino energy distribution for an on-axis beam and three different off-axis beam designs. The case for NOvA is shown in red and results in a narrow neutrino energy distribution around $2\,\mathrm{GeV}$, with limited dependence on the parent pion's energy. Figure from [87]

2.2 The NOvA Detectors

The two main NOvA detectors are the ND, located in Fermilab $\sim$ 1 km from the NuMI target and $\sim$ 100 m under ground, and the FD, located $\sim$ 810 km from Fermilab at Ash River in north Minnesota, partially underground with a rock overburden [87]. NOvA also operated a detector prototype called Near Detector on the Surface (NDOS), which was used for early research and development of detector components and analysis [68]. Additionally, NOvA operated a Test Beam detector, described in detail in Sec. **??**. The scales of the ND and FD are shown in Fig. 2.4.

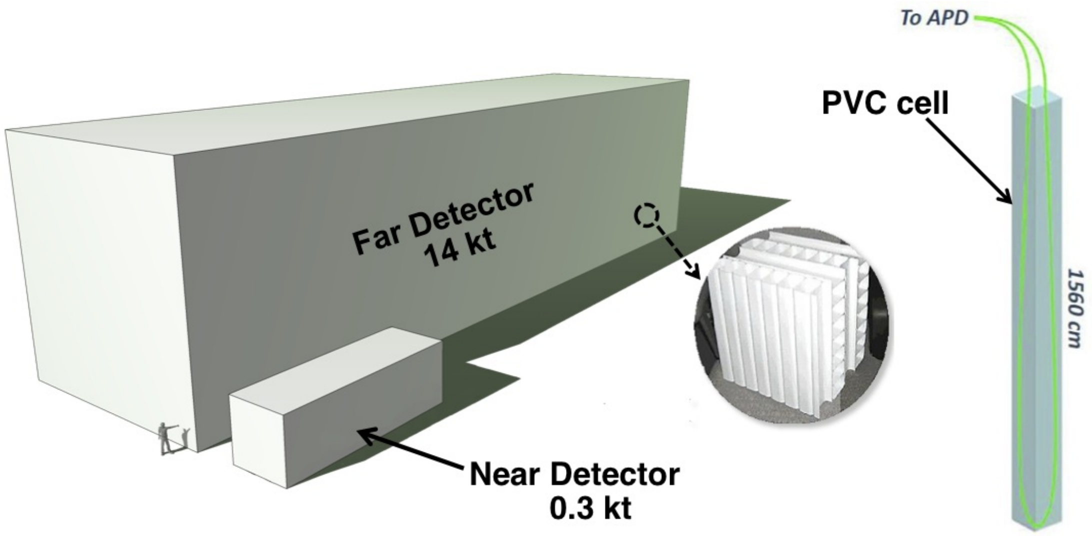

Figure 2.4: Schematic description of the scale and composition of the NOvA ND and FD. The inset shows a photo of the orthogonal planes made out of PVC cells. An example of a FD cell containing liquid scintillator and a looped WLS fibre attached to an APD is shown on the right [88].

All NOvA detectors are highly segmented, highly active, functionally identical tracking calorimeters made up of Polyvinyl chloride (PVC) cells filled with liquid scintillator. Each cell is a long rectangular cuboid with depth of 5.9 cm and width of 3.8 cm (with some variations), with cell length extending to the full width/height of each detector, which is $\sim$ 4.1 m for the ND and $\sim$ 15.6 m for the FD [87]. An example of a FD cell is shown on the right of Fig. 2.4.

Cells are connected side-by-side into a 16 cell-wide extrusions with 3.3 mm-wide walls between cells and 4.9 mm-wide walls on the outsides of the extrusions. The first and last cell of each extrusion are $\sim$ 3 mm narrower than the rest of the cells. Two extrusions are connected side-by-side to form a 32 cell-wide module, with each module having a separate readout (see Sec. 2.3). In the FD, 12 modules are connected side-by-side to form one plane of the detector. In the ND only 3 modules make up a plane. Planes are positioned one after another, alternating between vertical and horizontal orientation, and grouped into diblocks, each containing 64 planes. The FD contains 14 diblocks, totalling 896 planes, whereas the ND contains 3 diblocks totalling 192 planes. The ND also contains a Muon Catcher region, positioned right after the active region, consisting of 22 planes of the normal NOvA detector design, 2 modules high and 3 modules wide, sandwiched with 10 steel plates to help range out muons mainly from the ν_μ charged current interactions [68, 87].

The NOvA coordinate system is centred with $(0, 0, 0)$ in the centre of the first plane, relative to the beam direction. The x axis runs from left to right when facing the detector, y axis from bottom to top and z axis runs perpendicular to the planes along the beam direction.

Each cell is filled with a liquid scintillator consisting of mineral oil with 4.1% pseudocumene as the scintillant [89]. Each cell contains a single wavelength shifting fibre with double the length of the cell, looping at one end and connecting to the readout at the other. The PVC walls of the cells are loaded with highly reflective titanium dioxide, with light typically bouncing off the PVC walls ~ 8 times before being captured by the Wavelength Shifting (WLS) fibre [87].

The final dimensions of the FD are $15.6\,\mathrm{m} \times 15.6\,\mathrm{m} \times 60\,\mathrm{m}$ with a total mass of $14\,\mathrm{kT}$ and for the ND the dimensions are $3.8\,\mathrm{m} \times 3.8\,\mathrm{m} \times 12.8\,\mathrm{m}$ with a mass of about $0.3\,\mathrm{kT}$ [80]. The active volume, consisting only of the liquid scintillator without the PVC structure, makes up about 70% of the total detector volume [87].

The NOvA detectors are specifically designed for electromagnetic shower identification, with a radiation length of $38\,\mathrm{cm}$, which amounts to ~ 7 planes for particles travelling perpendicular to the detector planes [68]. This is particularly useful to distinguish electrons from π^0s.

We can calculate the minimum energy an electron needs to have to cross one cell ($5.9\,\mathrm{cm}$) of the NOvA detector by using the measured scintillator density $0.86\,\mathrm{g/cm^3}$ [90], which gives us the required range of $\sim 5\,\mathrm{g/cm^2}$. Comparing this to measured values for the electron range [91] in the continuous slowing down approximation in a Polyethylene (approximation of the NOvA scintillator [92]), gives us an estimate of the lowest detectable electron energy as $E_e \gtrsim 10\,\mathrm{MeV}$.

2.3 Readout and Data Acquisition

The signal from the WLS fibres is read out by an Avalanche Photodiode (APD), converting the scintillation light into electrical signal, with a high quantum efficiency of $\sim 85\%$ and a gain of 100 [87]. An example APD is shown in Fig. 2.5. Both ends of each fibre correspond to a single readout channel and are connected to one of the 32 pixels on the APD, organized in four rows of 8 pixels, with each APD reading out signal from one module. To maximise the signal to noise ratio, the APDs are cooled to $-15\,^{\circ}\mathrm{C}$ by a thermoelectric cooler, with heat carried away by a water cooling system.

The combination of the APD quantum efficiency and the light yield, determined by the PVC reflectivity and the scintillator and WLS fibre responses, result in a signal requirement of at least 20 Photo Electron (PE) in response to minimum ionizing radiation at the far end of the FD cell.

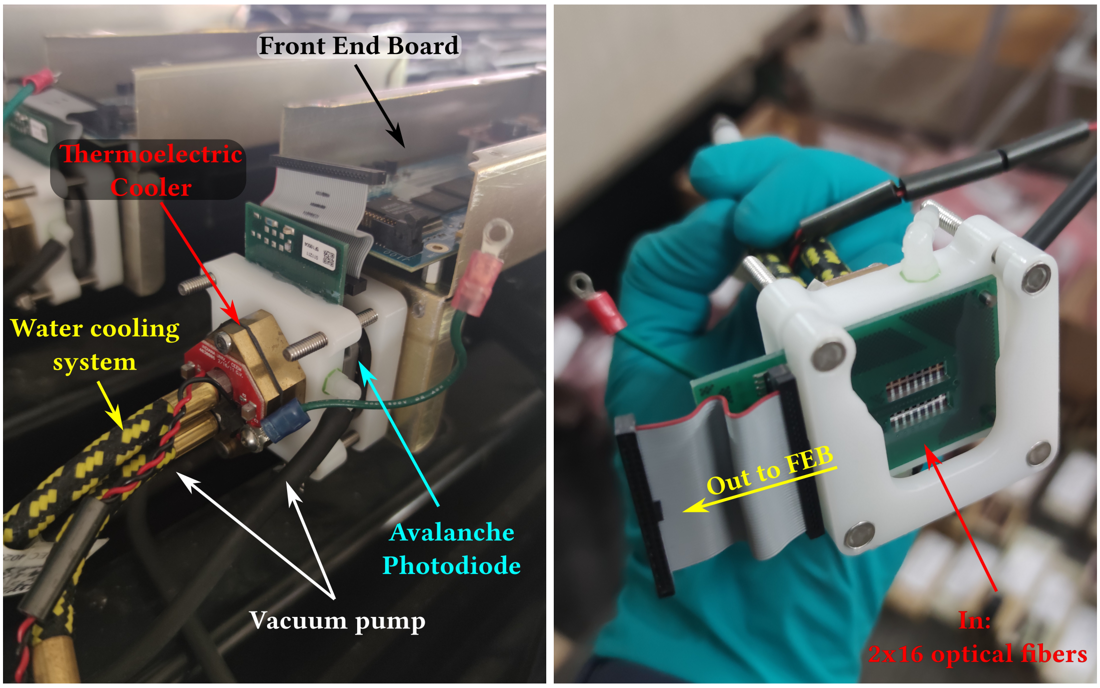

Figure 2.5: The modules with APDs for NOvA mounted on top of the detector on the left picture, and shown from the bottom on the right. The individual components of the module are described. The left picture shows a disconnected ribbon cable and ground cable, which are normally connected to the front end board.

Each APD is connected to a single Front End Board (FEB), shown in Fig. 2.6. The FEB amplifies and integrates the APD signal, determines its amplitude and arrival time, before passing it to the Data Acquisition (DAQ) system. On the FEB the APD signal is first passed to a custom NOvA Application-Specific Integrated Circuit (ASIC), which is designed to maximize the detector sensitivity to small signals. ASICs amplify, shape and combine the signal, before sending it to an Analog-to-Digital Converter (ADC). The combined noise from the APD and the amplifier is equivalent to about 4 PEs, which, compared to an average PE yield from the far end of the FD cell of 30, results in a good signal and noise separation [87]. The digitized data from an ADC is sent to a Field Programmable Gate Array (FPGA), which extracts the time and amplitude of the ADC signals, while subtracting noise based on a settable threshold. The FPGAs employ multiple correlated sampling methods to reduce noise and improve time resolution of the signal [93].

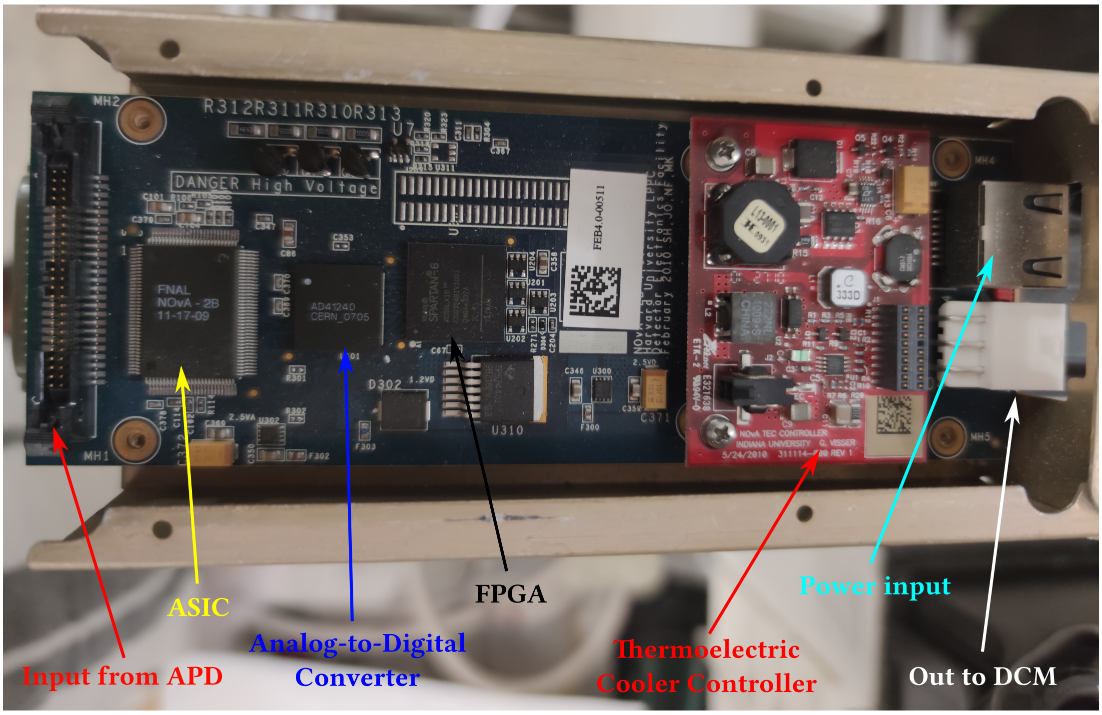

Figure 2.6: An example of a NOvA FEB with individual components labelled.

All of the NOvA front end electronics (APDs and FEBs) are operated in a continuous readout mode, without requiring any external triggers [87]. Due to higher detector activity during beam spills, the ND FEBs work at a higher frequency of 8 MHz, whereas the FD FEBs suffice with 2 MHz sampling frequency [93].

Data from up to 64 FEBs are concentrated in a Data Concentration Module (DCM), which concatenates and packages the data into 5 ms time slices, before sending it to the buffer nodes. DCMs are also connected to the timing system and pass a single unified timing measurement to the FEBs to maintain synchronization across the detector [93].

The buffer nodes cache the data for at least 20 seconds while receiving information from the trigger system. Each trigger uses a time window based either on the time of the NuMI beam spill, on a periodic interval for monitoring and for the readout of cosmic events, or on one of the activity-based data-driven triggers [93]. Data that fall within any of the trigger windows are sent to a data logger system, where they are merged to form events, before being written to files for offline processing and sent to an online monitoring system. Files are organized based on a unique combination of run and subrun numbers, with runs corresponding to data taking periods with constant detector conditions and limited to either 64 subruns or 24 hours. Subruns are delineated either by a $2\,\mathrm{GB}$ file size constraint or a 1-hour timeout limit [94].

The detectors are continuously monitored to ensure data stability and quality. Subruns with suboptimal detector conditions or with events failing basic quality criteria are flagged as 'bad' and recorded in a 'bad runs list' [94]. Additionally, individual readout channel are assessed on a per-subrun basis, with those with too high or too low hit rates marked as 'bad' [95]. Both the 'good runs' list and the 'bad channel' maps are used to inform event processing and during simulation to emulate real detector conditions.

2.4 Simulation

To extract neutrino oscillation parameters, or to test a hypothesis, NOvA uses a series of simulations to make predictions according to various physical models [96]. The simulation chain can be divided into four parts: simulation of the neutrino beam, simulation of neutrino interactions within the NOvA detectors, simulation of cosmic particles interacting in the NOvA detector and simulation of the detector and readout response.

To simulate the neutrino beam, NOvA uses a simulation based on the GEANT4 v9.2.p03 [97] Monte Carlo (MC) event generator with a detailed model of the NuMI beamline [98], as described in Sec. 2.1. The simulation starts with the $120\,\mathrm{GeV/c}$ MI protons interacting within the long carbon target and producing hadrons, mainly

π, K and secondary protons. This is followed by transport and possible further interaction of hadrons within the focusing system, until finally ending with hadron decays producing the neutrino beam.

To account for the inherently imprecise theoretical models used in GEANT4, NOvA uses the Package to Predict the Flux (PPFX) to incorporate external measurements of yields and cross sections of hadron interactions inside the target and the other NuMI materials into the neutrino beam prediction [99]. The current version of PPFX is limited by the results available during its creation and only corrects the most frequent interactions while assigning conservative systematic uncertainties to the rest (see Sec. 2.8). For the most common π, K and p production, PPFX uses the NA49 measurements [100–102] of $158\,\mathrm{GeV/c}$ protons interacting on a thin (few percent of interaction length) carbon target. To expand the kinematic coverage, PPFX uses a few data points from Barton et al [103] for the π production and K/π ratios from the Main Injector Particle Production (MIPP) [104] experiment for the production of K. These results have to be scaled to the $20 - 120\,\mathrm{GeV/c}$ incident proton moment seen throughout NuMI using the FLUKA [105, 106] MC generator.

There are two new experiments that measure the production and interaction of hadrons on various targets and incident energies, specifically designed to improve the prediction of neutrino beams. The most impactful measurements from the NA61 experiment are of the $120\,\mathrm{GeV/c}$ protons on a thin carbon target [107–109], of the hadron incident interactions on various materials [110], and of the $120\,\mathrm{GeV/c}$ protons on a NuMI replica target [111]. The Fermilab-based EMPHATIC experiment [112] is currently analysing a broad range of hadron production and secondary and tertiary interaction measurements for neutrino beam prediction with a significant involvement of NOvA and DUNE collaborators.

The output of the neutrino beam simulation is passed to the simulation of neutrino interactions inside the detectors, which is done with the GENIE v3.0.6 [113] neutrino MC generator. GENIE allows users to choose the particular models for different types of neutrino interactions and particle propagation within the nucleus, as well as possible tunes to external measurements. The four main interaction modes in GENIE are the QE CC scattering, the Res, the DIS, and the COHπ production. The special case of the 2p2h interaction via MEC and the FSI inside a nucleus are also considered. The initial state of the nucleus is represented by a local Fermi gas in the QE and 2p2h models, while a global relativistic Fermi gas is used for all other processes. All of these are set by the Comprehensive Model Configuration (CMC), which is currently `N1810j0000` for NOvA. Additionally, NOvA adds a costume tune to the NOvA ν_μCC data for a better constraint of the CCMEC interactions. NOvA also uses a set of external π interaction measurements to constrain the FSI model. Table 2.1 shows the list of models and tunes for different interaction modes in NOvA [54].

Table 2.1: Models and tunes used in the NOvA simulation of neutrino interactions.

Interaction	Model	Tune
CCQE	València [114]	External $\nu-$ D data [115]
CCMEC	València [116, 117]	NOvA ν_μCC data
Res & COHπ	Berger-Sehgal [118, 119]	External $\nu - A$ data
DIS	Bodek-Yang [120, 121]	External $\nu - A$ data
FSI	Semi-classical cascade [122]	External $\pi -^{12}$ C data

Since the FD is on the surface NOvA also uses a simulation of cosmic rays generated with the MC Cosmic-Ray Shower Generator (CRY) [123]. The simulated cosmic muons are also used to calibrate NOvA detectors [99].

Particles that are created from neutrino interactions and cosmic rays are propagated through the NOvA detectors using the GEANT4 v10.4.p02 [97], which outputs the energy deposited in the scintillator. This is then passed to a custom NOvA software of the light model [99], which calculates the amount of scintillation light produced for the deposited energy based on a Poisson distribution. The scintillation light production is parametrized using the Birks-Chou model [124], which corrects for the recombination in organic scintillators at high deposited energies. The scintillator light yield and the inherent production of the Cherenkov light, which can affect the light readout, are tuned to NOvA data [72]. The light collection by the WLS fibres, its transport to the APDs, and the APD response use a parametrized simulation, as the NOvA cells and their readout are generally the same across the detectors [99]. The simulation of the readout electronics is done by another custom NOvA parametrized model, which accounts for random noise in the readout electronics and outputs true events in the same format as the real data.

Due to the high neutrino rate in the ND, there are neutrinos interacting in the surrounding rock creating particles, mainly muons, that make it to the detector and act as background. However, since only a few ‘rock muons’ make it into the detector, it would be very time consuming to run a simulation which includes the rock around the ND for every neutrino. Instead, NOvA creates a separate simulation that includes the surrounding rock and then overlays these results into the nominal NOvA simulation chain to match the NuMI neutrino rate [99].

2.5 Data Processing and Event Reconstruction

Both data and simulation events for all NOvA detectors are passed through the same event reconstruction and particle identification algorithms. The reconstruction was specifically developed with the ν_e appearance search in mind, focusing on identifying the ν_eCC signal against the ν_μCC and NC backgrounds. Each NOvA detector has to deal with different challenges, with multiple neutrinos interacting during one beam spill in the ND, and a large cosmic background in the FD [125].

The output from the DAQ system for each channel is called a *raw hit*. Hits are grouped into 550 μs-long windows and passed to an offline reconstruction chain [125]. Reconstruction starts by grouping hits into *slices* based on their proximity to other hits in both time and space [126]. Slices are designed to ideally contain only a single neutrino interaction event.

For events that produce hadronic and electromagnetic showers, reconstruction first identifies straight lines through major features using a modified Hough transform [127], representing particle directions. These lines are passed to the Elastic Arms algorithm [128] to identify *vertex* candidates from their intersection points. Hits are then clustered into *prongs*, which are collections of hits with a start point, based on the vertex, and a direction, using a k-means algorithm called FuzzyK [129, 130]. Here ‘fuzzy’ means that each hit can belong to multiple prongs. Prongs are first created separately for each view (also called 2D prongs) and then, if possible, view-matched into 3D prongs (from here on referred to as prongs) [125]. Figure 2.7 shows an example of a simulated electron shower, where the reconstructed vertex is shown as a red cross and the prong as a red shaded area. The prong groups together all the hits that are part of the shower, while removing the background hits, shown in grey.

For particles that are represented by tracks rather than showers (especially muons),

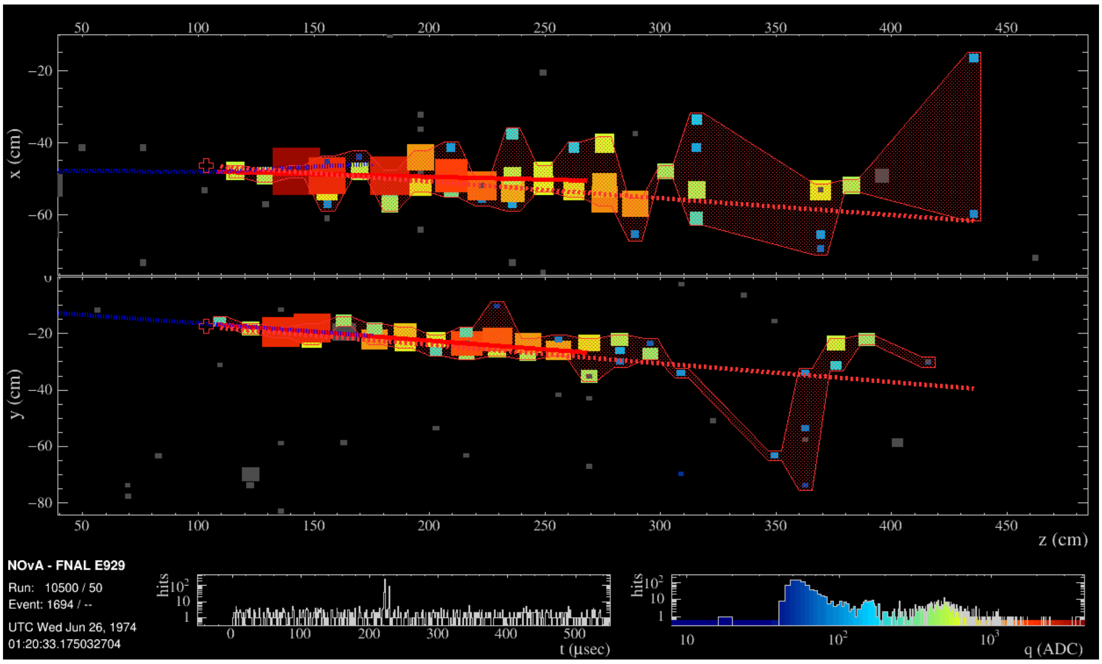

Figure 2.7: Reconstruction of a simulated single electron event in the NOvA ND. The red cross is the reconstructed vertex, the shaded area shows the cluster of hits into a prong and the dotted red line shows the estimated shower direction. The blue dotted line shows the true direct of the scattering neutrino and the solid red line the true momentum of the scattered electron. Figure from internal NOvA database [131].

the reconstruction takes the slice hits and forms 'Kalman tracks' based on a Kalman filter [132]. In addition to the start point and the direction, which exist also for prongs, tracks also contain information on the vector of trajectory points that make up the track and on the end point - and therefore on the track length. A parallel tracking algorithm takes in the Elastic Arms vertex and the Fuzzy-K prongs and forms Break Point Fitter (BPF) tracks [133, 134], using a model of Coulomb scattering and energy loss. BPF tracks also contain an information on the particle 4-momenta based on various particle assumptions, most notably the muon assumption. For cosmic particles, mostly muons, NOvA uses another track reconstruction algorithm, called 'window cosmic track' [135]. It uses a sliding 5 plane-long window, in which it fits a straight line to the recorded hits. The window starts from the end of the detector and then slides forward and repeats the fitting process until all hits are processed. This way it accounts for possible Coulomb scattering of cosmic muons. The intersection of each cosmic track with the edge of the detector (or extrapolation of the track to the edge of the detector) is reconstructed as the 'cosmic ray vertex'.

To identify individual particles and remove backgrounds, NOvA uses several Machine Learning (ML) algorithms, outputs of which are used in combination with the information from classical reconstruction algorithms for Particle Identification (PID). The most common topologies for particles interacting in NOvA detectors are shown in Fig. 2.8. Muons are easily identifiable as single long tracks which decay into an electron (or positron) if stopping inside of the detector. Both electrons and π^0's produce electromagnetic showers, but thanks to the low-Z composition and high granularity of the detector, there is a gap between the interaction vertex and the electromagnetic shower for the π^0.

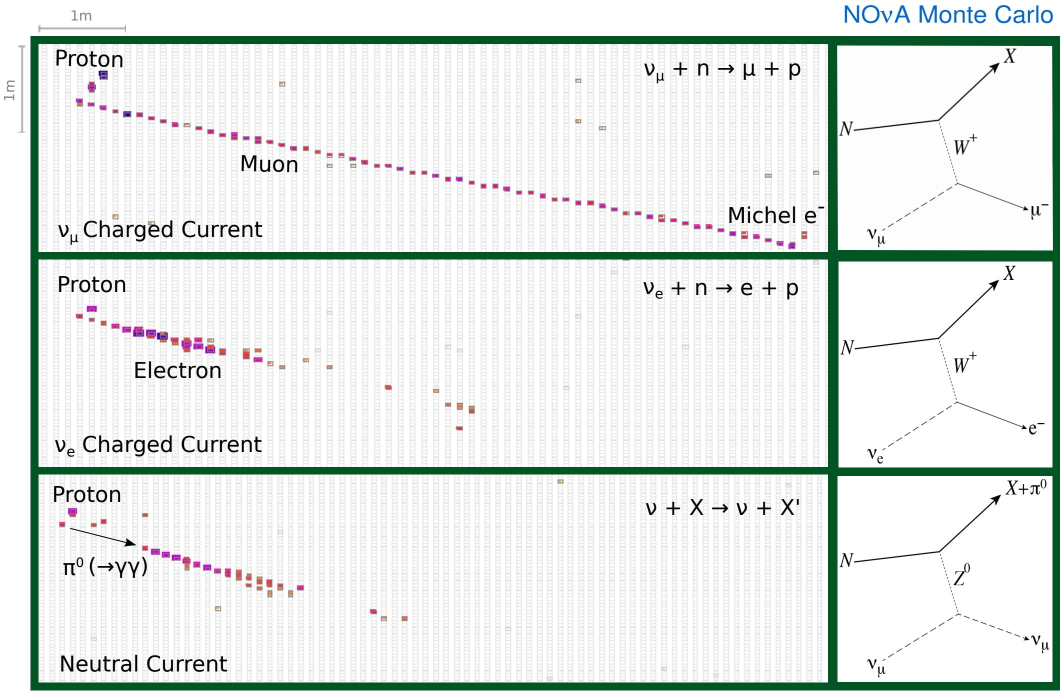

Figure 2.8: Different event topologies as seen in the NOvA detectors with corresponding Feynman diagrams [125]. Each event is a simulated 2.15 GeV neutrino interacting in a NOvA detector producing a 0.78 GeV proton and a second 1.86 GeV particle depending on the interactions type. The figure shows only one view and the colouring represents the deposited energy.

One of the ML algorithms that NOvA employs is a Convolutional Neural Network (CNN) based on the GoogLeNet [136] architecture named Convolutional Visual Network (CVN) [137]. When it is applied to identify entire events it is called *EventCVN* and uses slice hits to classify interactions into one of the five categories: ν_e, ν_μ, ν_τ, NC, or cosmic. The same architecture, but applied to the Fuzzy-K prongs, is called *ProngCVN* [138], and is used to identify what particles the prongs most likely correspond to. This assignment is useful in calculation of prong energy, as described in

Sec. 2.7. Another ML algorithm is specifically designed for identifying muons and is based on a Boosted Decision Tree (BDT). It is called Reconstructed Muon Identifier (ReMId) [132] and uses the reconstructed Kalman tracks as inputs.

2.6 Detector Calibration

The energy deposited within NOvA detectors is represented by the peak ADC values for each cell the particle passed through, obtained from the readout electronics, as described in Sec. 2.3. The conversion of the peak ADC values into physical units of energy requires calibrating the NOvA detectors [139], while accounting for the attenuation of light along the WLS fibres, or for differences between individual cells. The purpose of calibration is to calculate a conversion factor from $\mathrm{ADC} \rightarrow \mathrm{MeV}$ for every part of the detector, so that the same energy deposited anywhere and at any time, is recorded as the same value of the reconstructed energy.

NOvA uses cosmic ray muons for calibration due to their abundance in the NOvA detectors and their consistent energy deposition. To calculate the absolute energy scale, NOvA selects a subsample of muons stopping inside of the detectors when they are almost exactly Minimum Ionising Particle (MIP) and therefore have a well understood energy deposition. The cosmic muons are collected using a periodic trigger with the same length as the beam trigger, whilst removing events with timestamps overlapping with the beam spill window. The simulation of cosmic muons is created using the CRY [123] MC generator, as outlined in Sec. 2.4.

Cosmic muon tracks are reconstructed using the window cosmic track algorithm described in Sec. 2.5. The selection of well reconstructed cosmic tracks requires that at least 80% of all hits from the reconstructed slice contribute to the track [92]. Each track must have at least 2 hits in both the x and y views and the difference in the number of planes the track crossed between the views must be at most 10% of the total number of planes. Also, the plane where each track starts or stops in one view must be within 3 planes of the start or stop plane in the other view. Additionally, since tracks that do not cross many planes tend to not be reconstructed very well, the extent of each track in the z direction must be at least $70\,\mathrm{cm}$ and tracks must have at least 20% of their total track direction in the z axis. Tracks with on average more than 6 cells per plane and with path lengths through the cell larger than $10\,\mathrm{cm}$ are removed for the same reason. Furthermore, all the reconstructed tracks must start at most $10\,\mathrm{cm}$ from the edge inside of the detector and stop at most $10\,\mathrm{cm}$ outside of the detector. Lastly, tracks with trajectory points far away from each other are also removed. The selection of stopping muons for the absolute energy scale relies on identifying Michel electrons, which are produced by decaying muons at the end of their tracks, as can be seen on the top panel of Fig. 2.8.

Since the energy deposited in a cell is proportional to the distance the particle travels through the cell, the input variable for calibration is the deposited energy divided by the path length through the cell PE/cm. To ensure the path length is well calculated, all hits used in calibration must satisfy the so-called 'tricell' condition, shown in Fig. 2.9. This means that for each calibration hit, there must be a corresponding hit in both of the surrounding cells in the same plane for the same track. The path length can then be calculated simply from the height of the cell and the angle of the reconstructed track. In case there is a bad channel in a neighbouring cell (right side of Fig. 2.9), this channel is ignored and the tricell condition looks one cell further [139]. If the tricell condition fails, the hit can still pass the 'z tricell' condition, which is a longitudinal equivalent of the tricell condition and requires a hit in both the neighbouring planes in the same view and with the same cell number. The 'z tricell' hits are saved separately and may be used if there are no hits satisfying the original tricell condition. This is especially useful for the cells on the edge of the detector, which fail the tricell condition due to only having one neighbouring cell.

The calibration conversion factor from the signal recorded by the detector readout to the deposited energy can be expressed by as

$$E_{dep}\ [\mathrm{MeV}] = \mathsf{Signal}\ [\mathrm{ADC}] \times S_d \times TS_{d,i}^{\textsc{Calib}} \times R_{d,i}\left(t\right) \times A_d\left(t\right). \tag{2.1}$$

The calibration scale therefore consists of four separate and complementary factors: the Scale (S_d), the Threshold and Shielding correction ($TS_{d,i}$), the Relative calibration ($R_{d,i}\left(t\right)$) and the Absolute calibration ($A_d\left(t\right)$), all described below. Each part is calculated for each detector separately, as indicated by the subscript d. The threshold and shielding correction is only used during calibration and is omitted when applying the calibration results. The relative and absolute calibrations are calculated for

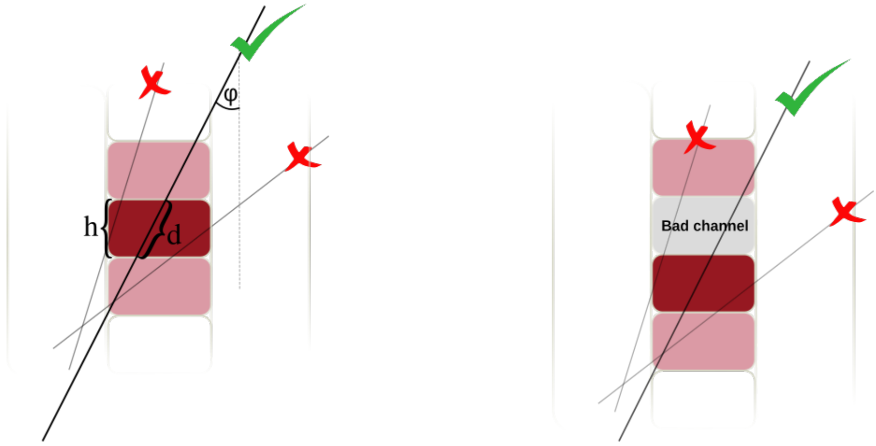

Figure 2.9: Illustration of the tricell condition. Only the hits with two surrounding hits in the same plane are used in the NOvA calibration, as shown on the left plot. This is to ensure a good quality of the path length (d) reconstruction, which is calculated from the known cell height (h) and the reconstructed track angle (φ). In case the hit is next to a bad channel, as shown on the right plot, the bad channel is ignored and the tricell condition requires a hit in the next cell over.

each time period separately to account for possible changes in the energy deposition throughout the time, possibly caused by the ageing of the scintillator oil, or of the readout electronics. The time periods are either determined by a fixed time interval, or by running conditions separated by significant changes to the readout or the DAQ systems, including the summer shutdown.

The threshold and shielding correction and the relative calibration calculate a calibration factor for each position within the detector to account for variations caused by the attenuation of light as it travels through the WLS fibres, or by differences between individual cells. This is expressed with a subscript i in Eq. 2.1. For data, the position of a hit in the detector is described by the plane number, cell number and the position within the cell (w). w is calculated as the projection of the cosmic track to the central cell axis and its value is equivalent to the x axis (y axis) coordinate of the projection for the horizontal (vertical) cells, with the 0 value at the centre of the cell [139].

For simulation, the calibration does not use the plane number to determine the position within a detector, as by construction all detector planes should have the same readout. This significantly reduces the requirements for the number of events that need to be simulated, reconstructed, and calibrated, especially for the FD with 896 planes. However, in reality there are some variations in the detector response between individual planes, caused by different *brightness* qualities of the fibres, zipped or twisted fibres, different qualities of the scintillator, possible air bubbles, and potentially other factors. To include these differences in simulation without having to simulate every cell individually, all the cells are divided into 12 equally populated Fibre Brightness (FB) bins based on the uncorrected average response in the center of that cell, as shown in Fig. 2.10. These FB bins describe the relative differences in the detector response between individual cells [140].

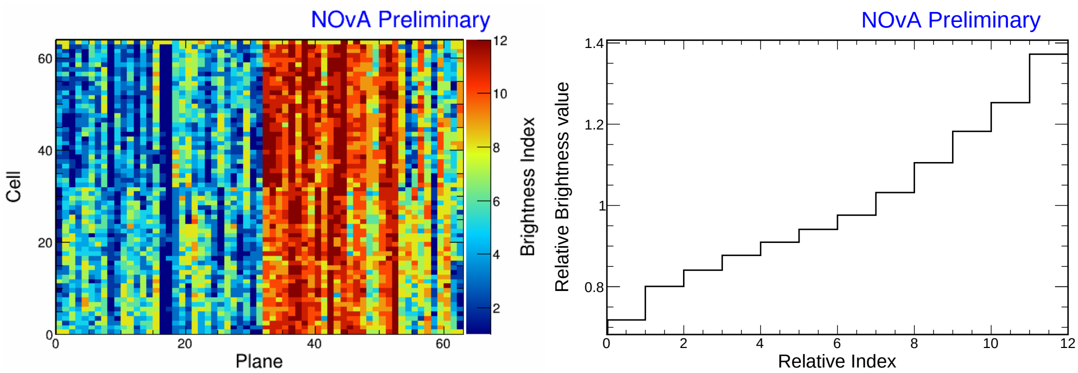

Figure 2.10: Distribution of the NOvA detector cells into 12 brightness bins (left plot), each representing a relative difference in energy response (right plot) due to different brightnesses of the fibres, scintillators, or readout. This is an example from the NOvA Test Beam detector, described in Sec. ??, where the left side of the detector (planes 1-32) has clearly lower response relative to the right side of the detector (planes 33-64).

2.6.1 Scale

The scale calibration factor from Eq. 2.1 is a simple conversion from the peak ADC value into the number of PEs. This factor only depends on the APD gain (which was different in the beginning of NOvA data taking) and on the FEB type (different between detectors, as described in Sec. 2.3).

2.6.2 Threshold and Shielding Correction

The threshold and shielding correction accounts for two assumptions, which hold true in most cases in NOvA, but fall short for some hits at the bottom of the detector, or far away from the readout, especially for the FD [139].

The first assumption is that the ADC response to the photon signal is linear, which is mostly true except close to the APD threshold. Energy deposited far away from the readout may produce photons that get attenuated enough to be shifted below the threshold. However, due to natural fluctuations of the number of photons created by the energy deposition, the same deposited energy may also produce photons that would make it over the threshold, therefore making it appear that the actual deposited energy was higher then in reality, introducing a bias to the calibration. The threshold correction is calculated using simulation, as the ratio between the mean of the Poisson distribution of the true number of the created PE ($\mathrm{PE}_{Poisson\lambda}$) and the number of the 'reconstructed' PE seen by the APD (PE_{Reco}).

The second assumption is that the spectrum of cosmic muons is uniform within each detector. Again, this is generally true, but breaks down in the FD, which is big enough for the top of the detector to shield the bottom of the detector and therefore affect the energy distribution. The shielding correction is calculated from simulation as a ratio between the expected deposited energy if the particle was a MIP (E_{MIP}), which is estimated from simulation for the NOvA scintillator as $E_{\mathrm{MIP}} = 1.78\,\mathrm{MeV/cm}$ and the true deposited energy (E_{true}).

The total threshold and shielding correction is calculated for simulated events in each cell, FB bin and w as

$$TS_i = \frac{\mathrm{PE}_{Poisson\lambda}}{\mathrm{PE}_{Reco}} \frac{E_{\mathrm{MIP}}}{E_{True}}. \tag{2.2}$$

To ensure that the correction changes smoothly across each cell position, the final correction is calculated as a fit to the mean correction value along w in each cell and FB bin.

2.6.3 Relative Calibration

The main goal of the relative calibration is to correct for the attenuation of the scintillator light as it travels through the WLS fibre to the readout. The attenuation in each cell is estimated by performing an 'attenuation fit' to the mean response in $\mathrm{PE/cm}$, as shown in Fig. 2.11. The relative calibration scale is then calculated as the ratio between the average response in $\mathrm{PE/cm}$ across the entire detector (can differ between detectors) and the result of the attenuation fit in each particular position within the detector. The response after applying the relative calibration scale is expressed as

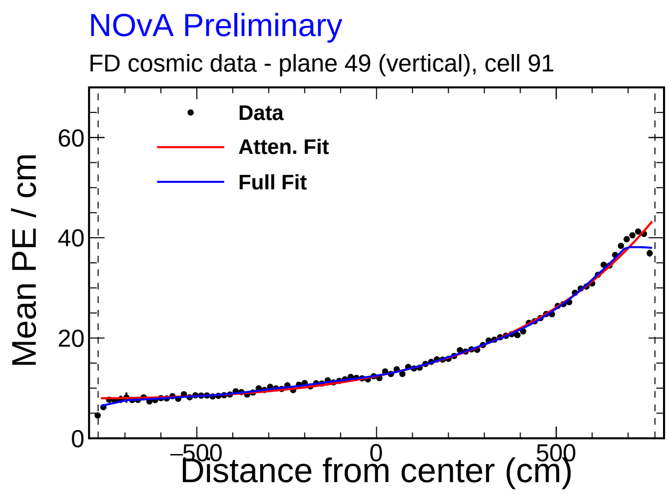

Figure 2.11: Example attenuation fit for a single cell in the NOvA FD across its full length, as shown by dashed vertical lines. The red line shows the initial exponential fit and the blue line shows the full fit after the LOWESS correction, both described in text. Figure from [141].

Corrected Photo Electronss (PECorrs). Since the relative calibration scale is calculated for each cell independently, it effectively corrects for the relative differences between detector cells as well as for the attenuation. Therefore, the resulting distribution of $\mathrm{PECorr}/\mathrm{cm}$ should be uniform across the detector, especially along the plane, cell and w [139].

The first step to do the attenuation fit is to create 'attenuation profiles' for each cell. Attenuation profiles are profile histograms of mean detector response over the path length through the cell, in the units of PE/cm, along the position within the cell. An example attenuation profile is shown in Fig. 2.11 as black dots. The threshold and shielding correction described in Sec. 2.6.2 is applied to the attenuation profiles before doing the attenuation fit, which consists of two steps.

1. The first step is a three-parameter exponential fit according to

$$y = C + A\left(\exp\left(\frac{w}{X}\right) + \exp\left(-\frac{L+w}{X}\right)\right), \tag{2.3}$$

   where y is the fitted response, L is the length of the cell and C, A and X are the fitted parameters representing the background, attenuation scale and attenuation length respectively. An example of the exponential fit is shown as a red curve in Fig. 2.11.

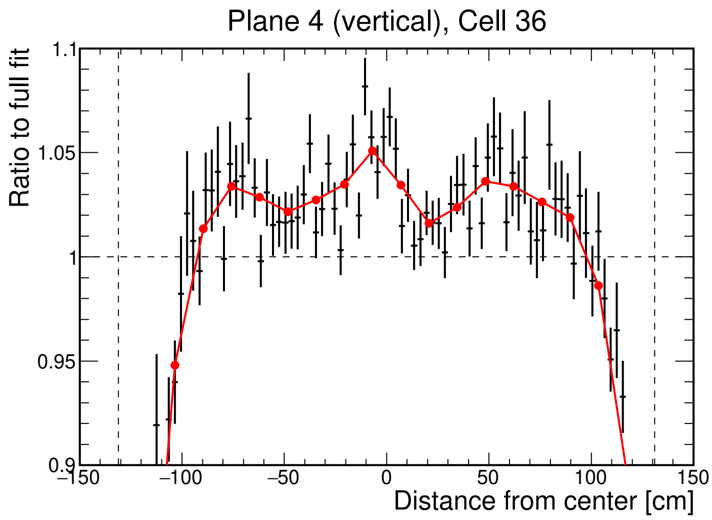

Figure 2.12: Example LOWESS correction for the residual differences after the exponential part of the attenuation fit of the NOvA relative calibration. This is an example for a single cell in the NOvA Test Beam detector with black points showing the residual differences and red line the LOWESS correction, both described in text.

2. The second step is the smoothing out of residual differences between the exponential fit and the original distribution with the Locally Weighted Scatter plot Smoothing (LOWESS) method, shown in Fig. 2.12. The residual differences get evened out by creating a smooth distribution of 20 locally weighted points across the length of each cell. The result of the LOWESS correction is then combined with the exponential fit into the full attenuation fit, shown as a blue line in Fig. 2.11.

Even after applying the LOWESS correction, there are sometimes large differences between the attenuation fit and the fitted response. This is usually caused by a small number of events in that cell, common for cells at the edge of the detector. To ensure a good quality of the attenuation fit, the total χ^2 between the attenuation fit and the fitted response is calculated and only cells with the final $\chi^2 \leq 0.2$ are counted as *calibrated*. Cells with $\chi^2 > 0.2$ are ignored in further processing and marked as *uncalibrated*.

2.6.4 Absolute Calibration

The absolute calibration only uses hits from muons stopping inside of the detector, in a track window $1 - 2\,\mathrm{m}$ from the end of their tracks. This is when they are approximately MIP and their energy deposition is well understood. Additionally, hits at the

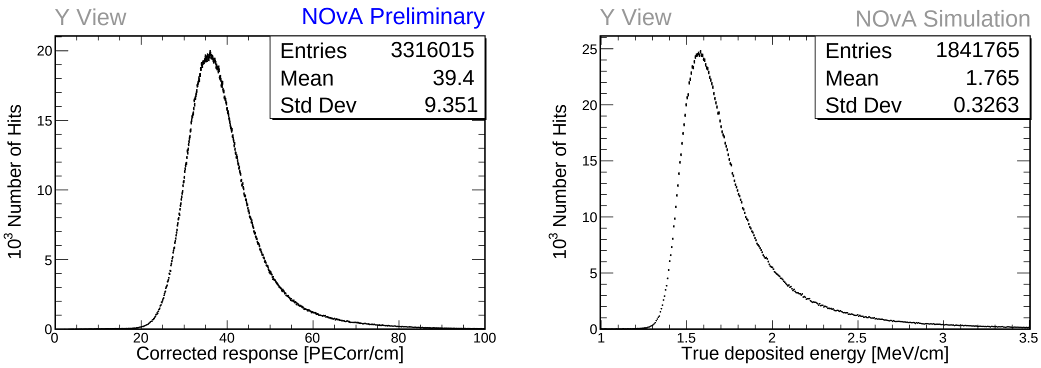

Figure 2.13: The absolute energy scale is calculated as the ratio between the simulated mean true deposited energy (right) and the mean reconstructed energy response (left) for selected stopping muons in each view and each data period or simulation.

edges of each cell are removed to mitigate the effects at the end of the WLS fibres and the lower number of events at the edge of the detector [92].

First, the relative calibration results are applied to the selected stopping muon hits to get a distribution of the corrected detector response in $PECorr/\mathrm{cm}$, as shown on the left of Fig. 2.13. The mean of this distribution is called the *reconstructed* Muon Energy Unit (MEU) and is calculated separately in each of the two views, and in each time period or version of simulation. Analogously, the mean of the true deposited energy in $\mathrm{MeV/cm}$ from simulation, shown on the right of Fig. 2.13, is called the *true* MEU. The absolute energy scale (the absolute calibration scale) is then the ratio between the true and the reconstructed MEU value, where both the MEU values are taken as a simple average over the two views

$$\text{Absolute Energy Scale} = \frac{\mathrm{MEU}_{True}\ [\mathrm{MeV/cm}]}{\mathrm{MEU}_{Reco}\ [\mathrm{PE\textsc{Corr}/cm}]}. \tag{2.4}$$

The values of the absolute energy scales for each data period and simulation, as well as the results of the attenuation fit, are saved in a set of lookup tables, which are then used any time a hit is recorded in the NOvA detector and processed and reconstructed with the NOvA algorithms described above.

2.7 Energy Estimation

The deposited energy from detector calibration (Sec. 2.6) is only the first step in estimating the neutrino energy (E_ν) required for the main NOvA analyses.

For the ν_μ disappearance analysis, the ν_μ energy is measured as the sum of the muon energy and the energy of the hadronic shower [54]. The muon energy is identified from the length of its track, without the need of the calibration results. The energy of the hadronic shower is estimated from simulation as a fit to the 2D distribution of the true ν_μ energy minus the reconstructed muon energy, versus the visible (not corrected for the dead material) deposited energy of the hadronic system [138].

For the ν_e appearance analysis, the ν_e energy is calculated using a quartic fit to the 2D distribution of the electromagnetic versus the hadronic calorimetric energies, both corrected for the energy deposition in the dead material (PVC cells) [138]. The dead material correction is currently just a simple scaling of the deposited energy from calibration for all particles and is calculated from the measurement of the π^0 mass peak in the NOvA ND. This correction is correct only for electromagnetic showers and is not directly applicable to hadronic showers. The fit to determine the ν_e energy keeps the normalization of both the electromagnetic and the hadronic energies free, so the exact value of the dead material correction is not important. It is however used in other, non-neutrino oscillation analyses.

2.8 Systematic Uncertainties at NOvA

Systematic uncertainties in NOvA analyses arise from the imperfect knowledge on the individual components of the NOvA experiment, or from the known shortcomings of the prediction used to extract the measured parameters. Even though different analyses in NOvA need to consider different systematic uncertainties and their effect on the results varies, there are a few commonalities across all NOvA analyses that are explained below.

Both the 3-flavour [54] and the sterile neutrino [76] oscillation analyses in NOvA use the ND to constrain the FD prediction, which significantly reduces the effect of the neutrino beam and interaction prediction systematic uncertainties. On the other hand, these are the leading sources of systematic uncertainties for the ND-only analyses, such as the cross section analyses [71–74]. The leading systematic uncertainty for the neutrino oscillation measurements comes from the detector calibration uncertainty. Significant uncertainties for all NOvA measurements also come from the neutron modelling, the detector simulation and the muon energy estimation. There are other sources of systematic uncertainties that are not mentioned here as they are sub-dominant, or specific to a certain analysis.

TO DO: *Mention here how are the systematics used - shifting the spectra and doing the full analysis 'separately' for each shifted prediction. Then we compare these shifted predictions with the nominal one*

The systematic uncertainty on the prediction of the neutrino beam consists of two parts: the hadron production and the beam focusing uncertainties [99]. The uncertainty for hadron production is estimated by the PPFX (describe in Sec. 2.4) using the multi-universe technique. Here we create 100 PPFX universes in which the inputs from the external measurements used to constrain the hadron production are randomly floated around their central values within their respective systematic uncertainties. Parts of the hadron production that are not constrained by external measurements are given a conservatively large systematic uncertainty. The beam focusing systematic uncertainties account for the uncertainties on the horn and target positions, the horn current, the beam position on the target, the beam spot size, and the effect of Earth's magnetic field in the beam pipe. TO DO: *Describe the beam PCA and how can we limit the beam uncertainty*

TO DO: *Describe the neutrino interaction modelling systematic uncertainties* [3fl technote] There's in total 77 neutrino interaction related systematic uncertainty knobs that are randomly varied during fitting. Only the ones that contribute are actually accepted during a fit.

TO DO: *Describe the detector modelling systematic uncertainties*

The systematic uncertainty arising from the simulation of the detector response can be divided into the scaling of the overall light level inside the simulation and of the Cherenkov light component.

The systematic uncertainty on the Cherenkov light scaling factor is calculated by profiling over the factor during the light model tune and taking the 3σ confidence interval around the best fit value as the systematic uncertainty, resulting in a $\pm 6.2\,\%$ relative uncertainty on the Cherenkov scaling factor. Similarly, the light level uncertainty was calculated by profiling over the light level scaling factor, resulting in a $\pm 5\,\%$ relative uncertainty on the light level scaling factor.

TO DO: *Describe the neutron uncertainty - only if I decide I need it*

There are three systematic uncertainty arising from the calibration procedure: the absolute energy scale, the shape (relative residual variations along the cell, especially on its edges) and detector ageing.

Other standard candles are used to set the systematic uncertainty on the absolute energy scale. This is calculated as the difference between the data and simulation reconstructed energy for beam muons and protons in the ND, rock muons in the ND, π^0 measurement in the ND and Michel electrons in the ND. These discrepancies drove the decision to set the systematic uncertainty on the absolute energy scale to $5\,\%$. Measurements from the NOvA Test Beam experiment will help reduce this systematic uncertainty.

[3fl technote] The calibration shape systematic uncertainty was defined based on data/MC differences. The uncertainty was parameterized with a linear shape, with different slopes in the middle of the detector vs the edges, determined by linear fits to data/MC ratios.

[3fl technote] The detector ageing uncertainty is implemented as a simple linear drift downward in light level as a function of time, and a corresponding drift upward in the overall calibration scale to compensate. This is intended to mimic the impact of the number of hits above thresholds falling over time, while the overall calorimetric energy remains the same. For a more detailed summary, see Section 4.3 in the Prod5 detector simulation technote [2].

TO DO: *Describe the calibration uncertainties*

Chapter 3

Measuring the Muon Neutrino Magnetic Moment

In this analysis, I aim to detect a potential signal of the effective muon neutrino magnetic moment in the NOvA ND. This signal would manifest as an excess of neutrino-on-electron (ν-on-e) elastic scattering interactions at low electron recoil energies, proportional to the value of the effective neutrino magnetic moment, over the SM background. If no significant excess is observed, I will establish an upper limit on the effective muon neutrino magnetic moment.

Detecting the neutrino magnetic moment would provide a definitive evidence of new BSM physics, and measuring its value would help identify the appropriate BSM theory. As current and planned experiments can only detect an anomalously large neutrino magnetic moment, observing such a signature would strongly suggest that neutrinos are Majorana particles and would have significant implications for astrophysics and cosmology [51].

The best model-independent experimental results on the neutrino magnetic moment come from experiments searching for dark matter using xenon-based detectors. These highly sensitive detectors detect solar neutrinos, which are part of the background in dark matter searches but can be reanalyzed for other purposes. In 2020, the XENON1T experiment observed [142] a low energy excess of solar neutrinos, which could correspond to a signal from an anomalously large effective magnetic moment within $\mu_{\nu_\odot} \in (0.14, 0.29) \times 10^{-10}\mu_B$ at $90\,\%$ Confidence Level (C.L.), where $\nu_\odot$ marks solar neutrinos. However, this result was disfavoured by the follow-up XENONnT experiment in 2022 [143], which saw no excess and set the current world-leading limit on neutrino magnetic moment at $\mu_{\nu_\odot} < 0.063 \times 10^{-10}\mu_B$ at $90\,\%$ C.L.. Other solar neutrino experiments also reported null results regarding neutrino magnetic moment [144, 145], placing less stringent limits on its value. Given some basic assumptions [145, 146] this limit for solar neutrinos would correspond to a limit on muon neutrino effective magnetic moment of $\mu_{\nu_\mu} < 0.137 \times 10^{-10}\mu_B$. However, the relationship between effective magnetic moments of different neutrino flavours may be non-trivial, especially in the context of possible new BSM physics, and studying muon neutrinos remains an important endeavour [147].

The best results for ν_μ and $\overline{\nu}_\mu$ come from accelerator-based stopped pion neutrino sources [148, 149], which also do not observe any low energy excess and provide an upper limit on the effective muon neutrino magnetic moment of $\mu_{\nu_\mu} < 6.8 \times 10^{-10}\mu_B$ at $90\,\%$ C.L. [148]. Stopped pion neutrino sources provide a well-understood beams made up of ν_μ, $\overline{\nu}_\mu$ and ν_e with energies up to $52.8\,\mathrm{MeV}$. Slightly looser limits come from pion decay-in-flight accelerator-based measurements (similar to NOvA)[150, 151], which provide a limit of $\mu_{\nu_\mu} < 8.5 \times 10^{-10}\mu_B$ at $90\,\%$ C.L..

Thanks to the very intense and highly pure beam of muon neutrinos and antineutrinos, and a detector designed for the reconstruction and identification of events with electrons in the final state, NOvA is well-positioned to provide a highly competitive, and possibly even world-leading, measurement (or limit) of the effective muon neutrino magnetic moment. A previous analysis of NOvA ND data for a measurement of the effective muon neutrino magnetic moment was presented in a thesis [152], providing a (statistics-only) limit of $\mu_{\nu_\mu} < 15.8 \times 10^{-10}\mu_B$ at $90\,\%$ C.L..

Additionally, ν-on-e elastic scattering interactions are used in various other analyses in NOvA, specifically in efforts to constrain the neutrino beam prediction [153, 154] and in the search for Light Dark Matter (LDM) [155]. These analyses developed various tools and methods that can be utilized in the search for neutrino magnetic moment.

In this chapter, I will provide an overview of the theory of neutrino electromagnetic interactions in Sec. 3.1, focusing on the effective neutrino magnetic moment and its implications for ν-on-e measurements and other theoretical considerations. In Sec. 3.2, I will discuss the analysis strategy, the signal and background definition, as well as the data and simulation samples and the analysis weights. Following this, Sec. 3.3 will explain the selection of events for this analysis, while Sec. 3.4 will cover the electron recoil energy and angle resolution studies and the choice of binning. Sec. 3.5 will address the relevant systematic uncertainties and Sec. 3.6 will introduce the methods used in the statistical analysis of the measurement. Finally, I will present the results of this analysis in Sec. 3.7 and discuss their implications in Sec. 3.8. Section 3.9 will summarise the findings of this analysis.

3.1 Theory of neutrino magnetic moment

As was describe in Sec. 1, neutrinos in the SM are massless and electrically neutral particles. However, even SM neutrinos can have electromagnetic interaction through loop diagrams involving charged leptons and the W boson, covered by the neutrino charge radius [51].

In general BSM theories, considering interactions with a single photon as shown on Fig. 3.1, neutrino electromagnetic interactions can be described by an effective interaction Hamiltonian [156]

$$\mathcal{H}_{em}^{(\nu)}(x) = \sum_{k,j=1}^{N} \overline{\nu}_k(x)\,\Lambda_\mu^{kj}\nu_j(x)\,A^\mu(x)\,. \tag{3.1}$$

Here $\nu_k(x)\,, k = 1, ..., N$, are neutrino fields in the mass basis with N neutrino mass states, Λ_μ^{kj} is a general vertex function and $A^\mu(x)$ is the electromagnetic field.

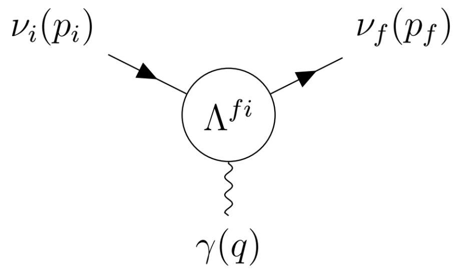

Figure 3.1: Effective coupling of neutrinos with one photon electromagnetic field.

The vertex function $\Lambda_\mu^{fi}(q)$ is generally a matrix and, in the most general case consistent with the SM gauge invariance [157, 158], can be written in terms of linearly independent products of Dirac matrices (γ) and only depends on the four momentum of the photon ($q = p_f - p_i$):

$$\begin{aligned}\Lambda_\mu^{fi}(q) =&\mathbb{F}_1^{fi}\left(q^2\right)q_\mu + \mathbb{F}_2^{fi}\left(q^2\right)q_\mu\gamma_5 + \mathbb{F}_3^{fi}\left(q^2\right)\gamma_\mu + \mathbb{F}_4^{fi}\left(q^2\right)\gamma_\mu\gamma_5 + \\ &\mathbb{F}_5^{fi}\left(q^2\right)\sigma_{\mu\nu}q^\nu + \mathbb{F}_6^{fi}\left(q^2\right)\epsilon_{\mu\nu\rho\gamma}q^\nu\sigma^{\rho\gamma},\end{aligned} \tag{3.2}$$

where $\mathbb{F}_i^{fi}(q^2)$ are six Lorentz invariant form factors and δ and ϵ are the Dirac delta and the Levi-Civita symbols respectively.

Applying conditions of hermiticity $\left(\mathcal{H}_{em}^{(\nu)\dagger} = \mathcal{H}_{em}^{(\nu)}\right)$ and of the gauge invariance of the electromagnetic field, the vertex function can be rewritten as

$$\Lambda_\mu^{fi}(q) = \left(\gamma_\mu - q_\mu \not{q}/q^2\right)\left[\mathbb{F}_Q^{fi}\left(q^2\right) + \mathbb{F}_A^{fi}\left(q^2\right) q^2 \gamma_5\right] - i\sigma_{\mu\nu}q^\nu \left[\mathbb{F}_M^{fi}\left(q^2\right) + i\mathbb{F}_E^{fi}\left(q^2\right)\gamma_5\right], \tag{3.3}$$

where $\mathbb{F}_Q^{fi}, \mathbb{F}_M^{fi}, \mathbb{F}_E^{fi}$ and $\mathbb{F}_A^{fi}$ are hermitian matrices representing the charge, dipole magnetic, dipole electric and anapole neutrino form factors respectively. It is clear that the vertex function only depends on the square of the four momentum of the photon q^2. In coupling with a real photon $(q^2 = 0)$ these form factors become the neutrino charge and magnetic, electric and anapole moments respectively. Additionally, the neutrino charge radius corresponds to the second term in the expansion of the charge form factor [156].

The above expression can be simplified [159] as

$$\Lambda_\mu^{fi}(q) = \gamma_\mu \left(Q_{\nu_{fi}} + \frac{q^2}{6}\langle r^2\rangle_{\nu_{fi}}\right) - i\sigma_{\mu\nu}q^\nu \mu_{\nu_{fi}}, \tag{3.4}$$

where $Q_{\nu_{fi}}$, $\langle r^2\rangle_{\nu_{fi}}$, and $\mu_{\nu_{fi}}$ are the neutrino charge, effective charge radius (also containing anapole moment), and an effective magnetic moment (also containing electric moment) respectively. This is possible thanks to the similar effects of the neutrino charge radius and the anapole moment, and of the neutrino magnetic and electric moments, on neutrino interactions. Therefore, these are the three neutrino electromagnetic properties (charge, effective charge radius and effective magnetic moment) measured in experiments.

The neutrino electric charge is primarily constrained through measurements of the neutrality of matter and cosmological observations, which provide much better constraints than neutrino oscillation experiments [156]. On the other hand, the neutrino charge radius would manifest as an increase in the size of the ν-on-e elastic scattering coupling constants, allowing it to be studied in neutrino oscillation experiments such as NOvA. Additionally, the value of the neutrino charge radius in the SM is only an order of magnitude smaller than the current world-leading limits [52] and measuring it could either confirm the validity neutrino interactions in the SM, or open possibilities to non-standard contributions to neutrino scattering [156]. However, measurement of the neutrino charge radius is not part of this analysis, but may be included in the future re-analysis of the ν-on-e interactions in the NOvA ND.

3.1.1 Neutrino electric and magnetic dipole moments

The size and effect of neutrino electromagnetic properties depend on the specific BSM theory applied. Evaluating one loop diagrams in the minimally extended SM with three right-handed Dirac neutrinos, as described in Sec. 1.4, gives the first approximation of the electric and magnetic moments, which are now 3×3 matrices with elements:

$$\left.\begin{matrix} \mu^D_{kj} \\ i\epsilon^D_{kj} \end{matrix}\right\} \simeq \frac{3eG_F}{16\sqrt{2}\pi^2}\left(m_k \pm m_j\right)\left(\delta_{kj} - \frac{1}{2}\sum_{l=e,\mu,\tau} U^\star_{lk}U_{lj}\frac{m_l^2}{m_W^2}\right), \tag{3.5}$$

where m_k, m_j are the neutrino masses and m_l are the masses of charged leptons which appear in the loop diagrams [156]. The D superscript denotes Dirac neutrinos and M denotes Majorana neutrinos throughout this section. Also, e is the electron charge, G_F is the Fermi coupling constant, and U is the PMNS neutrino oscillation matrix. Higher order electromagnetic corrections were neglected, but can also have a significant contribution, depending on the theory.

It can be seen that Dirac neutrinos have no diagonal electric moments $\left(\epsilon^D_{kk} = 0\right)$ and their diagonal magnetic moments are approximately

$$\mu^D_{kk} \simeq \frac{3eG_F m_k}{8\sqrt{2}\pi^2} \simeq 3.2 \times 10^{-19}\left(\frac{m_k}{\text{eV}}\right)\mu_B, \tag{3.6}$$

where μ_B is the Bohr magneton which represents the value of the electron magnetic moment [156]. Neutrino magnetic moments are therefore strongly suppressed by the smallness of neutrino masses, with theoretical predictions in Eq. 3.6 several orders of magnitude below the reach of current experiments [159].

The transition magnetic moments in the minimally extended SM from Eq. 3.5 are suppressed with respect to the largest of the diagonal magnetic moments by at least a factor of 10^{-4} due to the m_W^2 in the denominator. The transition electric moments are even smaller due to the mass difference in Eq. 3.5. Therefore an experimental observation of a magnetic moment larger than in Eq. 3.6 would indicate physics beyond the minimally extended SM [156, 160].

The suppression of the neutrino magnetic moment by the smallness of its mass can be also expressed in a general case [160]. The 'natural' upper limits on the size of the neutrino magnetic moment for any BSM theory that has NP generated at a scale Λ_{NP} can be expressed as [161]

$$\mu_\nu^D\,(\mu_B) \lesssim 3 \times 10^{-15} \frac{m_\nu^D\,(\mathrm{eV})}{[\Lambda_{NP}\,(\mathrm{TeV})]^2}. \tag{3.7}$$

Therefore for $\Lambda_{NP} \simeq 1$TeV and $m_\nu^D \lesssim 1$eV the limit becomes $\mu_\nu^D \lesssim 3 \times 10^{-15} \mu_B$, well below the current experimental capabilities. However, these upper bounds only apply if NP is generated well above the electroweak scale $\Lambda_{EW} \sim 100\,\mathrm{GeV}$ [156].

For Majorana neutrinos, the magnetic and electric form factors (and therefore the magnetic and electric moment matrices) are antisymmetric, thus Majorana neutrinos only have transition moments. The simplest extension of the SM that includes Majorana neutrinos requires either the addition of a Higgs triplet, or right-handed neutrinos together with a Higgs singlet [156]. Neglecting the Feynman diagrams which depend on the model of the scalar sector, the magnetic and electric dipole moments are

$$\left.\begin{matrix} \mu_{kj}^M \\ \\ \epsilon_{kj}^D \end{matrix}\right\} \simeq \mp \frac{3ieG_F}{16\sqrt{2}\pi^2} (m_k \pm m_j) \sum_{l=e,\mu,\tau} \mathrm{Im}/\mathrm{Re}\,[U_{lk}^\star U_{lj}]\, \frac{m_l^2}{m_W^2}, \tag{3.8}$$

where Im is for μ_{kj}^M and Re is for ϵ_{kj}^D. These are difficult to compare to the Dirac case, due to possible presence of Majorana phases in the PMNS matrices, but it is clear that they have the same order of magnitude as Dirac transition dipole moments. However, the neglected model dependent contributions can enhance the transition dipole moments for Majorana neutrinos [156].

The natural upper bound on the Majorana magnetic moment is less strict compared to the Dirac neutrinos, due to the antisymmetric nature of Majorana magnetic moment, which requires an addition of additional Yukawa couplings into the BSM theory compared to Dirac neutrinos, which can enhance the maximal possible magnetic moment [160]. The limit for Majorana neutrinos can be expressed as

$$\mu_{\alpha\beta}^M\,(\mu_B) \leq 4 \times 10^{-9} \frac{[m_\nu^M]_{\alpha\beta}\,(\mathrm{eV})}{[\Lambda_{NP}\,(\mathrm{TeV})]^2} \frac{m_\tau^2}{|m_\alpha^2 - m_\beta^2|}, \quad \alpha, \beta \in \{e, \mu, \tau\}\,. \tag{3.9}$$

Here, the neutrino magnetic moment is expressed in the flavour basis instead of the mass basis, since the charged lepton masses are diagonal here. The two basis are related by

$$\mu_{ij} = \sum_{\alpha\beta} \mu_{\alpha\beta} U^{\star}_{\alpha i} U_{\beta j}. \tag{3.10}$$

and the effect of the neutrino magnetic moment on neutrino interactions does not depend on the choice of the basis[62].

These considerations imply, that if a magnetic moment $\mu \gtrsim 10^{-15}\mu_B$ would be measured, neutrinos are almost certainly Majorana particles [160].

Effective neutrino magnetic moment

As mentioned above, the neutrino magnetic moment that is measured in experiments is the so-called effective neutrino magnetic moment, which is a combination of electric and magnetic dipole moments and depends on neutrino source and oscillations. In the ultra-relativistic limit, the neutrino effective magnetic moment is

$$\mu^2_{\nu_l}(L, E_\nu) = \sum_j \left| \sum_k U^{\star}_{lk} e^{\mp i \Delta m^2_{kj} L/2E_\nu} \left(\mu_{jk} - i\epsilon_{jk}\right) \right|^2, \tag{3.11}$$

where the minus sign in the exponent is for neutrinos and the plus sign for antineutrinos [156]. Therefore, the only difference between the effective neutrino and antineutrinos magnetic moment is in the phase induced by neutrino oscillations. For experiments with baselines short enough that neutrino oscillations would not have time to develop ($\Delta m^2 L/2E_\nu \ll\sim 1$), such as the NOvA ND, the effective magnetic moment is the same for neutrinos and antineutrinos and is independent of the neutrino energy.

Since the effective magnetic moment depends on the initial neutrino flavour, it is different for experiments studying neutrinos from different sources. Additionally, experiments such as solar neutrino experiments, need to include matter effects on the neutrino oscillations. Therefore the reports on the value (or upper limit) of the effective neutrino magnetic moment are not directly comparable between different types of neutrino experiments.

3.1.2 Measuring neutrino magnetic moment

The most sensitive method to measure neutrino magnetic moment is the low energy elastic scattering of (anti)neutrinos on electrons [156]. The diagram for this interaction is shown in Fig. 3.2 displaying the two observables, the recoil electron's kinetic energy ($T_e = E_{e'} - m_e$) and the recoil angle with respect to the incoming neutrino beam (θ).

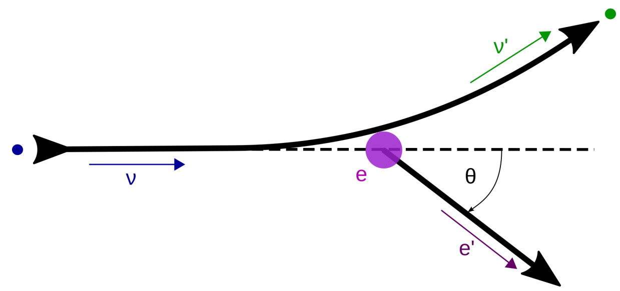

Figure 3.2: Neutrino-on-electron elastic scattering diagram

COMMENT: *Is this derivation too trivial to mention in a thesis? Should I just mention the results?* Since the ν-on-e interaction is governed by simple $2 \to 2$ kinematics, it is possible to get

$$(P_\nu - P_{e'})^2 = (P_{\nu'} - P_e)^2 \,, \tag{3.12}$$

$$m_\nu^2 + m_e^2 - 2E_\nu E_{e'} + 2E_\nu p_{e'} \cos\theta = m_\nu^2 + m_e^2 - 2E_{\nu'} m_e. \tag{3.13}$$

From the energy conservation

$$E_\nu + m_e = E_{\nu'} + E_{e'} = E_{\nu'} + T_e + m_e \Rightarrow E_{\nu'} = E_\nu - T_e \tag{3.14}$$

follows

$$E_\nu p_{e'} \cos\theta = E_\nu E_{e'} - E_{\nu'} m_e = E_\nu (T_e + m_e) - (E_\nu - T_e) m_e = T_e (E_\nu + m_e) \,, \tag{3.15}$$

$$\cos\theta = \frac{E_\nu + m_e}{E_\nu} \sqrt{\frac{T_e^2}{E_{e'}^2 - m_e^2}} = \frac{E_\nu + m_e}{E_\nu} \sqrt{\frac{T_e^2}{T_e^2 + 2T_e m_e}}. \tag{3.16}$$

And finally

$$\cos\theta = \frac{E_\nu + m_e}{E_\nu} \sqrt{\frac{T_e}{T_e + 2m_e}}. \tag{3.17}$$

Which can be rearranged to get

$$T_e = \frac{2m_e E_\nu^2 \cos^2\theta}{(E_\nu + m_e)^2 - E_\nu^2 \cos^2\theta}. \tag{3.18}$$

Electron's kinetic energy is therefore kinematically constrained by the energy conservation as

$$T_e \leq \frac{2E_\nu^2}{2E_\nu + m_e}, \tag{3.19}$$

which corresponds to the $\cos\theta \to 1$ when the recoil electron goes exactly forward in the incident neutrino direction, as depicted in Fig. 3.3.

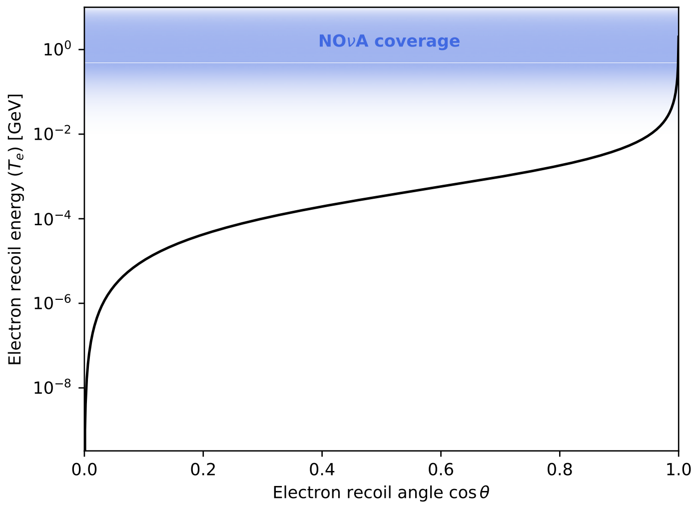

Figure 3.3: Relation between the recoil electron's kinetic energy and angle for the ν-on-e elastic scattering. The coverage of the NOvA detectors for measuring the electron recoil energy is shown in blue. Only very forwards electron's are therefore recorded in NOvA.

Considering $E_\nu \sim$ GeV, it is useful to approximate $\frac{m_e^2}{E_\nu^2} \to 0$. Additionally, considering only very small electron recoil angles, meaning $\theta^2 \cong (1 - \cos^2\theta)$, applied to Eq. 3.17 results in

$$T_e\theta^2 \cong T_e \left(1 - \left(\frac{E_\nu + m_e}{E_\nu}\right)^2 \frac{T_e}{T_e + 2m_e}\right) = T_e \left(1 - \left(1 + \frac{2m_e}{E_\nu}\right) \frac{T_e}{T_e + 2m_e}\right), \tag{3.20}$$

therefore

$$T_e\theta^2 \cong \frac{2m_e T_e}{T_e + 2m_e}\left(1 - \frac{T_e}{E_\nu}\right) = 2m_e \left(\frac{1}{1 + \frac{2m_e}{T_e}}\right)\left(1 - \frac{T_e}{E_\nu}\right), \tag{3.21}$$

and finally

$$T_e\theta^2 \cong 2m_e\left(1-\frac{T_e}{E_\nu}\right) < 2m_e. \tag{3.22}$$

This is a strong limit that very clearly distinguishes the ν-on-e elastic scattering events from other similar interactions involving single electron (mainly the ν_eCC interactions).

Neutrino magnetic moment cross section

In the ultra-relativistic limit, the neutrino magnetic moment interaction flips the neutrino helicity, while the SM weak interaction conserves it, which means it is possible to add the two contribution to the total ν-on-e cross section incoherently (without interference terms) [156]:

$$\frac{d\sigma_{\nu_e^-}}{dT_e} = \left(\frac{d\sigma_{\nu_e^-}}{dT_e}\right)_{\mathsf{SM}} + \left(\frac{d\sigma_{\nu_e^-}}{dT_e}\right)_{\mathsf{MAG}}. \tag{3.23}$$

The SM contribution can be expressed as [16, 156]:

$$\left(\frac{d\sigma_{\nu_e^-}}{dT_e}\right)_{\mathsf{SM}} = \frac{2G_F^2 m_e}{\pi}\left\{g_1^2 + g_2^2\left(1-\frac{T_e}{E_\nu}\right)^2 + g_1 g_2 \frac{m_e T_e}{E_\nu^2}\right\}, \tag{3.24}$$

where the coupling constants g_1 and g_2 differ for between neutrino flavours and between neutrinos and antineutrinos. Their values are:

$$g_1^{\nu_e} = g_2^{\overline{\nu}_e} = \sin^2\theta_W + 1/2, \qquad g_2^{\nu_e} = g_1^{\overline{\nu}_e} = \sin^2\theta_W, \tag{3.25}$$

$$g_1^{\nu_{\mu,\tau}} = g_2^{\overline{\nu}_{\mu,\tau}} = \sin^2\theta_W - 1/2, \qquad g_2^{\nu_{\mu,\tau}} = g_1^{\overline{\nu}_{\mu,\tau}} = \sin^2\theta_W, \tag{3.26}$$

where $\sin^2\theta_W \cong 0.23$.

The total SM cross section, and therefore the number of SM ν-on-e interactions, depends on the neutrino energy and the minimum measured electron recoil energy. However, in general the cross section for for ν_e is about 2.5 times larger than for the $\overline{\nu}_e$, about 6 times larger than for $\nu_{\mu/\tau}$ and about 7 times larger than for $\overline{\nu}_{\mu/\tau}$.

The neutrino magnetic moment contribution is [156, 162]:

$$\left(\frac{d\sigma_{\nu_l e^-}}{dT_e}\right)_{\mathsf{MAG}} = \frac{\pi\alpha^2}{m_e^2}\left(\frac{1}{T_e}-\frac{1}{E_\nu}\right)\left(\frac{\mu_{\nu_l}}{\mu_B}\right)^2, \tag{3.27}$$

where α is the fine structure constant and μ_{ν_l} is the effective magnetic moment of ν_l. The total cross section now only depends on the neutrino energy and on the effective magnetic moment, but is the same for neutrinos and antineutrinos.

The comparison of the SM and the neutrino magnetic moment differential cross sections is shown in Fig.3.4. Whereas the SM cross section is approximately uniform for $T_e \to 0$, the neutrino magnetic moment cross section rises to infinity. However, this reach is limited by the experimental capabilities of detecting electrons with very low energies. The (possible) NOvA coverage is shown with a shaded blue region, with current capability reaching $T_e = 0.5\,\mathrm{GeV}$. Future analyses might extend this reach to lower T_e, with the lowest possible detectable electron recoil energy $T_{e,min} \approx 0.01\,\mathrm{GeV}$, as discussed in Sec. 2.2.

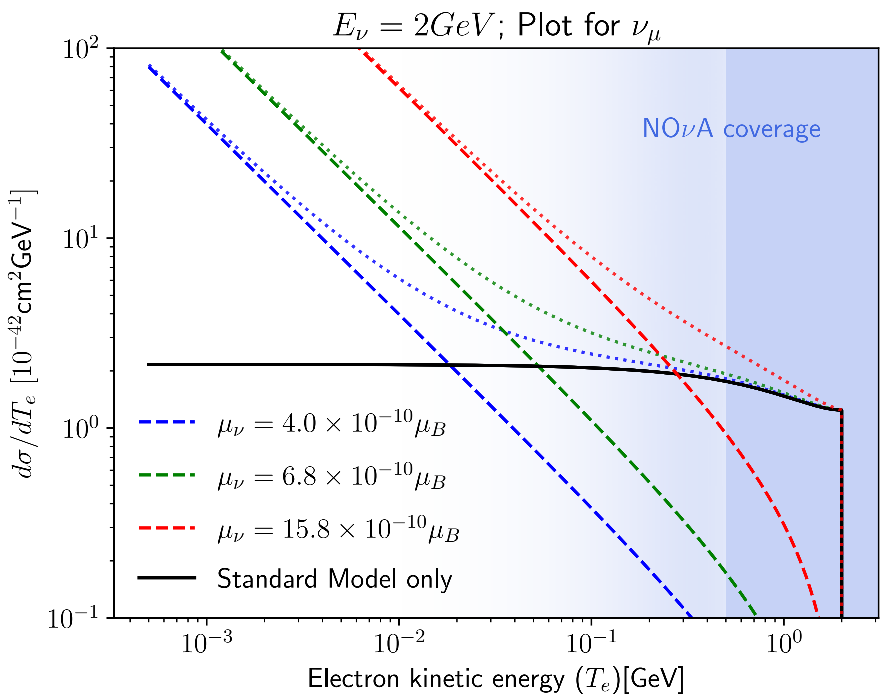

Figure 3.4: Comparison of the neutrino magnetic moment (coloured) and the SM (black) cross sections for the ν-on-e elastic scattering. Different colours depict different values of the neutrino magnetic moment, with red corresponding to the previous NOvA measurement, green the LSND result, and blue a possible ultimate NOvA sensitivity, as discussed in the introduction to this chapter. Dashed lines are the individual cross sections and dotted lines are the added total cross section with the standard model contribution. NOvA coverage of electron recoil energies is shown in shaded blue.

Calculating the ratio of the neutrino magnetic moment and the SM cross sections, as shown in Fig. 3.5, can serve as a proxy to estimate the number of neutrino magnetic moment events in relation to the predicted number of SM events, if the E_ν and T_e are known. Additionally, comparing the ratio of the total cross sections can reveal the expected total number of neutrino magnetic moment events as a function of the predicted number of SM events. Considering $E_\nu = 2\,\text{GeV}$, $\mu_\nu = 6.8 \times 10^{-10}\mu_B$ (current best limit for ν_μ from LSND), and integrating differential cross sections for ν_μ in Eq. 3.24 and 3.27 from $T_{e,min}$ to $T_{e,max} \to 2\,\text{GeV}$ results in

$$\frac{\sigma_{\text{MAG}}}{\sigma_{\text{SM}}} \approx \begin{cases} 0.035 & T_{e,min} = 0.5\,\text{GeV}, \\ 0.14 & T_{e,min} = 0.01\,\text{GeV}. \end{cases} \tag{3.28}$$

Therefore, at the current NOvA detection capabilities, there are about 0.035 times as many neutrino magnetic moment ν-on-e events than SM ones. This can be compared with the expected statistical uncertainty on the SM background, which in case of Poisson distributed events is the square root of the number of predicted events. Consequently, it is possible to assess the minimal number of SM ν-on-e events necessary for the magnetic moment signal to be detected above the SM background (without considering systematic uncertainties) as

$$N_{SM} > 1/0.035^2 \approx 816. \tag{3.29}$$

However, this approximation is calculated only for one value of E_ν, but can be used to assess the sensitivity of the experiment.

As can be seen in Fig. 3.4 and Fig. 3.5, the magnetic moment contribution exceeds the SM contribution for low enough T_e. This can be approximated as [156]:

$$T_e \lesssim \frac{\pi^2\alpha^2}{G_F^2 m_e^3}\left(\frac{\mu_\nu}{\mu_B}\right)^2 \simeq 2.9 \times 10^{19}\left(\frac{\mu_\nu}{\mu_B}\right)^2 [\text{MeV}]\,, \tag{3.30}$$

which does not depend on the neutrino energy. Therefore, experiments sensitive to lower energetic electrons are significantly more sensitive to the neutrino magnetic moment.

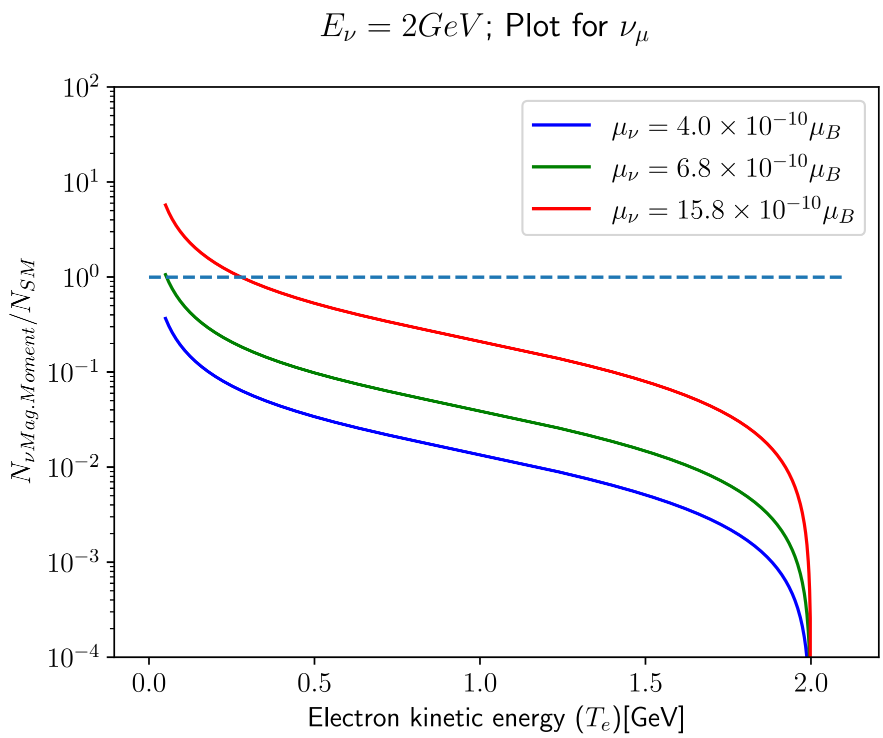

Figure 3.5: Ratio of the neutrino magnetic moment cross section to the SM cross section for the ν-on-e elastic scattering of $2\,\mathrm{GeV}$ ν_μ. Different colours depict different effective muon neutrino magnetic moment values, with red corresponding to the previous NOvA measurement, green the LSND result, and blue a possible ultimate NOvA sensitivity, as discussed in the introduction to this chapter.

3.2 Analysis overview

Our analysis strategy is to compare the count of the recorded neutrino events in data with the prediction. The prediction consists of the signal, which is directly related to the value of the neutrino magnetic moment, and the background, which corresponds to the predicted events under the SM. The signal is defined as true ν-on-e events with the neutrino magnetic moment cross section instead of the SM one. Additionally, we require the true vertex to be contained inside of the ND to remove events that originates from outside of the detector. Background is everything else.

The data used in this analysis was collected from the start of the NOvA ND data taking on the 22$^{\text{nd}}$ of August 2014, until the 3$^{\text{rd}}$ of February 2021. This is the ND data that was used in the latest NOvA neutrino oscillations result [54], with an additional one year of data taking. The ND collected more data since February 2021 which is however still being processed and it is not available at the time of writing this thesis. The full ND-equivalent exposure of the data sample is approximately 13.8×10^{20} POT. This exposure is used throughout the rest of this chapter to scale the predicted distributions and number of events. COMMENT: *Should I also talk about the RHC sample here? Future data?*

Maybe also mention something about the data that was excluded - bad runs and bad channels?

This analysis uses the standard NOvA simulation and reconstruction tools, as were discussed in Sec. 2.4 and 2.5. The simulation was created with approximately $4\times$ larger statistics than is available in data to limit statistical uncertainties from simulation. The total exposure for the simulation is approximately 55.4×10^{20} POT. However, for the studies of the systematic uncertainties, only a smaller portion of this full sample is used, specifically 19.3×10^{20} POT ND-equivalent.

The corrections for the known limitations in the simulation are applied in the form of event-by-event analysis weights, which weight each single event based on how it is affected by that particular variation in simulation. To correct for known deficiencies in simulation of neutrino flux or cross sections we apply weights calculated for each event. This includes the external measurements that correct the neutrino beam prediction inside PPFX as described in Sec. 2.4, and for the non-ν-on-e background, also the internal and external measurements that constrain the neutrino interaction prediction inside GENIE. These are not applied to the ν-on-e events, as they are assumed to be known precisely from theory. However, the GENIE MC simulation doesn't consider radiative corrections for the ν-on-e events, which are however trivial to implement.

Mention here where did I get the original GENIE cross section from (reference Yiwen's talk or technote, plus the original paper that was used). nu-on-e technote[153]

TO DO: *Write out the actual version of the weight. Including the original and the corrected XSec constants*

MINERvA paper [163]: At tree level, the neutrino-electron scattering cross section is given by... (basically same as I have in the theory) corrected for updated electroweak couplings, CLL and CLR [17] and one-loop electroweak radiative corrections as calculated in Ref. [18]. One deficiency of the calculation of Ref. [18] is that it does not contain the term in the one-loop cross section proportional to CLL CLR. This deficiency is corrected in a recent calculation [38], and that result is given below. However, as illustrated in Eq. (A1) this term also contains an additional power of m/Enu compared to the terms proportional to C2 LL and C2 LR, and the entire term is therefore negligible at the few-GeV neutrino energies of the MINERvA experiment.

Say that we are not using the third part of the correction because it is tiny and it makes no difference. (tried and tested)

[ND group's technote] In GENIE, the cross section of the nuone elastic scattering signal is calculated at the tree level. To improve the precision of the simulated nuone elastic scattering cross section, we performed radiative corrections to the GENIE nuone elastic scattering as shown in Appendix A. The precision of the simulated nuone elastic scattering cross section is improved by tuning CLL and CLR to one-loop values obtained from global fits to electroweak data 14 and 2. The radiative correction also includes additional low-energy terms in the expression of differential cross section of nuone elastic scattering. In comparison, the neutrino interactions in the NOvA detector are simulated using the GENIE neutrino event generator, where the Weinberg Angle is 0.501716712132. After radiative corrections, the total number of nuone elastic scattering increases 0.83% from the standard GENIE MC.

TO DO: *correct the equation* Calculated as

$$weight_{\text{Radiative Corr.}} = \left.\frac{d\sigma_{\nu-on-e}}{dy}\right|_{\text{Radiative Corr.}} \Big/ \left.\frac{\mathrm{d}\sigma_{\nu-on-e}}{\mathrm{d}y}\right|_{\text{GENIE 3}}; \; y = \frac{E_e - m_e}{E_\nu} \tag{3.31}$$

TO DO: *What does this do and why does it work? Reference the theory part as to why is the magnetic moment signal simply a rescaling of the GENIE cross section.*

Using the same tree-level cross section from GENIE as in the rad. corr. weight.

TO DO: *Write the name of the weight in CAFAna/nuone namespace and where it is located*

TO DO: *correct the equation* Calculated as

$$weight_{\nu\text{ Mag. Moment}} = \left.\frac{d\sigma_{\nu-on-e}}{dy}\right|_{\nu\text{ Mag. Moment}} \Big/ \left.\frac{\mathrm{d}\sigma_{\nu-on-e}}{\mathrm{d}y}\right|_{\text{GENIE 3}}; \; y = \frac{E_e - m_e}{E_\nu} \tag{3.32}$$

Due to the relatively low cross section of the ν-on-e interaction, the nominal simulation sample contains too few ν-on-e events, which could result in a significant statistical uncertainty from simulation. To avoid this, we created a ν-on-e-enhanced simulation sample which contains mainly ν-on-e events with a little non-ν-on-e background overlaid on top to properly account for the possible reconstruction effects of the pileup of neutrino interactions in one spill [153]. In the real detector, the hits from the true ν-on-e interaction can be clustered to another interaction, or additional hits can be clustered together into the ν-on-e event. The total exposure of the ν-on-e-enhanced sample is 1.72×10^{24} POT. To save up on unnecessary disk space and processing usage, the enhanced ν-on-e sample does not include any cross section related parameters and variables, as the ν-on-e interaction is assumed to be known exactly from theory.

The cross section tuning procedure in NOvA (Sec. 2.4) applies large weights to MEC events in some parts of the parameter space. However, after the full event selection described below in Sec. 3.3 there is only a small amount of MEC events, specifically ν_eCC MEC events, left in the detector. Applying large tuning corrections to only a small number of events results in large statistical fluctuations. To avoid this, we created another special sample with enhanced number of ν_eCC MEC events. We followed the same procedure as for the ν-on-e-enhanced sample, resulting in the final exposure of 1.99×10^{24} POT.

The summary of the simulation samples and analysis weights for the three different types of signal and background component is shown in Tab. 3.1.

Table 3.1: Overview of the simulation samples and analysis weight used for the different signal and background components.

Signal type	Sample	Weight
Signal	Enhanced ν-on-e	Flux & ν Mag. Moment
ν-on-e background	Enhanced ν-on-e	Flux & Rad. Corr.
ν_eCC MEC background	Enhanced ν_eCC MEC	Flux & Cross Sec.
Other background	Nominal ND	Flux & Cross Sec.

3.3 Event selection

We are searching for ν-on-e elastic scattering events, characterised by a single very forward going electron shower, specifically focusing on low electron recoil energies. The main background for our analysis come from ν_eCC interactions, which produce electron with an additional activity, and interactions that produce π^0, which decays into two photons producing electromagnetic showers, where each can look similar to the ν-on-e signal. Additionally, there are ν_μCC interactions, which are generally easy to identify from our signal, however their very high abundance in the NOvA ND makes them a dominant background nevertheless.

We explain the motivation behind each cut of the event selection and discuss their effect on the neutrino magnetic moment events below. We also consider possible improvements to the event selection for a future (re-)analysis.

The strategy for event selection is as follows. First, we remove events that failed reconstruction or data collection. Then, we apply pre-selection cuts that remove obvious background. The exact cut is selected by limiting the reduction of the signal efficiency to about $0.25\,\%$. Following this, we apply the containment cuts that remove events that are either not fully contained within the detector, or events that originate from outside of the detector, such are rock muons. Afterwards, we consider several variables that could be used for the signal selection and evaluate their combined performance for a signal selection. We choose cut values that result in the best statistical significance, based on a chosen Figure Of Merit (FOM). Given that we are searching for a very limited number of signal events on top of a large background, we chose a simple statistics-only FOM

$$\text{FOM} = \frac{\text{Signal}}{\sqrt{\text{Background}}}. \tag{3.33}$$

The summary of the cut values for the event selection of neutrino magnetic moment signal is presented in Tab. 3.2, showing the label for the event selection variable, its description and the cut value chosen. These event selection in total reduces signal $44.51\,\%$, ν-on-e background $70.40\,\%$ and other background $99.97\,\%$. After the full event selection, the predicted number of signal events for $\mu_\nu = 10^{-9}\mu_B$ is 23.31 and the total number of background events under the SM hypothesis is 678.26. The most likely improvement is in probing the low energetic events and making sure they make sense. Additionally, it is possible to use a specially designed control regions to mitigate the very high non-ν-on-e background.

3.3.1 Data Collection Quality

To ensure good data quality, we apply the following criteria to data only. These involve the the spill time cut, at least 2^{12} POT per spill, the current in the focusing horn within $-202\,\text{kA} < I_{Horn} < -196.4\,\text{kA}$, position of the beam is within $\pm 2\,\text{cm}$ in both x and y axis and that the width of the beam is within 0.57 and $1.58\,\text{cm}$. Additionally, we remove events that are incomplete, or with problems in one or more DCMs. TO DO: *Reference the 3f data quality technote*

3.3.2 Reconstruction Quality

Since electron are reconstructed by slicing, then vertexing, then reconstructing prongs. To identify electron we request that there is a valid reconstructed vertex and at least one reconstructed prong. Even though electrons only consist of a single shower, we don't reject events with more than one prongs in a slice, as the reconstruction can wrongly assign noise hits as a separate prong. We do not want to reject these events as we might still recover the true signal event from there.

Figure 3.6 and Tab. 3.3 show that about $67\,\%$ signal events do not have a valid reconstructed vertex. This is due to the concentration of the signal events at very low electron recoil energies, which can often consist of a single hit or only a few hits. As can be seen in the bottom plot of Fig. 3.6, events with small true electron recoil energy have much smaller vertex reconstruction efficiency than higher energetic electrons. However, improving NOvA vertex reconstruction at low energies might significantly aid the search for the neutrino magnetic moment. Ongoing work is improving the

Table 3.2: Summary of the cut values for the event selection of neutrino magnetic moment signal showing the label for the event selection variable, its description and the cut value chosen. COMMENT: *Should I include the loose cuts here even when they were made stricter during TMVA?*

Label	Description	Cut
Valid Vtx	Valid reconstructed vertex	> 0
N^o Prongs	Number of reconstructed prongs	> 0
Hits / Plane	Number of hits per plane	< 5
Low E_{Shower}	Low cut on calorimetric energy of the most energetic shower	$> 0.5\,\mathrm{GeV}$
N^o Hits Loose	Preliminary cut on the total number of hits for all prongs in a slice	< 200
Prong Length	Length of the longest prong	$< 540\,\mathrm{cm}$
$E\theta^2$ **Loose**	Preliminary cut on the product of the calorimetric energy and angle squared of the leading shower	$< 0.05\,\mathrm{GeV} \times \mathrm{rad}^2$
High E_{Shower} Loose	Preliminary upper cut on the calorimetric energy of the most energetic shower	$< 5.5\,\mathrm{GeV}$
Fiducial	Vertex x position	$> -177\,\mathrm{cm}$ $< 177\,\mathrm{cm}$
	Vertex y position	$> -177\,\mathrm{cm}$ $< 177\,\mathrm{cm}$
	Vertex z position	$> 50\,\mathrm{cm}$ $< 1050\,\mathrm{cm}$
Containment	Minimum hit position in x	$> -177\,\mathrm{cm}$
	Maximum hit position in x	$< 177\,\mathrm{cm}$
	Minimum hit position in y	$> -185\,\mathrm{cm}$
	Maximum hit position in y	$< 177\,\mathrm{cm}$
	Minimum hit position in z	$> 55\,\mathrm{cm}$
	Maximum hit position in z	$< 1270\,\mathrm{cm}$
E_{Shower}/E_{Tot}	Fraction of energy contained in the most energetic shower	> 0.91
N^o Hits	Total number of hits for all prongs in a slice	< 116
High E_{Shower}	Calorimetric energy of the most energetic shower	$< 1.4\,\mathrm{GeV}$
ν-on-e ID	CVN-based ν-on-e identifier	> 0.65
$E\pi^0$ **ID**	CVN-based ν-on-e and π^0 identifier	> 0.63
$E\theta^2$	Product of the calorimetric energy and angle squared of the leading shower	$< 0.0048\,\mathrm{GeV} \times \mathrm{rad}^2$

vertex reconstruction by using ML approach instead of the currently used Hough transform together with Elastic Arms [164].

Additionally, we're placing a cut on the number of hits per plane to < 5. This is to remove the so-called 'FEB flashers', which are caused by a very high energy deposit in one cell, such that it affects all the other channel on the same APD [165]. The cut value was chosen so that it removes $\leq 0.25\,\%$ signal events, which is the same criterion as is used for the basic event selection cuts described below. Relative comparisons between signal and background for the number of prongs and the number of hits per plane are shown in Fig. 3.7.

COMMENT: *Already applying the cut here to help reduce the events for TMVA. This cut is based purely on reco quality (we don't trust events below 0.5GeV, especially not for the CVN nuone ID variables*

TO DO: *discuss the energy cut, should this be removed? What is the effect on the event count? Why was this included in the first place (the identifiers are not as strong for lower energies - is this true though? - also there are further unexplored backgrounds that would need to be further studied and explore. Maybe depends on where would we move the cut...)*

The reconstructed calorimetric energy of the primary shower is required to be $E_{cal} > 0.5\,\mathrm{GeV}$ as shown in Fig. 3.8. This is to remove region in the parameter space with large backgrounds. However, due to the nature of the neutrino magnetic moment signal, this cut also removes a majority of our signal events (exactly how much?).

This is due to a presence of large background that has not been studied very well. No NOvA analysis really uses events with such low energies. However, after further studies and validation, it is likely that these cut can be pushed to lower electron recoil energy, especially by using better event identifiers to remove the large background there.

NOvA is not super well suited for a low energy detection and there are troubles identifying very low energetic event. Majority of the analyses in NOvA only use events with energies above $0.5\,\mathrm{GeV}$. nueCCXSec only uses events above 1 GeV. The numuCCpi0 XSec ana had a low E cutoff at 0.1GeV

COMMENT: *How does the energy resolution and bias come into play here? 0.5GeV*

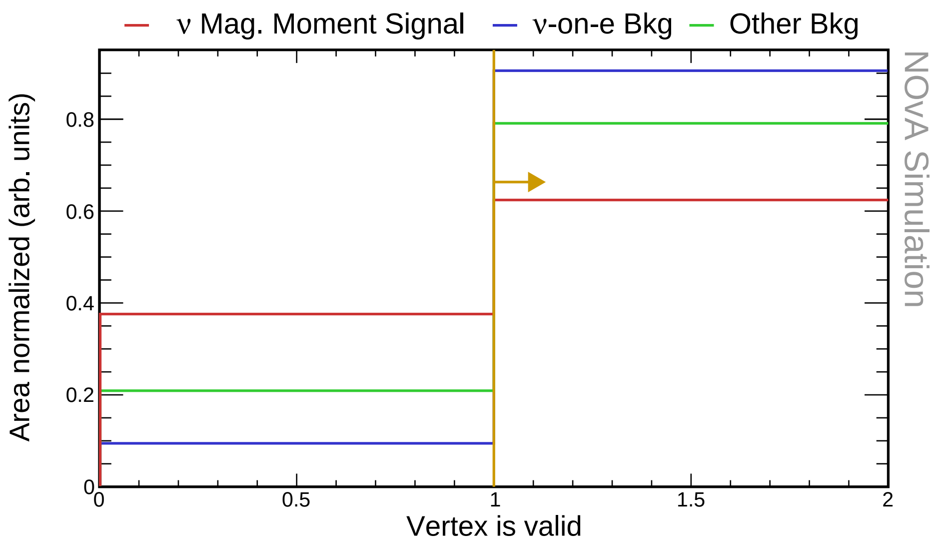

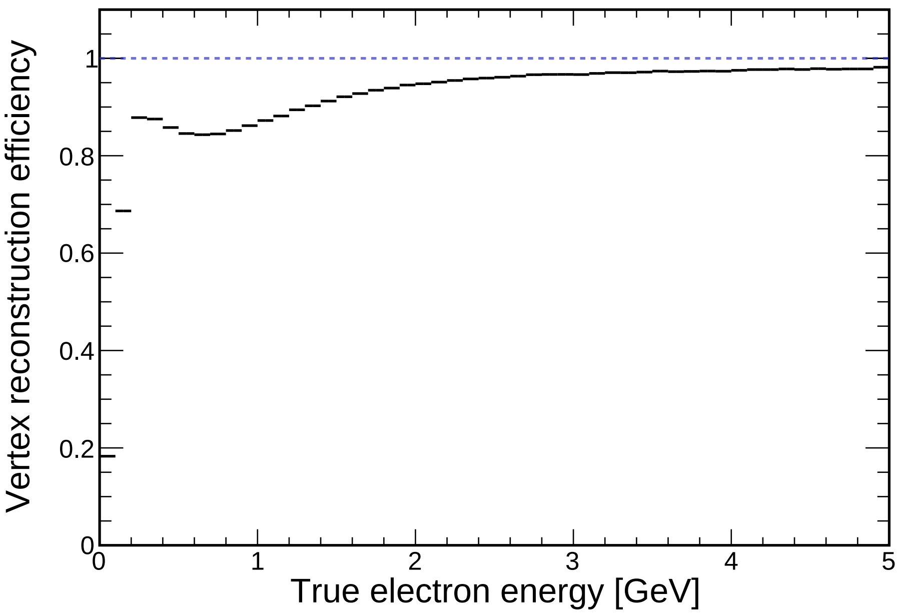

Figure 3.6: Top: Relative comparison of the signal (red), ν-on-e background (blue), and other background (green) events for the vertex reconstruction quality selection. Each histogram is area-normalised and the first bin corresponds to events without a valid vertex and second bin to events with correctly reconstructed vertex. The yellow line indicates the chosen cut value: all events have to have a valid reconstructed vertex. Bottom: profile histogram of the 'vertex is valid' variable as a function of the true electron energy for the true signal events, showing the significant drop in vertex reconstruction efficiency at low electron recoil energies. No selection was applied prior to making these plots.

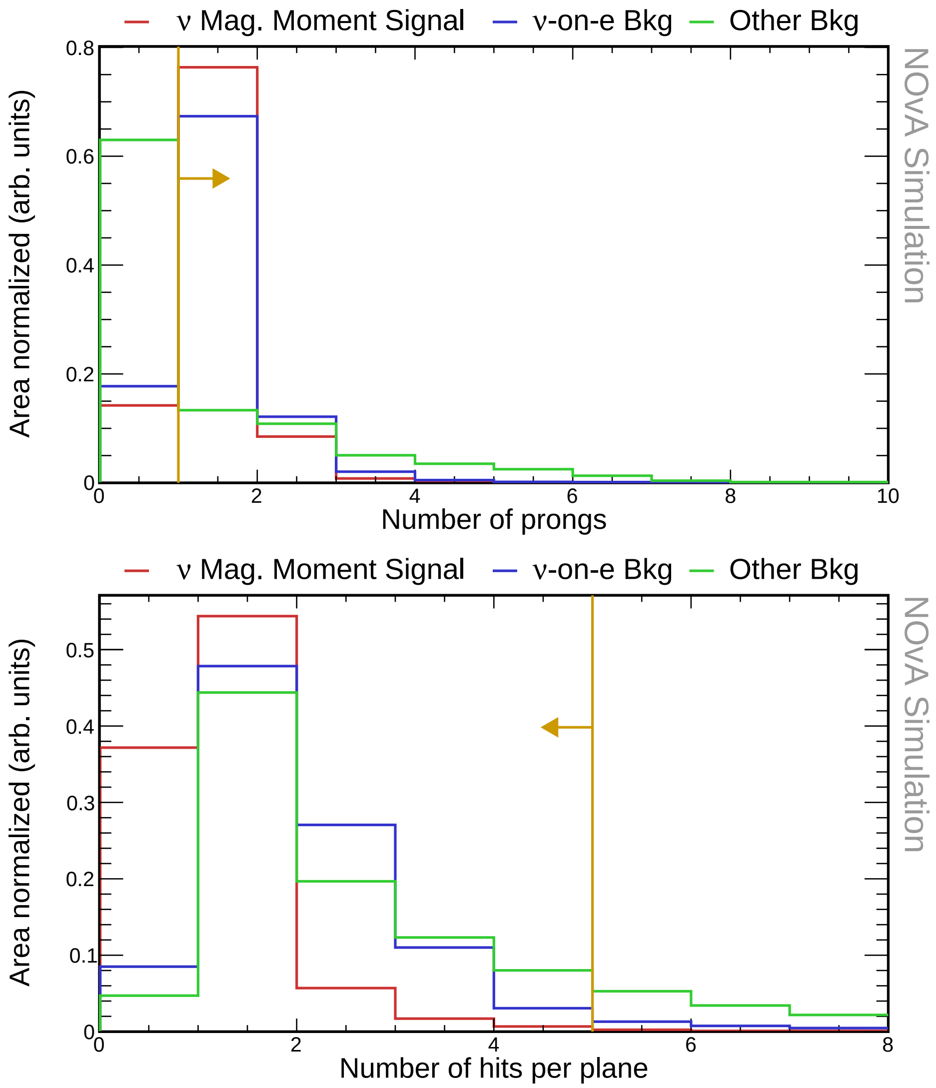

Figure 3.7: Relative comparison of signal (red), ν-on-e background (blue), and other background (green) events in the number of prongs (top) and the number of hits per plane (bottom) distributions. Events in both plots are required to have a valid reconstructed vertex and in the bottom plot also at least one reconstructed prong. Yellow lines indicate the cut values for the shown variables, with arrows pointing towards the preserved events. All histograms are area-normalised.

for us is not the same as for the 3fl or for some other ND analyses. This needs to be properly investigated in the future

Maybe also say that Test Beam will be crucial in improving the vertex and energy resolution within NOvA, including electrons.

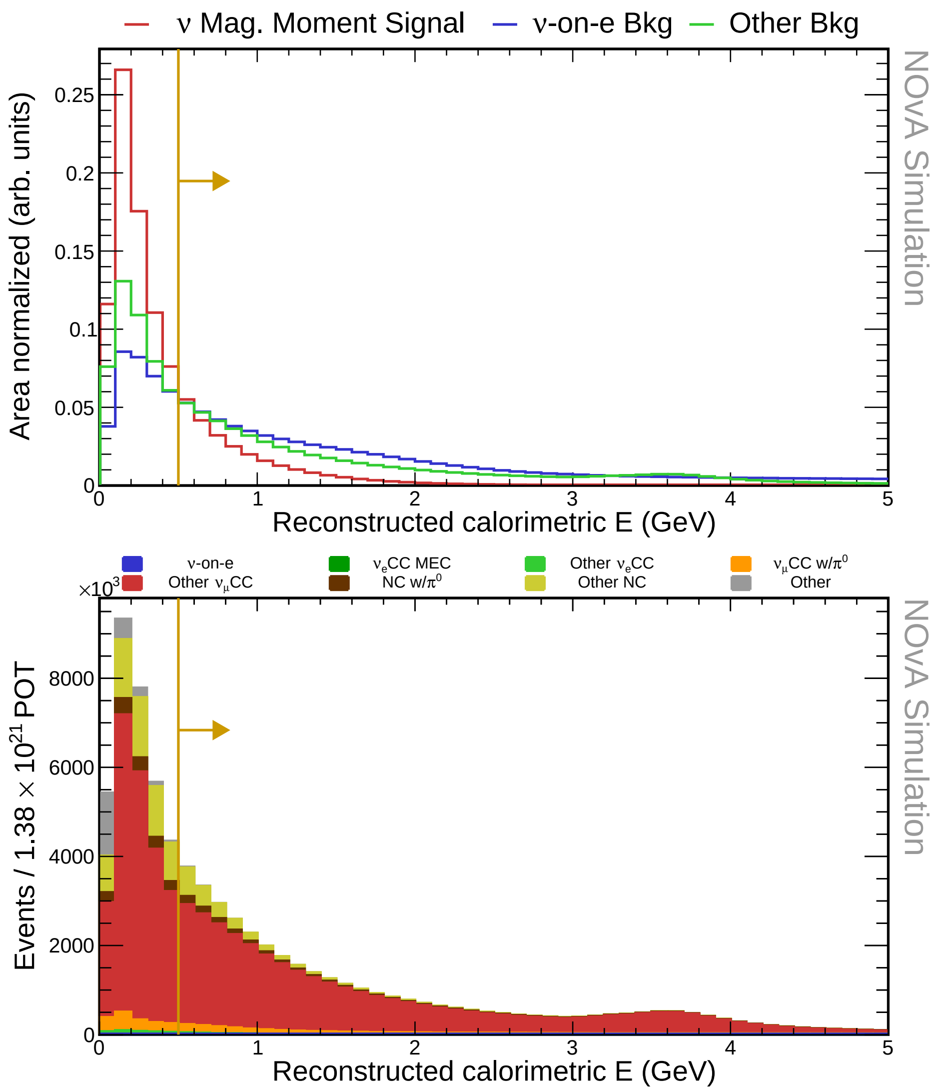

Figure 3.8: Top: Relative comparison of signal (red), ν-on-e background (blue), and other background (green) events in the reconstructed calorimetric energy distribution. All histograms are area-normalised. Bottom: Decomposition of background into various sub-samples, normalised to the data POT exposure. Events in both plots are required to have a valid reconstructed vertex, at least one reconstructed prong and at most 5 hits per plane. Yellow lines indicate the cut value for the reconstructed calorimetric energy, with arrows pointing towards the preserved events.

3.3.3 Basic Event Selection

Basic event selection cuts aim to remove obvious background events without affecting the signal too much. The criterion for these cuts will be that each of them has to limit the signal efficiency by approximately $0.25\,\%$. This means that in total the pre-selection cuts will lower the signal efficiency by only approximately $1\,\%$. We are using the same variables for these cuts as were used in the event selection for the ν_e appearance ND constraint for the three flavour neutrino oscillation measurements [54]. Additionally, we are also using a cut on the product of the reconstructed calorimetric energy and the square of the reconstructed angle between the recoil electron and the neutrino beam direction. The electron is assumed to be the most energetic reconstructed showers. The reconstructed showers are ordered based on their deposited energies, therefore the first reconstructed prong is assumed to be the most energetic. In case of the ν-on-e events, this should be the electron.

They also remove the obvious ν_μCC interactions by requiring that the summed number of cells for all prongs in the slice is < 200 and the length of the longest prong is < 540 cm. Relative comparison of signal, ν-on-e background, and other background distributions for the pre-selection variables is shown on Fig. **??**.

Additionally, as discussed in Sec. 3.1.2, from theory we know what the true recoil electron for the ν-on-e interaction is supposed to be limited by $E\theta^2 < 2m_e$. Due to reconstruction deficiencies, the reconstructed $E\theta^2$ will not have such a strict cut-off for ν-on-e events, this variable can however be used to distinguish them from the ν_eCC events, for which the electron has a much more isotropic distribution.

Table 3.3: Event selection cutflow table for the reconstruction quality cuts showing the number of events and the relative efficiency of each cut for each signal sample. The relative efficiency is calculated as number of events remaining after applying the corresponding cut divided by number of event for all the previous cuts. All the cuts are listed in sequence as they are applied.

Selection	**Signal**		**ν-on-e bkg**		**Other bkg**	
	N_{evt}	ϵ_{rel} (%)	N_{evt}	ϵ_{rel} (%)	N_{evt}	ϵ_{rel} (%)
No Cut	269.77	100	3.43×10^3	100	2.96×10^8	100
Valid Vtx	180.58	66.94	3.33×10^3	96.94	2.34×10^8	79.10
N^o Prongs	174.69	96.74	3.23×10^3	96.99	8.66×10^7	37.00
Hits / Plane	174.36	99.81	3.22×10^3	93.83	7.32×10^7	84.55
Low E_{Shower}	48.75	27.96	2.71×10^3	84.10	4.06×10^7	55.52

On top of that, we are also placing a loose cut on the maximum calorimetric energy, as the signal is limited to low energies, as can be seen in Fig. 3.11.

Some of the signal events can be reconstructed with the opposite direction than the beam. These events might still be useful though and we want to keep them. For that reason, we are calculating the angle between the outgoing electron and the neutrino beam direction as acos (abs ($\cos\theta$)), which gives the same value whether the shower is reconstructed forward or backwards.

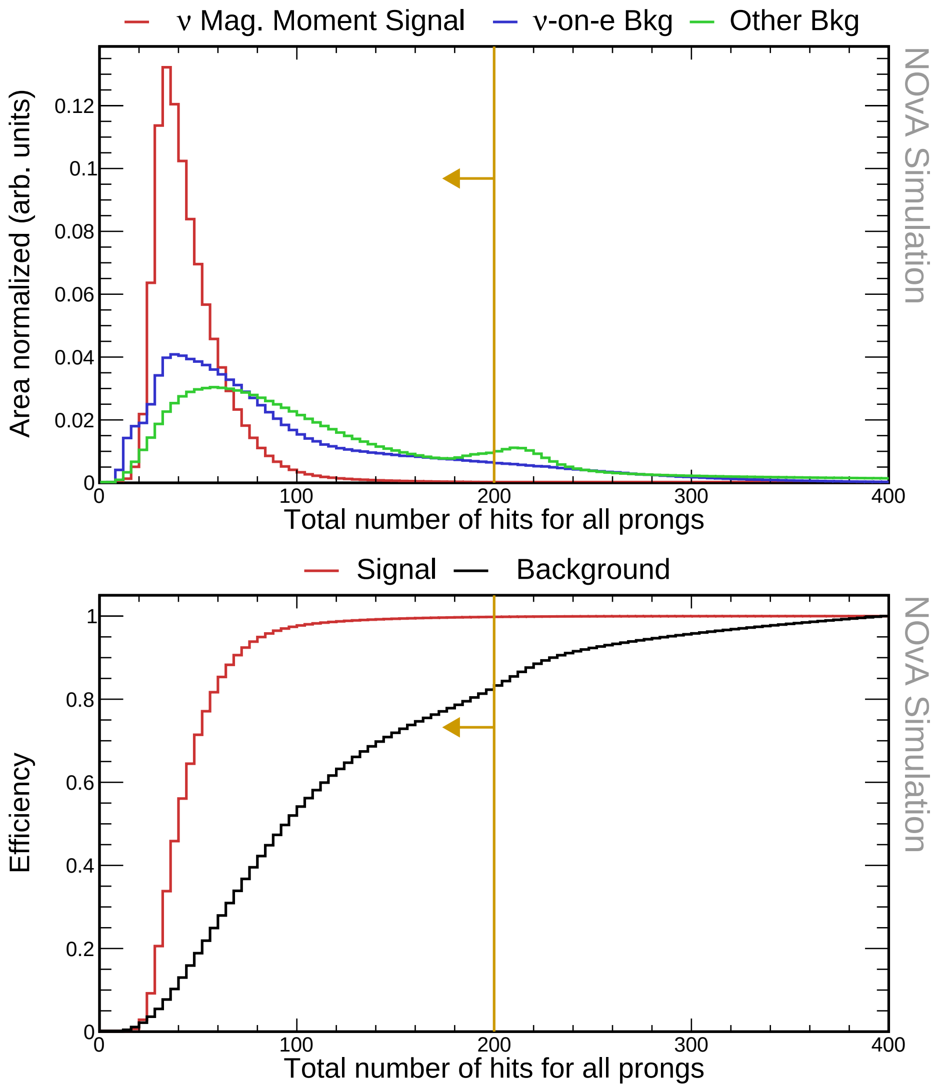

Figure 3.9: Top: Relative comparison of signal (red), ν-on-e background (blue), and other background (green) events in the distribution of total number of hits from all reconstructed prongs in the slice. All histograms are area-normalised. Bottom: Cumulative signal (red) and background (black) efficiency calculated as number of signal/background events left of the bin divided by the total number of signal/background events. Yellow lines indicate the cut value for the maximum number of hits, with arrows pointing towards the preserved events. The reconstruction quality cuts were applied before making these plots.

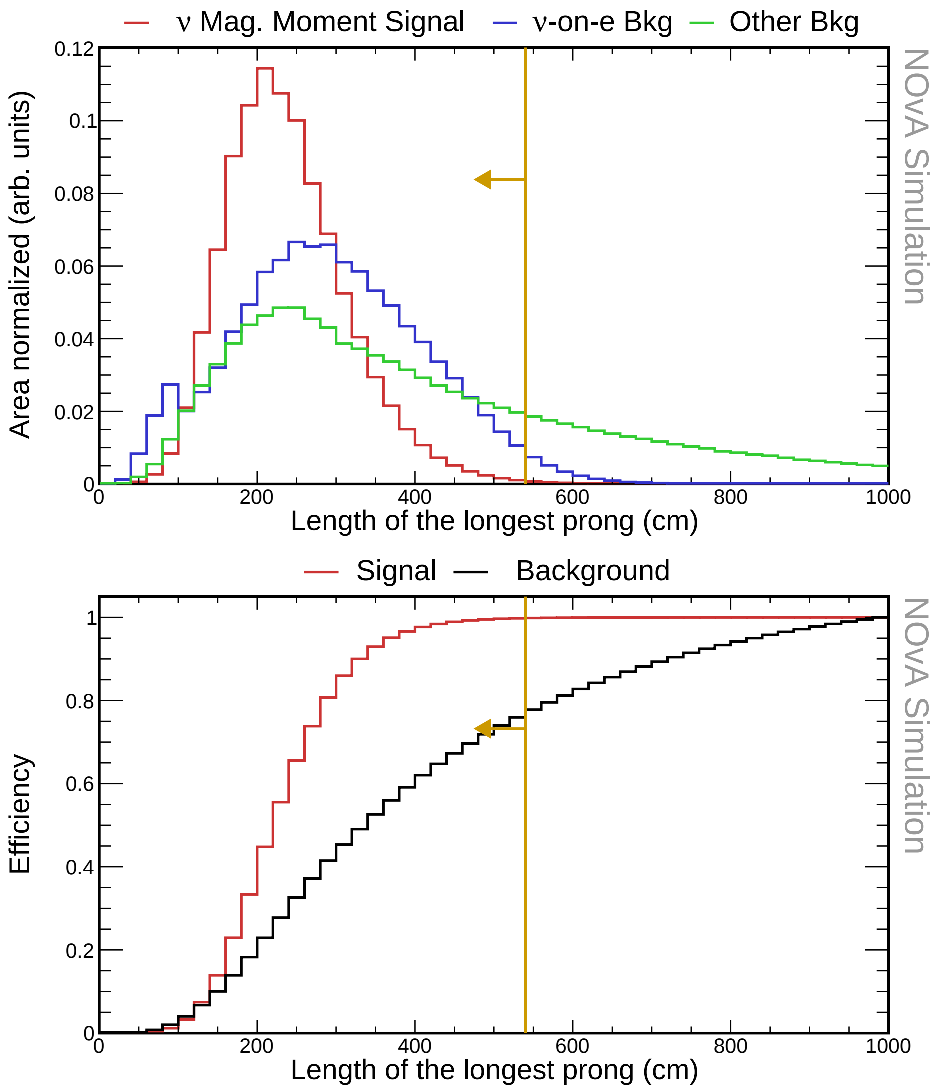

Figure 3.10: Top: Relative comparison of signal (red), ν-on-e background (blue), and other background (green) events in the distribution of the length of the longest reconstructed prong in slice. All histograms are area-normalised. Bottom: Cumulative signal (red) and background (black) efficiency calculated as number of signal/background events left of the bin divided by the total number of signal/background events. Yellow lines indicate the cut value for the maximum length of the longest prong, with arrows pointing towards the preserved events. The reconstruction quality cuts and the number of hits cut were applied before making these plots.

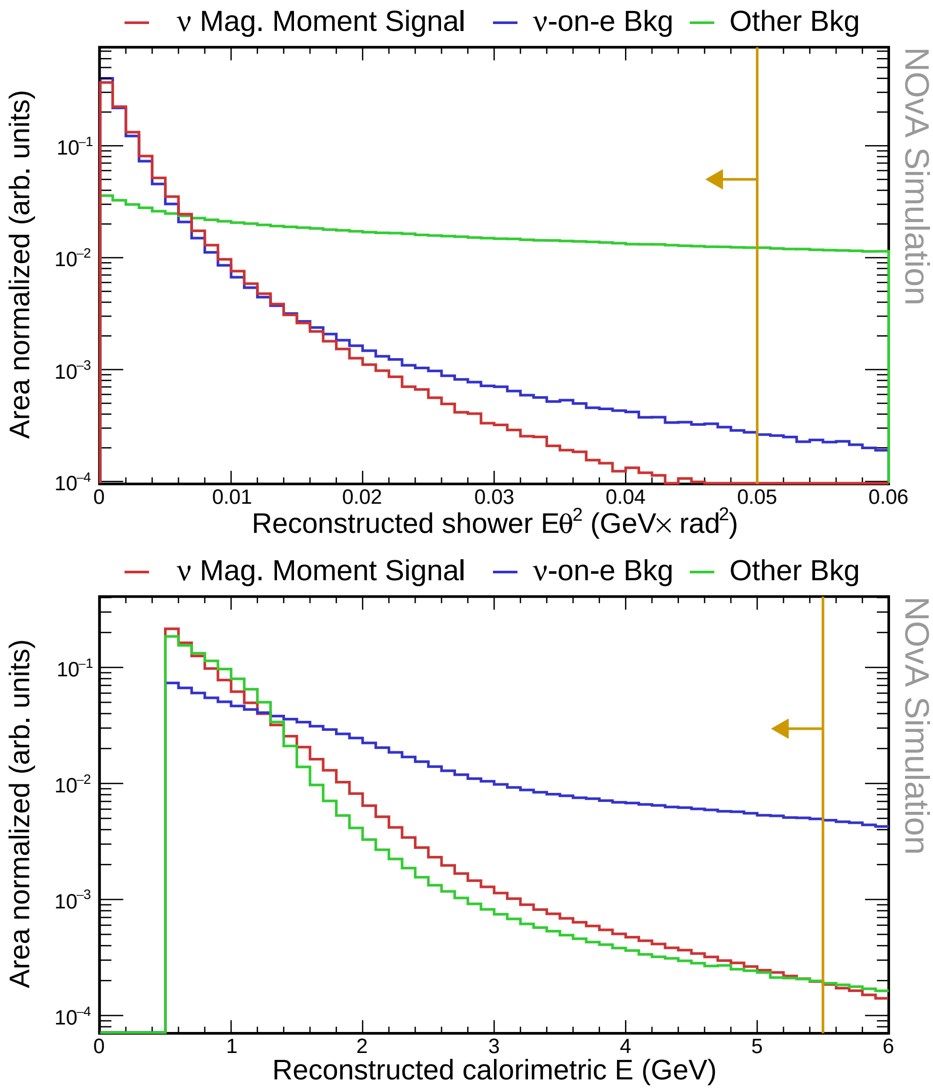

Figure 3.11: Relative comparison of signal (red), ν-on-e background (blue), and other background (green) events in the distribution of the reconstructed energy of the leading shower multiplied by its angle from the incoming neutrino beam direction squared (top) and of the reconstructed energy of the leading shower (bottom). All histograms are area-normalised with logarithmic y axis. Yellow lines indicate the cut value for the corresponding variables, with arrows pointing towards the preserved events. The reconstruction quality cuts, the number of hits cut, and the length of the longest prong cuts were applied before making both of these plots, while the hits in the bottom plot are also required to pass the $E\theta^2$ cut.

3.3.4 Fiducial and containment cuts

[nueXSec ana, docdb:37668] For both the X and Y vertices the distributions are asymmetric when comparing across the origin, in terms of vertex position. This is primarily due to particles coming from the +y and -x from events in the rock surrounding the detector. This corresponds to the direction of the NuMI target from the near detector. ...We require all activity from neutrino activity be deposited outside of the muon catcher.

TO DO: *Describe what does the fiducial cut do* We require that the reconstructed vertex is contained within the following volume: $-175 < \mathsf{Vtx}_X < 175, -175 < \mathsf{Vtx}_Y < 175, 95 < \mathsf{Vtx}_Z < 1095$ cm.

To ensure all the energy is contained within the detector and to remove events originating outside of the detector (rock muons), we require that the extreme positions of hits for all prongs in the slice are within the following volume: $-175 < \mathsf{min}_X, \mathsf{max}_X < 175, -175 < \mathsf{min}_Y, \mathsf{max}_Y < 175, 105 < \mathsf{min}_Z, \mathsf{max}_Z < 1270$ cm. COMMENT: *Also made this a bit stricter from the ND group's values as it didn't really make sense*

3.3.5 Event Selection Optimization

COMMENT: *This is where I started the TMVA*

Table 3.4: Basic event selection cutflow table showing the number of events and the relative efficiency of each cut for each signal sample. The relative efficiency is calculated as number of events remaining after applying the corresponding cut divided by number of event for all the previous cuts. All the cuts are listed in sequence as they are applied. The top row corresponds to the sample after applying the reconstruction quality cuts.

Selection	**Signal**		**ν-on-e bkg**		**Other bkg**	
	N_{evt}	ϵ_{rel} (%)	N_{evt}	ϵ_{rel} (%)	N_{evt}	ϵ_{rel} (%)
Reco Quality	48.75	100	2.71×10^3	100	4.06×10^7	100
N^o Hits Loose	48.64	99.78	2.32×10^3	85.63	3.08×10^7	75.67
Prong Length	48.52	99.75	2.26×10^3	97.39	2.17×10^7	70.66
$E\theta^2$ Loose	48.39	99.73	2.25×10^3	99.71	6.00×10^6	27.62
High E_{Shower} Loose	48.27	99.76	2.03×10^3	90.04	5.98×10^6	99.67

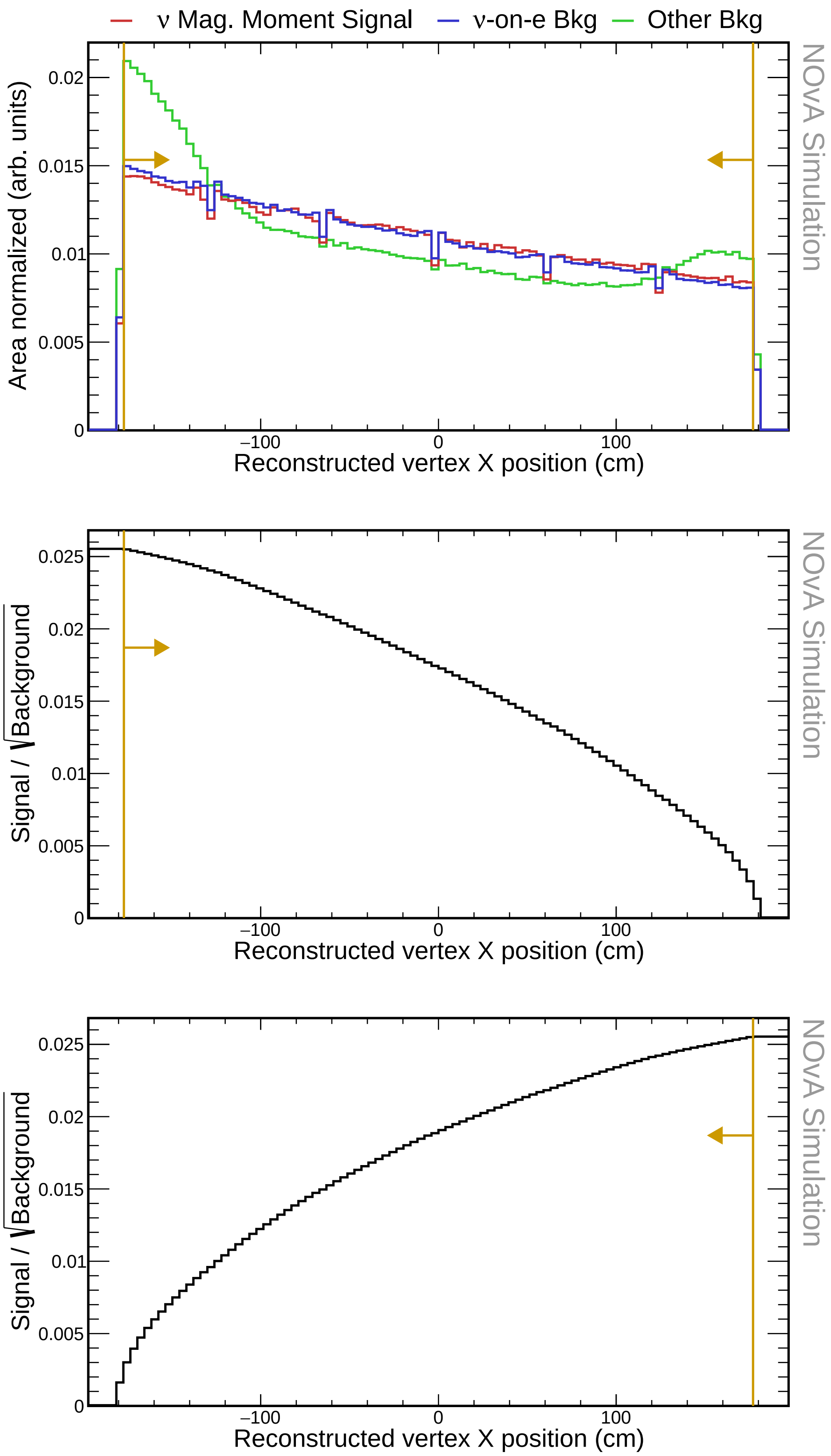

Figure 3.12: Top: Relative comparison of signal (red), ν-on-e background (blue), and other background (green) events in the distribution of the x position of the reconstructed vertex. All histograms are area-normalized. Middle and bottom: Cumulative FOM calculated as the number of signal events, divided by the number of background events from that bin until the end of the plot in the direction of the yellow arrow. The reconstruction quality and basic selection cuts were applied prior to making these plots. Additionally, vertex is required to be within the active region of the detector ($Vtx_Z < 1270\,\mathrm{cm}$). Yellow lines show the cut values that create the fiducial volume, with arrows pointing towards the preserved events.

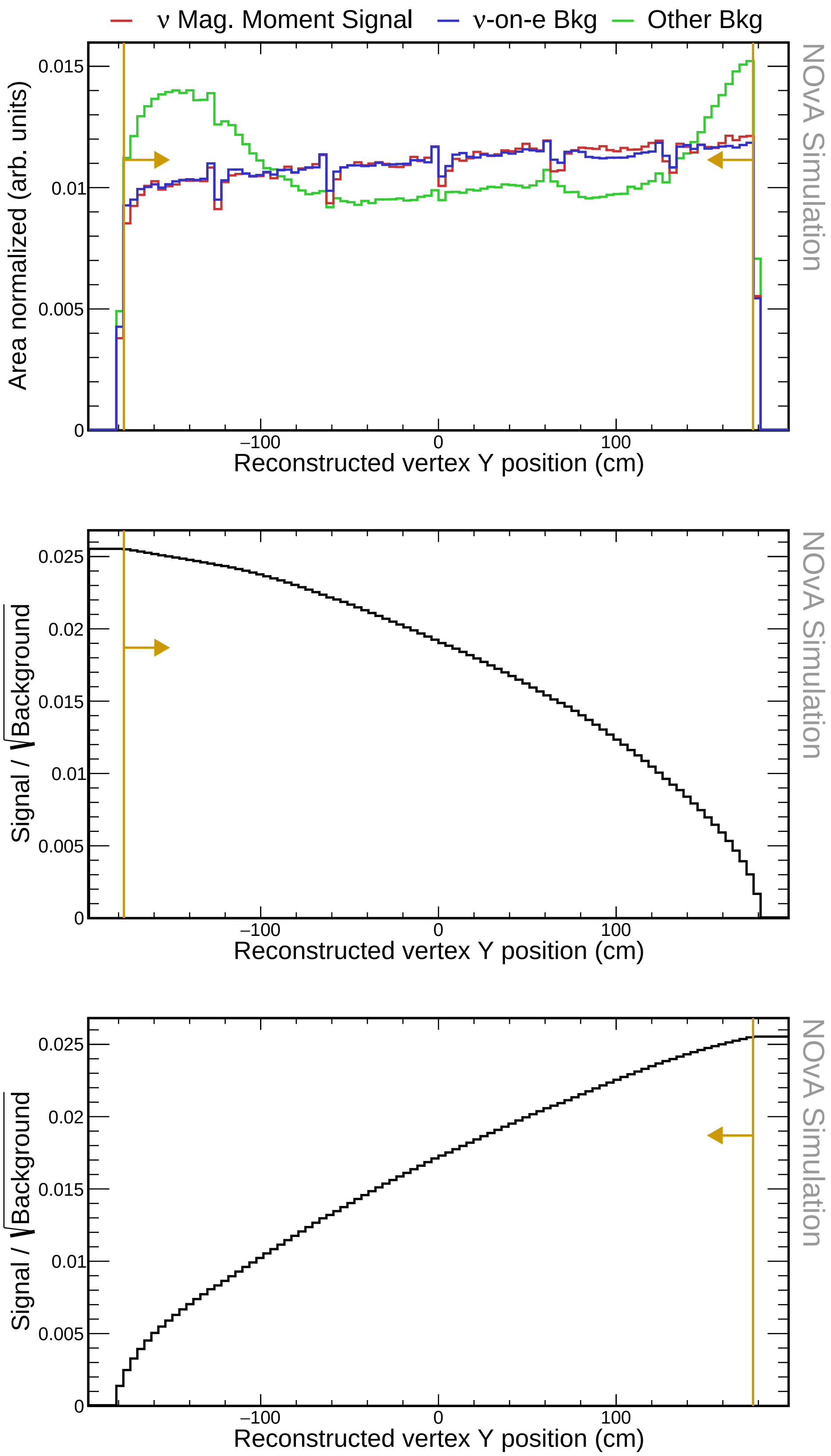

Figure 3.13: Top: Relative comparison of signal (red), ν-on-e background (blue), and other background (green) events in the distribution of the y position of the reconstructed vertex. All histograms are area-normalized. Middle and bottom: Cumulative FOM calculated as the number of signal events, divided by the number of background events from that bin until the end of the plot in the direction of the yellow arrow. The reconstruction quality and basic selection cuts were applied prior to making these plots. Additionally, vertex is required to be within the active region of the detector ($Vtx_Z < 1270\,\mathrm{cm}$). Yellow lines show the cut values that create the fiducial volume, with arrows pointing towards the preserved events.

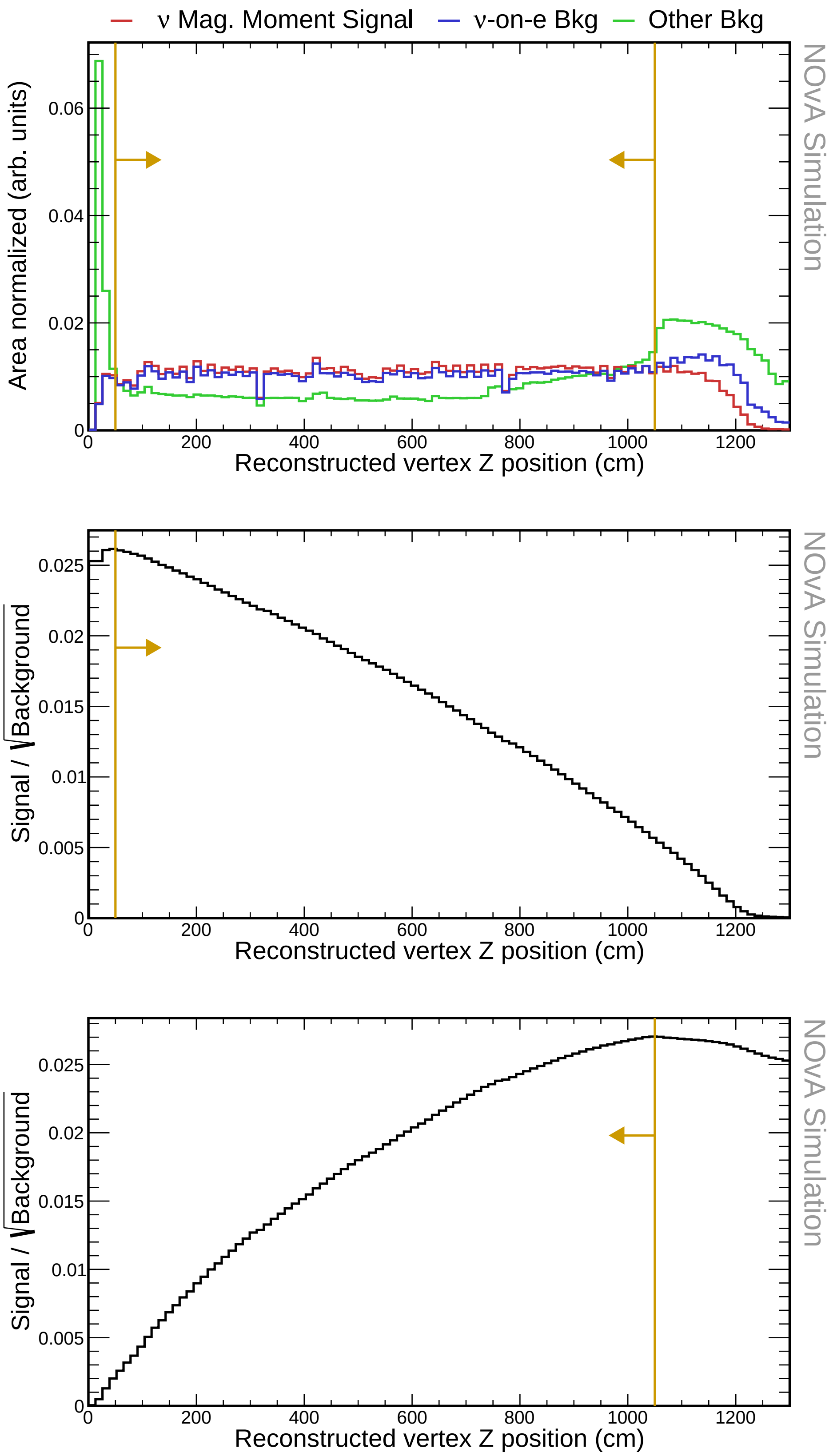

Figure 3.14: Top: Relative comparison of signal (red), ν-on-e background (blue), and other background (green) events in the distribution of the z position of the reconstructed vertex. All histograms are area-normalized. Middle and bottom: Cumulative FOM calculated as the number of signal events, divided by the number of background events from that bin until the end of the plot in the direction of the yellow arrow. The reconstruction quality and basic selection cuts were applied prior to making these plots. Yellow lines show the cut values that create the fiducial volume, with arrows pointing towards the preserved events.

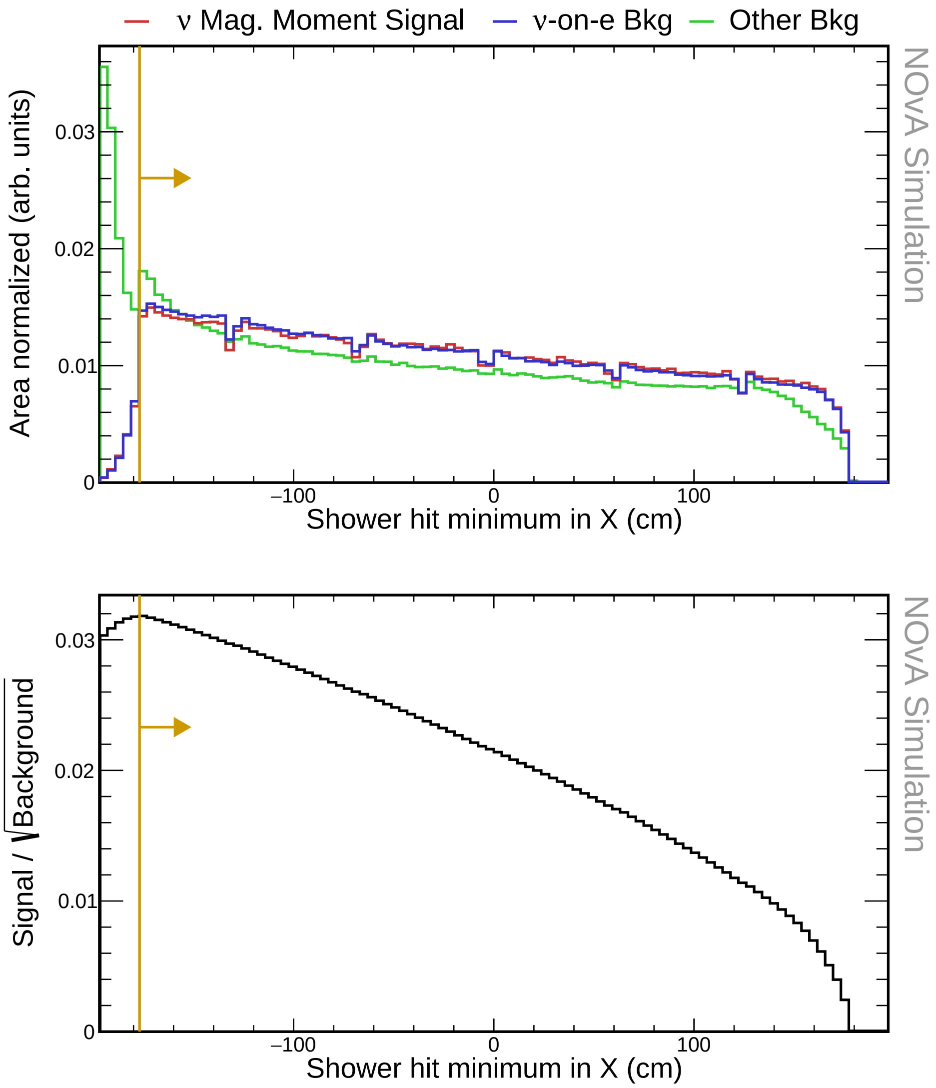

Figure 3.15: Relative comparison of signal, ν-on-e background, and other background events for the minimum and maximum position of the reconstructed shower along the x axis. Pre-selection and fiducial cuts were applied to make these plots. Gold lines show the values of the containment cuts.

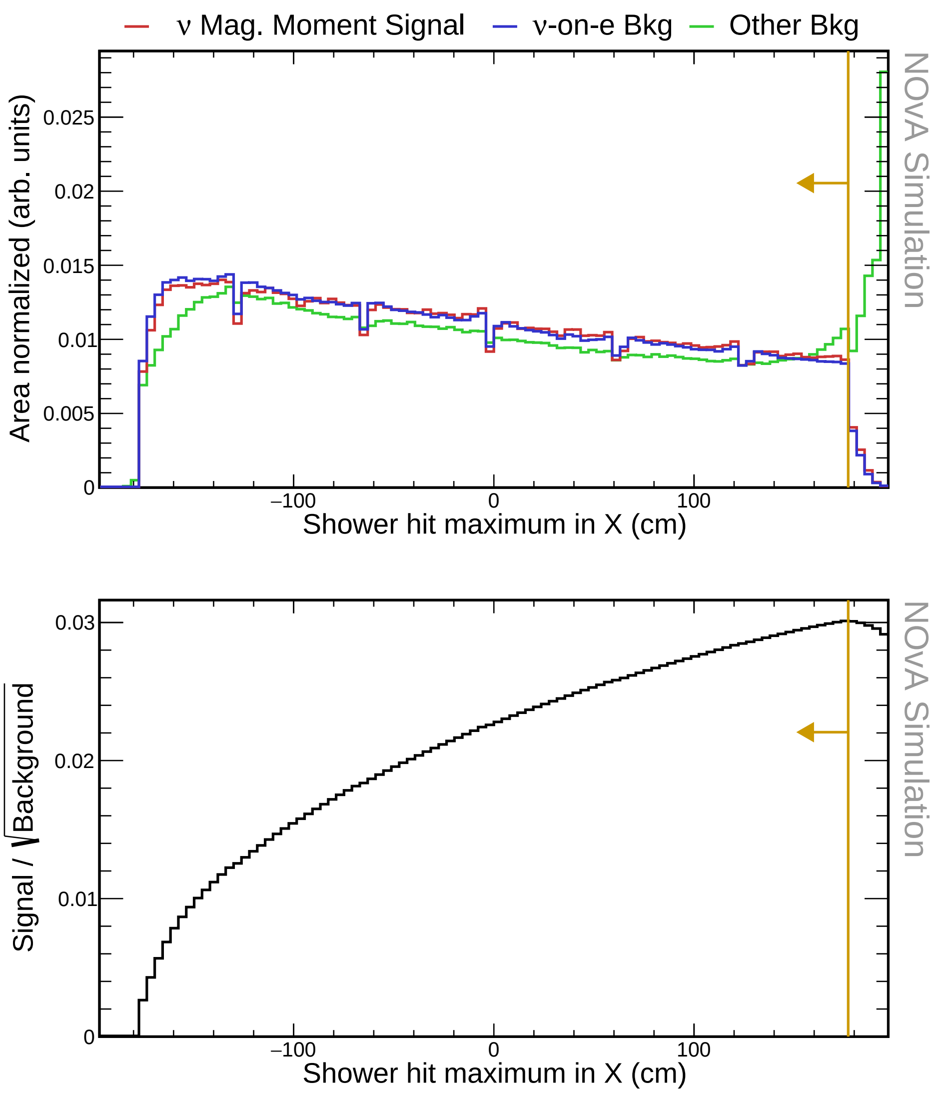

Figure 3.16: Relative comparison of signal, ν-on-e background, and other background events for the minimum and maximum position of the reconstructed shower along the x axis. Pre-selection and fiducial cuts were applied to make these plots. Gold lines show the values of the containment cuts.

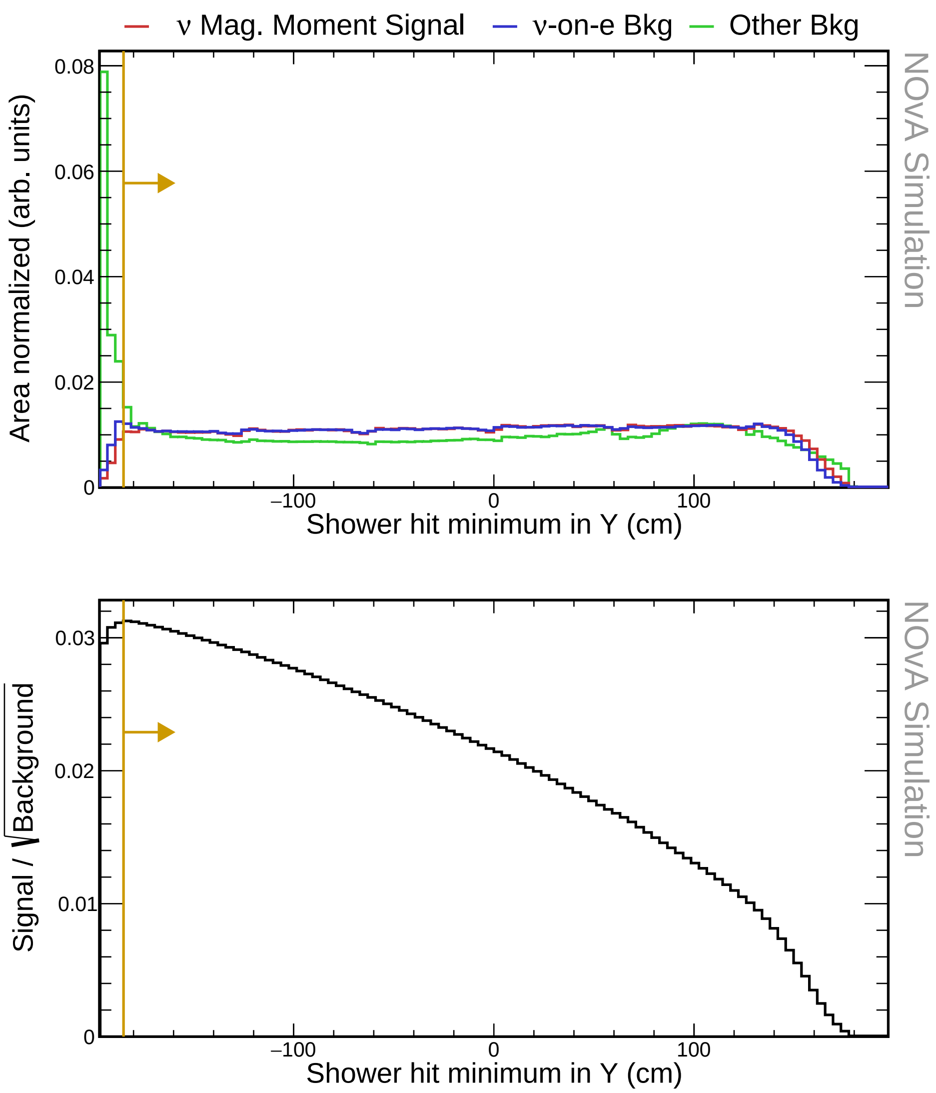

Figure 3.17: Relative comparison of signal, ν-on-e background, and other background events for the minimum and maximum position of the reconstructed shower along the y axis. Pre-selection and fiducial cuts were applied to make these plots. Gold lines show the values of the containment cuts.

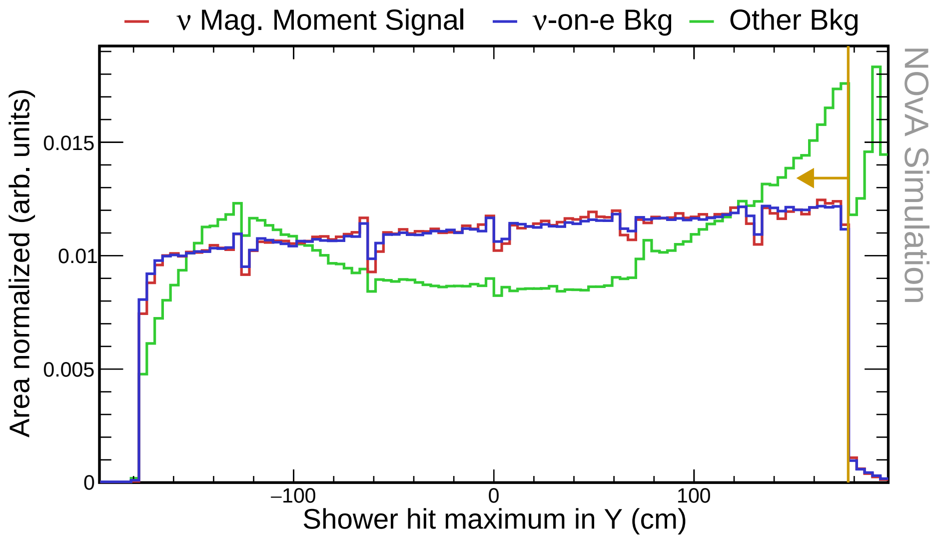

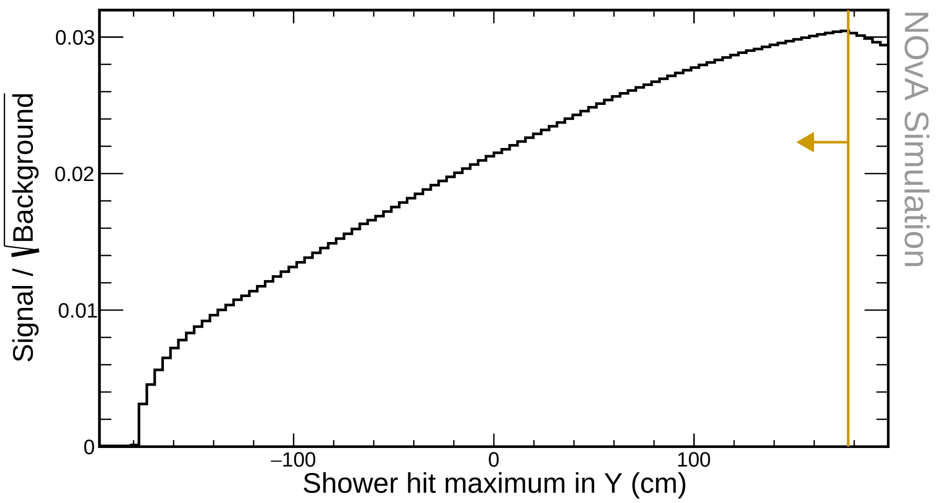

Figure 3.18: Relative comparison of signal, ν-on-e background, and other background events for the minimum and maximum position of the reconstructed shower along the y axis. Pre-selection and fiducial cuts were applied to make these plots. Gold lines show the values of the containment cuts.

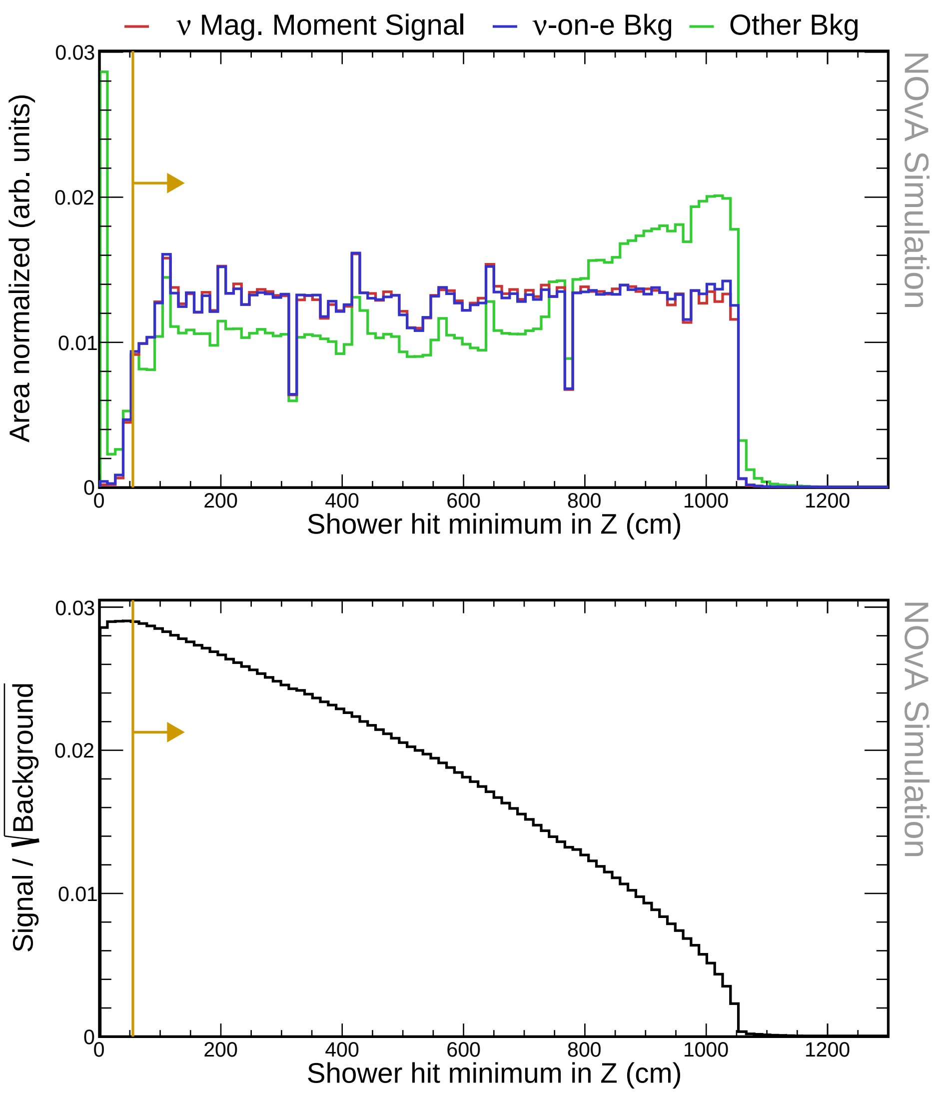

Figure 3.19: Relative comparison of signal, ν-on-e background, and other background events for the minimum and maximum position of the reconstructed shower along the z axis. Pre-selection and fiducial cuts were applied to make these plots. Gold lines show the values of the containment cuts.

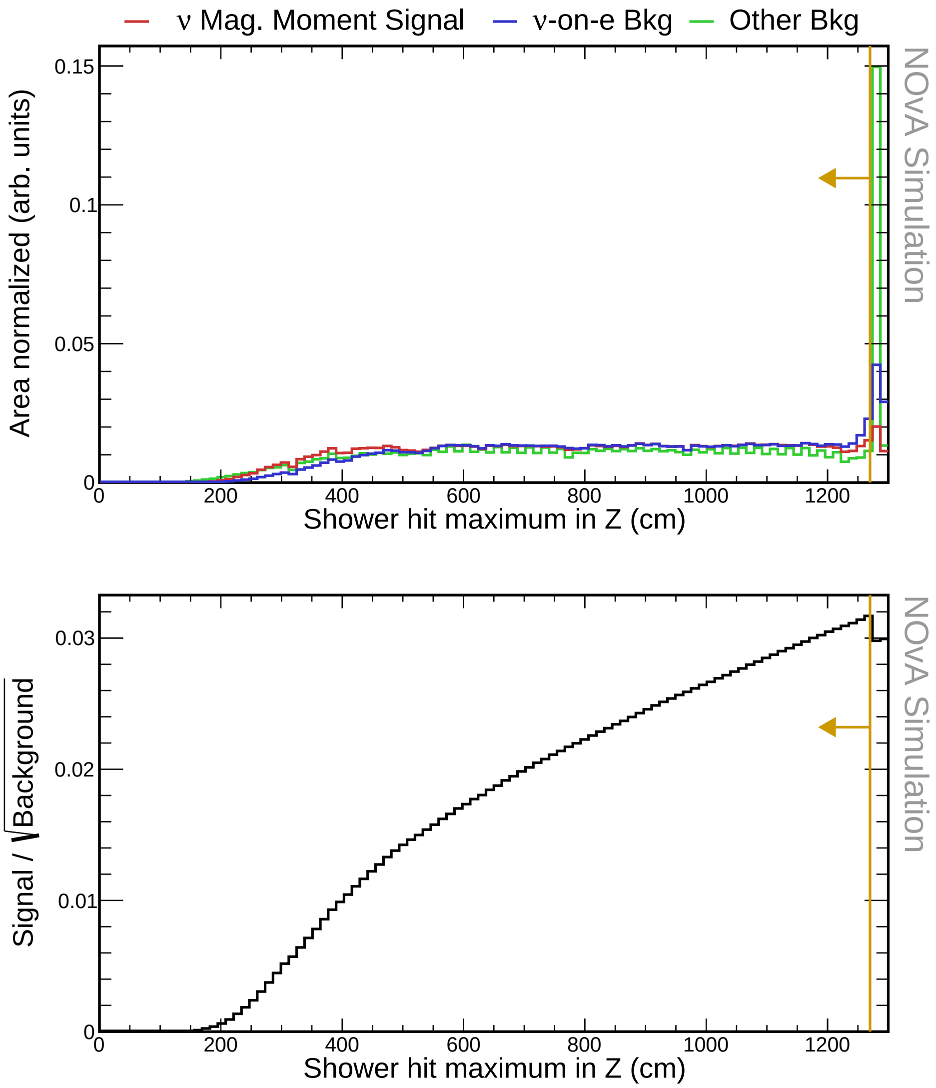

Figure 3.20: Relative comparison of signal, ν-on-e background, and other background events for the minimum and maximum position of the reconstructed shower along the z axis. Pre-selection and fiducial cuts were applied to make these plots. Gold lines show the values of the containment cuts.

Single Shower Requirement

To selection events with a single particle we require that the fraction of energy contained in the most energetic shower is > 0.8, that the summed energy of all cells (above threshold and within ± 8 planes from the vertex) outside of the most energetic shower is < 0.02 GeV, and that the distance between the vertex and the start of the primary shower is < 20 cm.

Event Classifiers

We are using two event classifiers based on convolution neural network that were developed specifically to identify ν-on-e interactions. The first one (`NuoneID`) is trained to select ν-on-e events and the second one (`Epi0ID`) is trained on the events passing the `NuoneID` to reject the π^0 background. Our selection requires that `NuoneID`$>$ 0.73 and that `Epi0ID`> 0.92.

TO DO: *reference theory for the kinematics of nuone scattering* We require that the product of reconstructed energy of the primary shower and the square of its angle from the Z axis is $E_{cal}\theta^2 < 0.005$ GeV $\times$ rad^2.

TO DO: *Add plots of distributions of the event selection variables with two columns. LHS shows no cuts applied and RHS shows all previous cuts applied*

Using the many plots below that show the effect of each of the cuts on the signal and all background events. (For signal we are showing NuMM=...)

[ND group's technote] Two event classifiers (NuoneID and Epi0ID) based on convolutional neural network (CNN) are trained to identify nuone elastic scattering events (NuoneID) and to further reject background with pi0 in the final state (Epi0ID). The CNN architecture adopted for this analysis is the one used for NOvA CVN [12]. It

Table 3.5: Event selection cutflow table for the reconstruction quality cuts showing the number of events and the relative efficiency of each cut for each signal sample. The relative efficiency is calculated as number of events remaining after applying the corresponding cut divided by number of event for all the previous cuts. All the cuts are listed in sequence as they are applied.

Selection	Signal		ν-on-e bkg		Other bkg	
	N_{evt}	ϵ_{rel} (%)	N_{evt}	ϵ_{rel} (%)	N_{evt}	ϵ_{rel} (%)
Basic selection	48.27	100	2.03×10^3	100	5.98×10^6	100
Fiducial	45.51	94.27	1.89×10^3	93.36	2.89×10^6	48.22
Containment	42.01	92.31	1.62×10^3	85.42	7.22×10^5	25.04

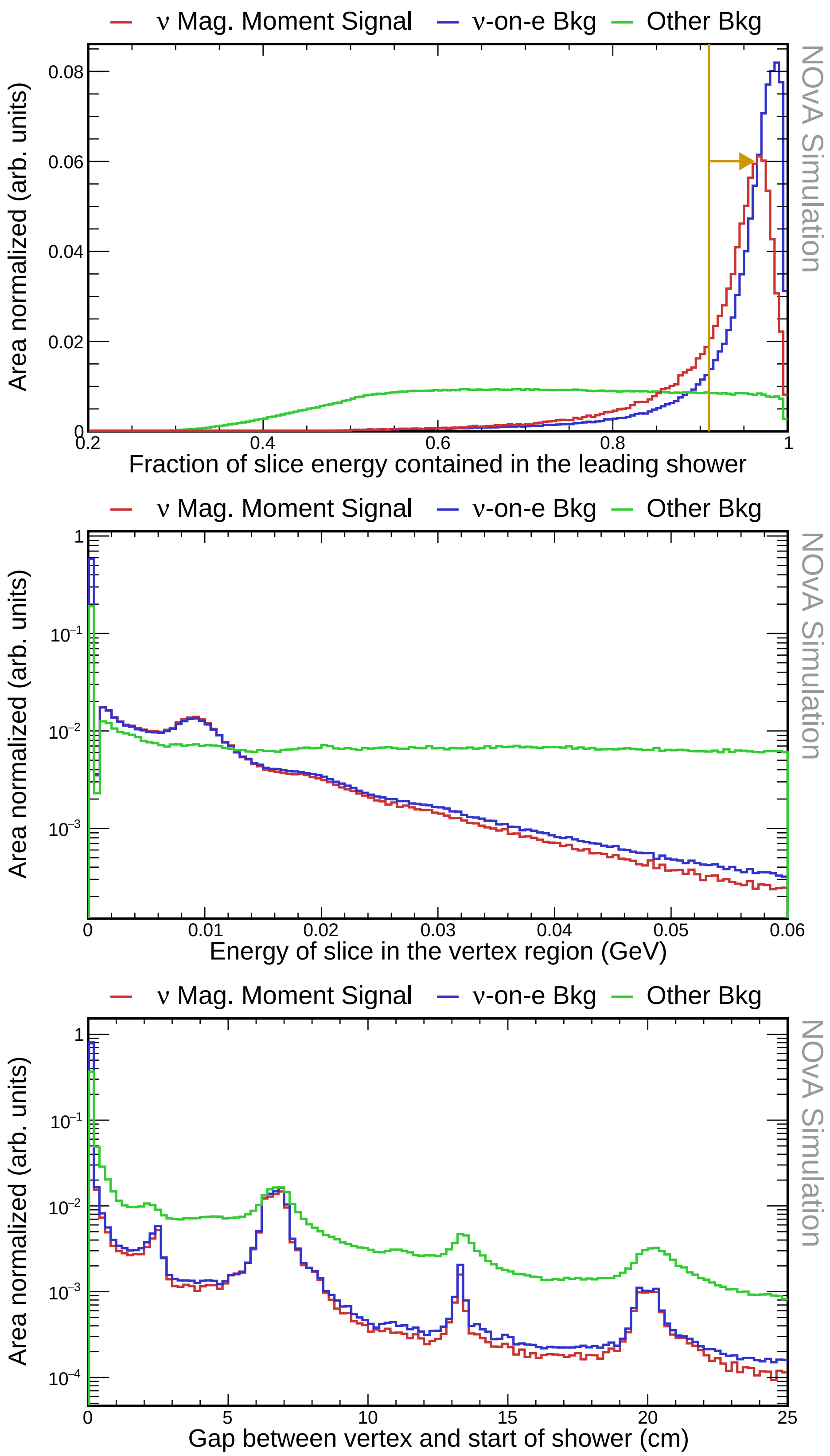

Figure 3.21: TMVA variables before the TMVA results. Relative comparison of signal, ν-on-e background, and other background events for the reconstructed vertex. Every previous cut was applied to make these plots, including the ShwECont for the middle and the bottom plot and the VtxE cut for the bottom plot. Gold lines show the cut values that create the fiducial volume.

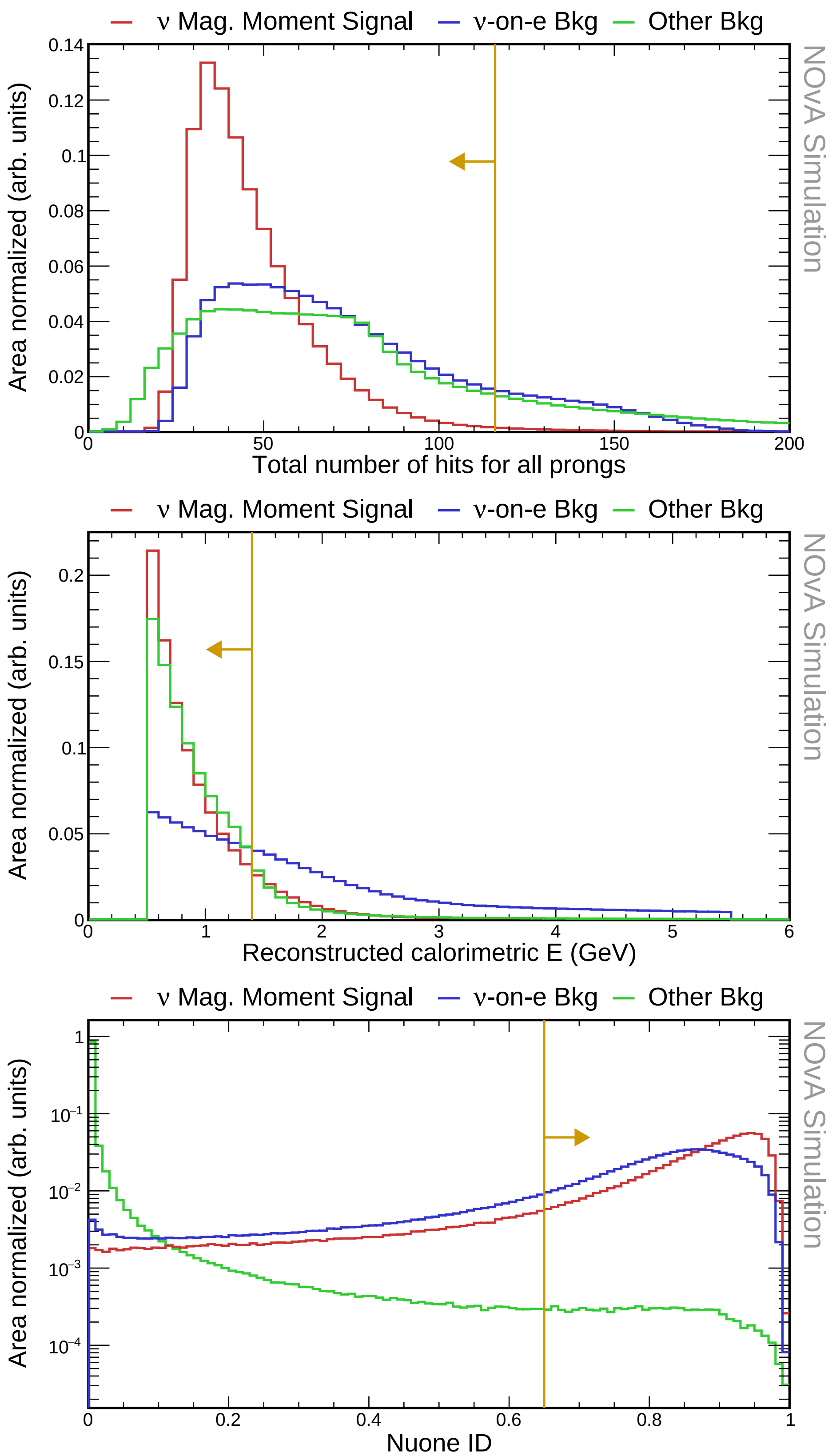

Figure 3.22: Relative comparison of signal, ν-on-e background, and other background events for the reconstructed vertex. No cuts were applied to make these plots. All the previous cuts were applied, including the cut on the shower energy. No single particle or event ID cuts were applied yet though. Gold lines show the cut values that create the fiducial volume.

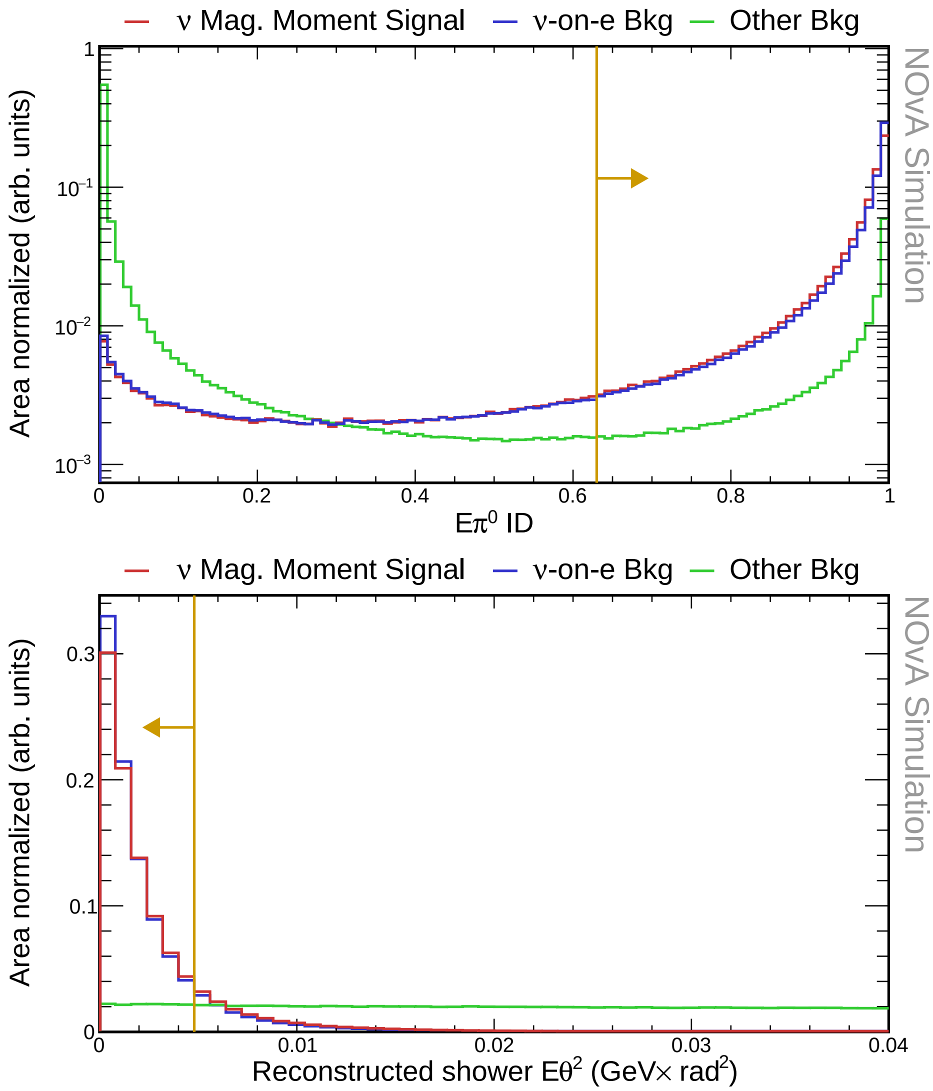

Figure 3.23: Relative comparison of signal, ν-on-e background, and other background events for the reconstructed vertex. No cuts were applied to make these plots. All the previous cuts were applied, including the cut on the shower energy. No single particle or event ID cuts were applied yet though. Gold lines show the cut values that create the fiducial volume.

takes the pixel map of a slice as the input and has deeper and more complicated neural networks than the ANNs used in the previous round of analysis [11]. The training for both classifiers (NuoneID and Epi0ID) were done with single electron samples as the signal in order to mitigate the model dependence. A nuone elastic scattering has an electron in the final state which could deposit energy in the detector. Single electron events share this feature with nuone elastic scattering, but have more uniform distribution of energy, angle between the shower direction and the beam direction. This additional feature could prevent CNN models from overfitting the feature of the very small scattering angle. To make comparisons, test samples of signal and background are normalized to 1.1E21. The output categories are ν-on-e, π^0, ν_eCC and other. The ν-on-e and π^0 outputs are used for the training of the Epi0ID. The pre-selection applied is: ND group's preselection ($L < 800\,\mathrm{cm}$, $N_{plane} < 120$, $N_{cell} < 600$), loose containment ($-190 < X < 190$, $-190 < Y < 190$, $50 < Z < 1500$ cm), loose single particle cut ($E_{vtx} < 0.05\,\mathrm{GeV}$, $gap < 20\,\mathrm{cm}$, $E_{shower}/E_{tot} > 0.9$ COMMENT: *These are quite strict actually*. The training accuracy for NuoneID is about 85% and for Epi0ID is about 96%. After each round of training, the trained model is saved to make predictions on the test sample so we know how the actual performance of the classifiers evolves over different epochs.

Multivariate Analysis

TMVA [166]

These event selection in total reduces signal $44.51\,\%$, ν-on-e background $70.40\,\%$ and other background $99.97\,\%$. After the full event selection, the predicted number of signal events for $\mu_\nu = 10^{-9}\mu_B$ is 23.31 and the total number of background events under the SM hypothesis is 678.26. The most likely improvement is in probing the low energetic events and making sure they make sense. Additionally, it is possible to use a specially designed control regions to mitigate the very high non-ν-on-e background.

TO DO: *Add a discussion of possible improvements on the event selection on its limitations - mostly for the analysis review committee* From here we can see that ... Maybe what can be improved is... This can likely be improved upon by specifically selection low energy events and removing the cut on the reconstructed shower energy.

3.4 Energy resolution and binning

TO DO: *Add the energy resolution and binning plots* Describe what events were used for the energy resolution study and how it was performed

What are the results

Final plot

The electron energy and angle distributions and resolutions. Are we going to fit in E, Th, or ETh2? Is there something else?

Show plots of Reco V True for both energy and angle. (Should I show it with or without the energy cut?). Also show the resolution plots.

Maybe also mention that Test Beam will help with improving the dead materials correction and generally improving the bias and resolution of the reconstructed energy, which won't have to depend on the comparison to simulation

3.5 Systematic uncertainties

3.6 Statistical analysis

We are basically doing two separate things:

1. Testing a hypothesis that there is no magnetic moment present in the signal. Can we reject the null hypothesis given our data?

Table 3.6: Event selection cutflow table for the reconstruction quality cuts showing the number of events and the relative efficiency of each cut for each signal sample. The relative efficiency is calculated as number of events remaining after applying the corresponding cut divided by number of event for all the previous cuts. All the cuts are listed in sequence as they are applied.

Selection	Signal		ν-on-e bkg		Other bkg	
	N_{evt}	ϵ_{rel} (%)	N_{evt}	ϵ_{rel} (%)	N_{evt}	ϵ_{rel} (%)
Pre-selection	42.01	100	1.62×10^3	100	7.22×10^5	100
E_{Shower}/E_{Tot}	40.32	95.98	1.57×10^3	96.87	2.79×10^5	38.60
N^o Hits	39.93	99.03	1.34×10^3	85.56	2.63×10^5	94.24
High E_{Shower}	34.70	86.91	714.28	53.28	2.22×10^5	84.58
ν-on-e ID	29.41	84.75	600.38	84.05	3.36×10^3	1.51
$E\pi^0$ **ID**	27.46	93.37	560.56	93.37	2.18×10^3	64.72
$E\theta^2$	23.31	84.88	478.83	85.42	199.42	9.17

2. If we can reject the null hypothesis we want to estimate the best fit of the parameter. Additionally, we want to put a limit (set a confidence interval) on the magnetic moment parameter.

What should be included here:

- Fit methodology: Detail the fitting techniques used to extract the muon neutrino magnetic moment from the data.
- Fit validation: Describe how the fit is validated, including any statistical tests used.
- Fake data studies: Explain the use of fake data or Monte Carlo simulations to test the robustness of the analysis.

3.7 Results

Show the money plot - full prediction in the binned energy distribution, including the full statistical and systematic uncertainties

Write out the total number of measured events and their corresponding uncertainties

Explain what are the results of the fit and the limits, discuss the statistical significance of the result

3.8 Discussion

What should be included here:

- Interpretation: Interpret the results in the context of the current understanding of neutrino physics.
- Implications: Explain the broader implications of your findings for the field of particle physics.
- Future work: Suggest directions for future research based on your results.

  - Improvements in NOvA, more FHC data, including RHC data, better reconstruction, better simulation and calibration, better event selection, including sideband samples, more systematics studies, better fitting techniques...
  - Future beyond NOvA - DUNE
    * What are the possibilities for DUNE?

3.9 Conclusion

Summarize the results and compare them to the introduction, including comparisons to other experiments and theory. Restate the significant of the measurement

Closing remarks

Acronyms

ν**-on-e** neutrino-on-electron. 37, 38, 40, 41, 44–55, 57–63, 65–68, 78, 79

2p2h two particle - two hole. 5, 6, 21

ADC Analog-to-Digital Converter. 19, 26, 29

APD Avalanche Photodiode. 16, 18, 19, 22, 29, 30, 56

ASIC Application-Specific Integrated Circuit. 19

BDT Boosted Decision Tree. 26

BPF Break Point Fitter. 24

BSM Beyond Standard Model. 10–12, 37–39, 41, 42

C.L. Confidence Level. 37, 38

CC Charged Current. 1, 2, 4–6, 8, 9, 21–23, 46, 52, 53, 60, 78

CEvNS Coherent Elastic ν-Nucleus Scattering. 6

CMC Comprehensive Model Configuration. 22

CNN Convolutional Neural Network. 25

COHπ Coherent π (production). 6, 21, 22

CP Charge conjugation - Parity (symmetry). 1, 8, 10, 13

CRY Cosmic-Ray Shower Generator. 22, 26

CVN Convolutional Visual Network. 25, 55

DAQ Data Acquisition. 19, 23, 28

DCM Data Concentration Module. 19, 54

DIS Deep Inelastic Scattering. 5, 21, 22

DUNE Deep Underground Neutrino Experiment. 10, 13, 21

FB Fibre Brightness. 29, 30

FD Far Detector. 15–19, 22, 23, 28–31, 34

FEB Front End Board. 18–20, 29, 56

Fermilab Fermi National Accelerator Laboratory. 13, 16, 21

FHC Forward Horn Current (neutrino mode). 14, 15

FOM Figure Of Merit. 53, 54, 65–67

FPGA Field Programmable Gate Array. 19

FSI Final State Interaction. 6, 21, 22

HK Hyper-Kamiokande. 10

HNL Heavy Neutral Lepton. 12

LBL Long Baseline. 10

LDM Light Dark Matter. 38

LOWESS Locally Weighted Scatter plot Smoothing. 31, 32

MC Monte Carlo. 20–22, 26, 51

MEC Meson Exchange Current. 6, 21, 22, 52, 53

MEU Muon Energy Unit. 33

MI Main Injector. 13, 14, 20

MIP Minimum Ionising Particle. 26, 30, 32

MIPP Main Injector Particle Production (experiment). 21

ML Machine Learning. 24–26, 56

MSW Mikheyev-Smirnov-Wolfenstein. 9

NC Neutral Current. 1–4, 6, 8, 9, 23, 25

ND Near Detector. 13–17, 19, 22–24, 34, 36–38, 41, 43, 50, 53, 60

NDOS Near Detector on the Surface. 16

NOvA NuMI Off-axis ν_e Appearance (experiment). 10, 13–26, 28–34, 36–38, 40, 41, 43, 45, 47–50, 52, 53, 55, 56

NP New Physics. 11, 42

NuMI Neutrinos from the Main Injector. 13–16, 20, 21, 23

PE Photo Electron. 18, 19, 27, 29–31

PECorr Corrected Photo Electrons. 31, 33

PID Particle Identification. 25

PMNS Pontecorvo-Maki-Nakagawa-Sakata. 7, 8, 41, 42

POT Protons On Target. 14, 50, 52, 54, 59

PPFX Package to Predict the Flux. 21, 35, 50

PVC Polyvinyl chloride. 16–18, 34

QE Quasi Elastic (interaction). 4–6, 21, 22

ReMId Reconstructed Muon Identifier. 26

Res Resonant baryon production. 5, 21, 22

RHC Reverse Horn Current (antineutrino mode). 14, 15

SK Super-Kamiokande. 9

SM Standard Model. 1, 2, 10–12, 37, 39–42, 46–50, 54, 78

SNO Sudbury Neutrino Observatory. 9

T2K Tokai to Kamioka (experiment). 10

WLS Wavelength Shifting (fibre). 16–18, 22, 26, 28, 30, 33

Bibliography

[1] Wolfgang Pauli. Pauli letter collection: letter to Lise Meitner. Typed copy. URL http://cds.cern.ch/record/83282.

[2] L. M. Brown. The idea of the neutrino. *Physics Today*, 31(9):23–28, September 1978. doi:10.1063/1.2995181. (Including translation of W. Pauli, Aufsdtze und Vortrdge u'ber Physik und Erkenntnistheorie, Braunschweig (1961)).

[3] H. A. Bethe. Ionization power of a neutrino with magnetic moment. *Mathematical Proceedings of the Cambridge Philosophical Society*, 31(1):108–115, 1935. doi:10.1017/S0305004100012998.

[4] Enrico Fermi. Tentativo di una teoria dei raggi β. *Il Nuovo Cimento (1924-1942)*, 11(1):1–19. ISSN 1827-6121. doi:10.1007/BF02959820.

[5] Fred L. Wilson. Fermi's theory of beta decay. *American Journal of Physics*, 36 (12):1150–1160, 1968. doi:10.1119/1.1974382. (A complete English translation of E.Fermi, Zeitschrift fur Physik 88, 161 (1934)).

[6] Sheldon L. Glashow. Partial-symmetries of weak interactions. *Nuclear Physics*, 22(4):579–588. ISSN 0029-5582. doi:10.1016/0029-5582(61)90469-2. URL https://www.sciencedirect.com/science/article/pii/0029558261904692.

[7] Steven Weinberg. A model of leptons. *Phys. Rev. Lett.*, 19:1264–1266, Nov 1967. doi:10.1103/PhysRevLett.19.1264.

[8] Abdus Salam. *Weak and electromagnetic interactions*, pages 244–254. doi:10.1142/9789812795915_0034.

[9] L. Landau. On the conservation laws for weak interactions. *Nuclear Physics*, 3(1):127–131. ISSN 0029-5582. doi:10.1016/0029-5582(57)90061-5. URL https://www.sciencedirect.com/science/article/pii/0029558257900615.

[10] T. D. Lee and C. N. Yang. Parity nonconservation and a two-component theory of the neutrino. *Phys. Rev.*, 105:1671–1675, Mar 1957. doi:10.1103/PhysRev.105.1671.

[11] Abdus Salam. On parity conservation and neutrino mass. *Nuovo Cim.*, 5:299–301, 1957. doi:10.1007/BF02812841.

[12] Peter W. Higgs. Broken symmetries and the masses of gauge bosons. *Phys. Rev. Lett.*, 13:508–509, Oct 1964. doi:10.1103/PhysRevLett.13.508.

[13] F. Englert and R. Brout. Broken symmetry and the mass of gauge vector mesons. *Phys. Rev. Lett.*, 13:321–323, Aug 1964. doi:10.1103/PhysRevLett.13.321.

[14] G. S. Guralnik, C. R. Hagen, and T. W. B. Kibble. Global conservation laws and massless particles. *Phys. Rev. Lett.*, 13:585–587, Nov 1964. doi:10.1103/PhysRevLett.13.585.

[15] Steven Weinberg. A model of leptons. *Phys. Rev. Lett.*, 19:1264–1266, Nov 1967. doi:10.1103/PhysRevLett.19.1264.

[16] Carlo Giunti and Chung W. Kim. *Fundamentals of Neutrino Physics and Astrophysics*. 2007. ISBN 978-0-19-850871-7.

[17] F. Reines and C. L. Cowan. Detection of the free neutrino. *Phys. Rev.*, 92:830–831, Nov 1953. doi:10.1103/PhysRev.92.830.

[18] Cowan Jr. C.L., Reines F., Harrison F.B., Kruse H.W., and McGuire A.D. Detection of the free neutrino: A confirmation. *Science*, 124(3212):103–104, July 1956. doi:10.1126/science.124.3212.103.

[19] F. Reines and C.L. Cowan. Neutrino physics. *Physics Today*, 10(8):12–18, 1957. doi:10.1063/1.3060455.

[20] B. Adeva et al. Measurement of Z^0 decays to hadrons and a precise determination of the number of neutrino species. *Phys. Lett. B*, 237:136–146, 1990. doi:10.1016/0370-2693(90)90476-M.

[21] S. Schael et al. Precision electroweak measurements on the Z resonance. *Phys. Rept.*, 427:257–454, 2006. doi:10.1016/j.physrep.2005.12.006.

[22] M. C. Goodman. Resource letter anp-1: Advances in neutrino physics. *American Journal of Physics*, 84:309–319, 2016. doi:10.1119/1.4962228.

[23] M. Schwartz. Feasibility of using high-energy neutrinos to study the weak interactions. *Phys. Rev. Lett.*, 4:306–307, Mar 1960. doi:10.1103/PhysRevLett.4.306.

[24] K. Kodama et al. Observation of tau neutrino interactions. *Phys. Lett. B*, 504: 218–224, 2001. doi:10.1016/S0370-2693(01)00307-0.

[25] K. Kodama et al. Final tau-neutrino results from the DONuT experiment. *Phys. Rev. D*, 78:052002, 2008. doi:10.1103/PhysRevD.78.052002.

[26] William J Marciano and Zohreh Parsa. Neutrino–electron scattering theory*. *Journal of Physics G: Nuclear and Particle Physics*, 29(11):2629. doi:10.1088/0954-3899/29/11/013.

[27] J. A. Formaggio and G. P. Zeller. From ev to eev: Neutrino cross sections across energy scales. *Rev. Mod. Phys.*, 84:1307–1341, Sep 2012. doi:10.1103/RevModPhys.84.1307.

[28] *Fundamental Physics at the Intensity Frontier*, 5 2012. doi:10.2172/1042577.

[29] D. Casper. The Nuance neutrino physics simulation, and the future. *Nucl. Phys. B Proc. Suppl.*, 112:161–170, 2002. doi:10.1016/S0920-5632(02)01756-5.

[30] Jr. Davis, Raymond, Don S. Harmer, and Kenneth C. Hoffman. Search for neutrinos from the sun. *Phys. Rev. Lett.*, 20:1205–1209, 1968. doi:10.1103/PhysRevLett.20.1205.

[31] G. Danby, J-M. Gaillard, K. Goulianos, L. M. Lederman, N. Mistry, M. Schwartz, and J. Steinberger. Observation of high-energy neutrino reactions and the existence of two kinds of neutrinos. *Phys. Rev. Lett.*, 9:36–44, Jul 1962. doi:10.1103/PhysRevLett.9.36.

[32] A. A. Aguilar-Arevalo et al. First measurement of the muon neutrino charged current quasielastic double differential cross section. *Phys. Rev. D*, 81:092005, May 2010. doi:10.1103/PhysRevD.81.092005.

[33] M. Sajjad Athar, A. Fatima, and S. K. Singh. Neutrinos and their interactions with matter. *Prog. Part. Nucl. Phys.*, 129:104019, 2023. doi:10.1016/j.ppnp.2022.104019.

[34] M. Martini, M. Ericson, G. Chanfray, and J. Marteau. Unified approach for nucleon knock-out and coherent and incoherent pion production in neutrino interactions with nuclei. *Phys. Rev. C*, 80:065501, Dec 2009. doi:10.1103/PhysRevC.80.065501.

[35] M. Martini, M. Ericson, G. Chanfray, and J. Marteau. Neutrino and antineutrino quasielastic interactions with nuclei. *Phys. Rev. C*, 81:045502, Apr 2010. doi:10.1103/PhysRevC.81.045502.

[36] M. Martini, M. Ericson, and G. Chanfray. Neutrino quasielastic interaction and nuclear dynamics. *Phys. Rev. C*, 84:055502, Nov 2011. doi:10.1103/PhysRevC.84.055502.

[37] D. Akimov et al. Observation of coherent elastic neutrino-nucleus scattering. *Science*, 357(6356):1123–1126. doi:10.1126/science.aao0990.

[38] B Pontecorvo. Mesonium and antimesonium. *Sov. Phys. JETP*, 33:549–551, 8 1957.

[39] B. Pontecorvo. Inverse beta processes and nonconservation of lepton charge. *Sov. Phys. JETP*, 7:172–173, 1958.

[40] Ziro Maki, Masami Nakagawa, and Shoichi Sakata. Remarks on the unified model of elementary particles. *Prog. Theor. Phys.*, 28:870–880, 1962. doi:10.1143/PTP.28.870.

[41] V. Gribov and B. Pontecorvo. Neutrino astronomy and lepton charge. *Physics Letters B*, 28(7):493–496. ISSN 0370-2693. doi:10.1016/0370-2693(69)90525-5. URL https://www.sciencedirect.com/science/article/pii/0370269369905255.

[42] M.C. Gonzalez-Garcia and Yosef Nir. Neutrino Masses and Mixing: Evidence and Implications. *Rev. Mod. Phys.*, 75:345–402, 2003. doi:10.1103/RevModPhys.75.345.

[43] L. Wolfenstein. Neutrino oscillations in matter. *Phys. Rev. D*, 17:2369–2374, May 1978. doi:10.1103/PhysRevD.17.2369.

[44] S.P. Mikheyev and A.Yu. Smirnov. Resonance Amplification of Oscillations in Matter and Spectroscopy of Solar Neutrinos. *Sov. J. Nucl. Phys.*, 42:913–917, 1985.

[45] M. Aglietta et al. Experimental study of atmospheric neutrino flux in the NUSEX experiment. *Europhysics Letters (EPL)*, 8(7):611–614, 04 1989. doi:10.1209/0295-5075/8/7/005.

[46] K. Daum et al. Determination of the atmospheric neutrino spectra with the Fréjus detector. *Zeitschrift für Physik C Particles and Fields*, 66(3):417–428, 1995. ISSN 1431-5858. doi:10.1007/BF01556368.

[47] R. Becker-Szendy et al. Electron- and muon-neutrino content of the atmospheric flux. *Phys. Rev. D*, 46:3720–3724, Nov 1992. doi:10.1103/PhysRevD.46.3720.

[48] Y. Fukuda et al. Atmospheric muon-neutrino / electron-neutrino ratio in the multiGeV energy range. *Phys. Lett. B*, 335:237–245, 1994. doi:10.1016/0370-2693(94)91420-6.

[49] Y. Fukuda et al. Evidence for oscillation of atmospheric neutrinos. *Phys. Rev. Lett.*, 81:1562–1567, 1998. doi:10.1103/PhysRevLett.81.1562.

[50] Q.R. Ahmad et al. Direct evidence for neutrino flavor transformation from neutral current interactions in the Sudbury Neutrino Observatory. *Phys. Rev. Lett.*, 89:011301, 2002. doi:10.1103/PhysRevLett.89.011301.

[51] Patrick Huber et al. Snowmass Neutrino Frontier Report. In *Snowmass 2021*, 11 2022.

[52] R. L. Workman and Others. Review of Particle Physics. *PTEP*, 2022:083C01, 2022. doi:10.1093/ptep/ptac097.

[53] Ivan Esteban, M. C. Gonzalez-Garcia, Michele Maltoni, Thomas Schwetz, and Albert Zhou. The fate of hints: updated global analysis of three-flavor neutrino oscillations. *JHEP*, 09:178, 2020. doi:10.1007/JHEP09(2020)178.

[54] M. A. Acero et al. Improved measurement of neutrino oscillation parameters by the NOvA experiment. *Phys. Rev. D*, 106(3):032004, 2022. doi:10.1103/PhysRevD.106.032004.

[55] K. Abe et al. Measurements of neutrino oscillation parameters from the T2K experiment using 3.6×10^{21} protons on target. *Eur. Phys. J. C*, 83(9):782, 2023. doi:10.1140/epjc/s10052-023-11819-x.

[56] B. Abi et al. Volume I. Introduction to DUNE. *Journal of Instrumentation*, 15 (08):T08008. doi:10.1088/1748-0221/15/08/T08008.

[57] K. Abe et al. Hyper-Kamiokande Design Report. 5 2018.

[58] M. Aker et al. Direct neutrino-mass measurement with sub-electronvolt sensitivity. *Nature Phys.*, 18(2):160–166, 2022. doi:10.1038/s41567-021-01463-1.

[59] Aghanim, N. et al. Planck 2018 results - vi. cosmological parameters. *Astron. Astrophys.*, 641:A6. doi:10.1051/0004-6361/201833910.

[60] A. Aguilar et al. Evidence for neutrino oscillations from the observation of $\overline{\nu}_e$ appearance in a $\overline{\nu}_\mu$ beam. *Phys. Rev. D*, 64:112007, Nov 2001. doi:10.1103/PhysRevD.64.112007.

[61] A.A. Aguilar-Arevalo et al. Significant Excess of ElectronLike Events in the MiniBooNE Short-Baseline Neutrino Experiment. *Phys. Rev. Lett.*, 121(22): 221801, 2018. doi:10.1103/PhysRevLett.121.221801.

[62] M.C. Gonzalez-Garcia and Michele Maltoni. Phenomenology with Massive Neutrinos. *Phys. Rept.*, 460:1–129, 2008. doi:10.1016/j.physrep.2007.12.004.

[63] Rabindra N. Mohapatra and Goran Senjanovic. Neutrino Mass and Spontaneous Parity Nonconservation. *Phys. Rev. Lett.*, 44:912, 1980. doi:10.1103/PhysRevLett.44.912.

[64] Ettore Majorana. Teoria simmetrica dell'elettrone e del positrone. *Nuovo Cim.*, 14:171–184, 1937. doi:10.1007/BF02961314. Translated by Luciano Maiani in"Soryushiron Kenkyu", 63 (1981) 149-462.

[65] Nova experiments official website. URL https://novaexperiment.fnal.gov. Cited February 2024.

[66] Fermi national accelerator laboratory official website. URL https://fnal.gov. Cited February 2024.

[67] Gary Feldman for the NOvA Collaboration. Physics of the nova experiment. White paper, 2012. URL https://nova-docdb.fnal.gov/cgi-bin/ShowDocument?docid=7733. Public NOvA document: NOVA-doc-7733-v1, cited on 05.2020.

[68] R.B. Patterson. The NOvA Experiment: Status and Outlook. *Nucl. Phys. B Proc. Suppl.*, 235-236:151–157, 2013. doi:10.1016/j.nuclphysbps.2013.04.005.

[69] P. Adamson et al. First measurement of muon-neutrino disappearance in NOvA. *Phys. Rev. D*, 93(5):051104, 2016. doi:10.1103/PhysRevD.93.051104.

[70] M.A. Acero et al. First Measurement of Neutrino Oscillation Parameters using Neutrinos and Antineutrinos by NOvA. *Phys. Rev. Lett.*, 123(15):151803, 2019. doi:10.1103/PhysRevLett.123.151803.

[71] M. A. Acero et al. Measurement of neutrino-induced neutral-current coherent π^0 production in the NOvA near detector. *Phys. Rev. D*, 102(1):012004, 2020. doi:10.1103/PhysRevD.102.012004.

[72] M. A. Acero et al. Measurement of the double-differential muon-neutrino charged-current inclusive cross section in the NOvA near detector. *Phys. Rev. D*, 107(5):052011, 2023. doi:10.1103/PhysRevD.107.052011.

[73] M. A. Acero et al. Measurement of the ν_e−Nucleus Charged-Current Double-Differential Cross Section at $\langle E_\nu \rangle = 2.4$ GeV using NOvA. *Phys. Rev. Lett.*, 130 (5):051802, 2023. doi:10.1103/PhysRevLett.130.051802.

[74] M. A. Acero et al. Measurement of ν_μ charged-current inclusive π^0 production in the NOvA near detector. *Phys. Rev. D*, 107(11):112008, 2023. doi:10.1103/PhysRevD.107.112008.

[75] P. Adamson et al. Search for active-sterile neutrino mixing using neutral-current interactions in NOvA. *Phys. Rev. D*, 96(7):072006, 2017. doi:10.1103/PhysRevD.96.072006.

[76] M. A. Acero et al. Search for Active-Sterile Antineutrino Mixing Using Neutral-Current Interactions with the NOvA Experiment. *Phys. Rev. Lett.*, 127(20): 201801, 2021. doi:10.1103/PhysRevLett.127.201801.

[77] M. A. Acero et al. Supernova neutrino detection in NOvA. *JCAP*, 10:014, 2020. doi:10.1088/1475-7516/2020/10/014.

[78] M. A. Acero et al. Extended search for supernovalike neutrinos in NOvA coincident with LIGO/Virgo detections. *Phys. Rev. D*, 104(6):063024, 2021. doi:10.1103/PhysRevD.104.063024.

[79] M. A. Acero et al. Search for slow magnetic monopoles with the NOvA detector on the surface. *Phys. Rev. D*, 103(1):012007, 2021. doi:10.1103/PhysRevD.103.012007.

[80] Peter N. Shanahan and Patricia LaVern Vahle. Physics with NOvA: a half-time review. *Eur. Phys. J. ST*, 230(24):4259–4273, 2021. doi:10.1140/epjs/s11734-021-00285-9.

[81] Peter Shanahan and Patricia Vahle. The NOvA Physics Program through 2025. Snowmass 2021 Letters of Interest NF, 135. URL https://www.snowmass21.org/docs/files/summaries/NF/SNOWMASS21-NF1_NF3_Patricia_Vahle-145.pdf.

[82] P. Adamson et al. The NuMI Neutrino Beam. *Nucl. Instrum. Meth. A*, 806:279–306, 2016. doi:10.1016/j.nima.2015.08.063.

[83] Records. URL https://operations.fnal.gov/records/. Performance records achieved by the Fermilab accelerators. Cited May 2024.

[84] Katsuya Yonehara. Megawatt upgrade of numi target system. 1 2022. URL https://www.osti.gov/biblio/1844332.

[85] Leonidas Aliaga Soplin. *Neutrino Flux Prediction for the NuMI Beamline.* PhD thesis, William-Mary Coll., 2016.

[86] Leonidas Aliaga Soplin. 2017-2018 Beam Plots. NOVA Document 20843. URL https://nova-docdb.fnal.gov/cgi-bin/sso/ShowDocument?docid=20843. NOvA internal document.

[87] D. S. Ayres et al. The nova technical design report. *NOvA Collaboration*, 2007. doi:10.2172/935497.

[88] Yury Kudenko. Neutrino detectors for oscillation experiments. *JINST*, 12(06): C06003, 2017. doi:10.1088/1748-0221/12/06/C06003.

[89] S. Mufson et al. Liquid scintillator production for the NOvA experiment. *Nucl. Instrum. Meth. A*, 799:1–9, 2015. doi:10.1016/j.nima.2015.07.026.

[90] Alex Sousa. Density of NOvA Liquid Scintillator at 69° F. NOVA Document 11886. URL https://nova-docdb.fnal.gov/cgi-bin/sso/ShowDocument?docid=11886. NOvA internal document.

[91] M.J. Berger, J.S. Coursey, M.A. Zucker, and J. Chang. ESTAR, PSTAR, and ASTAR: Computer Programs for Calculating Stopping-Power and Range Tables for Electrons, Protons, and Helium Ions (version 1.2.3). URL http://physics.nist.gov/Star.

[92] Luke Vinton. Calorimetric Energy Scale Calibration of the NOvA Detectors. NOVA Document 13579, document FA_Calorimetric_energy_scale.pdf. URL https://nova-docdb.fnal.gov/cgi-bin/sso/ShowDocument?docid=13579. NOvA Technical Note.

[93] Xinchun Tian. NOvA Data Acquisition Software System. In *Meeting of the APS Division of Particles and Fields*, 9 2011.

[94] Joao Coelho, Barnali Chowdhury, and Ryan Murphy. Tech note: Good data selection. NOVA Document 13546. URL https://nova-docdb.fnal.gov/cgi-bin/sso/ShowDocument?docid=13546. NOvA technical note.

[95] Jonathan M. Paley. BadChannels Technical Note. NOVA Document 12771. URL https://nova-docdb.fnal.gov/cgi-bin/sso/ShowDocument?docid=12771. NOvA technical note.

[96] A. Aurisano, C. Backhouse, R. Hatcher, N. Mayer, J. Musser, R. Patterson, R. Schroeter, and A. Sousa. The NOvA simulation chain. *J. Phys. Conf. Ser.*, 664(7):072002, 2015. doi:10.1088/1742-6596/664/7/072002.

[97] S. Agostinelli et al. GEANT4–a simulation toolkit. *Nucl. Instrum. Meth. A*, 506: 250–303, 2003. doi:10.1016/S0168-9002(03)01368-8.

[98] Zarko Pavlovic. *Observation of Disappearance of Muon Neutrinos in the NuMI Beam.* PhD thesis, Texas U., 2008.

[99] L. Aliaga et al. Neutrino Flux Predictions for the NuMI Beam. *Phys. Rev. D*, 94(9):092005, 2016. doi:10.1103/PhysRevD.94.092005. [Addendum: Phys.Rev.D 95, 039903 (2017)].

[100] C. Alt et al. Inclusive production of charged pions in p+C collisions at 158-GeV/c beam momentum. *Eur. Phys. J. C*, 49:897–917, 2007. doi:10.1140/epjc/s10052-006-0165-7.

[101] Gemma Maria Tinti. *Sterile neutrino oscillations in MINOS and hadron production in pC collisions.* PhD thesis, 2010.

[102] B Baatar, G Barr, J Bartke, L Betev, O Chvala, J Dolejsi, V Eckardt, HG Fischer, Z Fodor, A Karev, et al. Inclusive production of protons, anti-protons, neutrons, deuterons and tritons in p+ c collisions at 158 gev/c beam momentum. *The European Physical Journal C*, 73:1–66, 2013. doi:10.1140/epjc/s10052-013-2364-3.

[103] D. S. Barton et al. Experimental study of the a dependence of inclusive hadron fragmentation. *Phys. Rev. D*, 27:2580–2599, Jun 1983. doi:10.1103/PhysRevD.27.2580.

[104] Andrey V. Lebedev. *Ratio of Pion Kaon Production in Proton Carbon Interactions.* PhD thesis, 2007.

[105] T.T. Böhlen, F. Cerutti, M.P.W. Chin, A. Fassò, A. Ferrari, P.G. Ortega, A. Mairani, P.R. Sala, G. Smirnov, and V. Vlachoudis. The fluka code: Developments and challenges for high energy and medical applications. *Nuclear Data Sheets*, 120:211–214. ISSN 0090-3752. doi:10.1016/j.nds.2014.07.049.

[106] Alfredo Ferrari, Paola R. Sala, Alberto Fasso, and Johannes Ranft. FLUKA: A multi-particle transport code (Program version 2005). 10 2005. doi:10.2172/877507.

[107] A. Aduszkiewicz et al. Measurements of production and inelastic cross sections for p+C , p+Be , and p+Al at 60 GeV/c and p+C and p+Be at 120 GeV/c. *Phys. Rev. D*, 100(11):112001, 2019. doi:10.1103/PhysRevD.100.112001.

[108] H. Adhikary et al. Measurements of π^+, π^-, p, $\bar{p}$, K^+ and K^- production in 120 GeV/c p + C interactions. *Phys. Rev. D*, 108:072013, 2023. doi:10.1103/PhysRevD.108.072013.

[109] H. Adhikary et al. Measurements of KS0, Λ, and Λ^- production in 120 GeV/c p+C interactions. *Phys. Rev. D*, 107(7):072004, 2023. doi:10.1103/PhysRevD.107.072004.

[110] A. Aduszkiewicz et al. Measurements of hadron production in π^+ + C and π^+ + Be interactions at 60 GeV/c. *Phys. Rev. D*, 100(11):112004, 2019. doi:10.1103/PhysRevD.100.112004.

[111] Matej Pavin. Hadron production measurements for neutrino experiments, 2020. URL https://indico.fnal.gov/event/43209/contributions/187869/attachments/130502/159028/HadronProduction_neutrino2020.pdf. Presented on Neutrino 2020 conference.

[112] T. Akaishi et al. EMPHATIC: A Proposed Experiment to Measure Hadron Scattering and Production Cross Sections for Improved Neutrino Flux Predictions. 12 2019.

[113] C. Andreopoulos et al. The GENIE Neutrino Monte Carlo Generator. *Nucl. Instrum. Meth. A*, 614:87–104, 2010. doi:10.1016/j.nima.2009.12.009.

[114] J. Nieves, J. E. Amaro, and M. Valverde. Inclusive quasielastic charged-current neutrino-nucleus reactions. *Phys. Rev. C*, 70:055503, Nov 2004. doi:10.1103/PhysRevC.70.055503.

[115] Aaron S. Meyer, Minerba Betancourt, Richard Gran, and Richard J. Hill. Deuterium target data for precision neutrino-nucleus cross sections. *Phys. Rev. D*, 93:113015, Jun 2016. doi:10.1103/PhysRevD.93.113015.

[116] J. Nieves, I. Ruiz Simo, and M. J. Vicente Vacas. Inclusive charged-current neutrino-nucleus reactions. *Phys. Rev. C*, 83:045501, Apr 2011. doi:10.1103/PhysRevC.83.045501.

[117] R. Gran, J. Nieves, F. Sanchez, and M. J. Vicente Vacas. Neutrino-nucleus quasi-elastic and 2p2h interactions up to 10 gev. *Phys. Rev. D*, 88:113007, Dec 2013. doi:10.1103/PhysRevD.88.113007.

[118] Ch. Berger and L. M. Sehgal. Lepton mass effects in single pion production by neutrinos. *Phys. Rev. D*, 76:113004, Dec 2007. doi:10.1103/PhysRevD.76.113004.

[119] Ch. Berger and L. M. Sehgal. Partially conserved axial vector current and coherent pion production by low energy neutrinos. *Phys. Rev. D*, 79:053003, Mar 2009. doi:10.1103/PhysRevD.79.053003.

[120] A Bodek and U. K. Yang. Higher twist, xi(omega) scaling, and effective LO PDFs for lepton scattering in the few GeV region. *J. Phys. G*, 29:1899–1906, 2003. doi:10.1088/0954-3899/29/8/369.

[121] T. Yang, C. Andreopoulos, H. Gallagher, K. Hoffmann, and P. Kehayias. A Hadronization Model for Few-GeV Neutrino Interactions. *Eur. Phys. J. C*, 63:1–10, 2009. doi:10.1140/epjc/s10052-009-1094-z.

[122] L.L. Salcedo, E. Oset, M.J. Vicente-Vacas, and C. Garcia-Recio. Computer simulation of inclusive pion nuclear reactions. *Nuclear Physics A*, 484(3):557–592. ISSN 0375-9474. doi:10.1016/0375-9474(88)90310-7.

[123] Chris Hagmann, David Lange, and Douglas Wright. Cosmic-ray shower generator (cry) for monte carlo transport codes. volume 2, pages 1143 – 1146. ISBN 978-1-4244-0922-8. doi:10.1109/NSSMIC.2007.4437209.

[124] C. N. Chou. The nature of the saturation effect of fluorescent scintillators. *Phys. Rev.*, 87:904–905, Sep 1952. doi:10.1103/PhysRev.87.904.

[125] M. Baird, J. Bian, M. Messier, E. Niner, D. Rocco, and K. Sachdev. Event Reconstruction Techniques in NOvA. *J. Phys. Conf. Ser.*, 664(7):072035, 2015. doi:10.1088/1742-6596/664/7/072035.

[126] Martin Ester, Hans-Peter Kriegel, Jörg Sander, and Xiaowei Xu. A density-based algorithm for discovering clusters in large spatial databases with noise. In *Proceedings of the Second International Conference on Knowledge Discovery and Data Mining*, KDD'96, page 226–231. AAAI Press, 1996. doi:10.5555/3001460.3001507.

[127] Leandro A. F. Fernandes and Manuel Menezes de Oliveira Neto. Real-time line detection through an improved hough transform voting scheme. *Pattern Recognit.*, 41:299–314, 2008. doi:10.1016/j.patcog.2007.04.003. URL https://api.semanticscholar.org/CorpusID:5996185.

[128] Mattias Ohlsson, Carsten Peterson, and Alan L. Yuille. Track finding with deformable templates — the elastic arms approach. *Computer Physics Communications*, 71(1):77–98. ISSN 0010-4655. doi:10.1016/0010-4655(92)90074-9. URL https://www.sciencedirect.com/science/article/pii/0010465592900749.

[129] R. Krishnapuram and J.M. Keller. A possibilistic approach to clustering. *IEEE Transactions on Fuzzy Systems*, 1(2):98–110, 1993. doi:10.1109/91.227387.

[130] Miin-Shen Yang and Kuo-Lung Wu. Unsupervised possibilistic clustering. *Pattern Recognition*, 39(1):5–21. ISSN 0031-3203. doi:https://doi.org/10.1016/j.patcog.2005.07.005. URL https://www.sciencedirect.com/science/article/pii/S0031320305002943.

[131] Jianming Bian, Hongyue Duyang, and Alexander Radovic. Blessing package for Neutrino-Electron Scattering and Coherent Pi0. NOVA Document 13862. URL https://nova-docdb.fnal.gov/cgi-bin/sso/ShowDocument?docid=13862. NOvA internal document.

[132] Nicholas Jacob Raddatz. *Measurement of Muon Neutrino Disappearance with Non-Fiducial Interactions in the NOνA Experiment.* PhD thesis, Minnesota U., 2016.

[133] Michael David Baird. *An Analysis of Muon Neutrino Disappearance from the NuMI Beam Using an Optimal Track Fitter.* PhD thesis, Indiana U., 2015.

[134] G. Lutz. Optimum track fitting in the presence of multiple scattering. *Nuclear Instruments and Methods in Physics Research Section A: Accelerators, Spectrometers, Detectors and Associated Equipment*, 273(1):349–361. ISSN 0168-9002. doi:https://doi.org/10.1016/0168-9002(88)90836-4. URL https://www.sciencedirect.com/science/article/pii/0168900288908364.

[135] Brian Rebel. Window tracking algorithm for cosmic ray muons. NOVA Document 15977-v1. URL https://nova-docdb.fnal.gov/cgi-bin/sso/ShowDocument?docid=15977. NOvA internal document.

[136] Christian Szegedy, Wei Liu, Yangqing Jia, Pierre Sermanet, Scott Reed, Dragomir Anguelov, Dumitru Erhan, Vincent Vanhoucke, and Andrew Rabinovich. Going Deeper with Convolutions. *arXiv e-prints*, art. arXiv:1409.4842. doi:10.48550/arXiv.1409.4842.

[137] A. Aurisano, A. Radovic, D. Rocco, A. Himmel, M.D. Messier, E. Niner, G. Pawloski, F. Psihas, A. Sousa, and P. Vahle. A Convolutional Neural Network Neutrino Event Classifier. *JINST*, 11(09):P09001, 2016. doi:10.1088/1748-0221/11/09/P09001.

[138] Fernanda Psihas. Measurement of long baseline neutrino oscillations and improvements from deep learning. 1 2018. doi:10.2172/1437288. URL https://www.osti.gov/biblio/1437288.

[139] Prabhjot Singh. *Extraction of Neutrino Oscillation Parameters using a Simultaneous Fit of ν_μ Disappearance and ν_e Appearance data with the NOvA Experiment.* PhD thesis, University of Delhi, Dept. of Physics and Astrophysics, India, Delhi U., 9 2019.

[140] Ryan J. Nichol. Fibre brightness from cosmic muon data. NOVA Document 34909. URL https://nova-docdb.fnal.gov/cgi-bin/sso/ShowDocument?docid=34909. NOvA technical note.

[141] Prabhjot Singh. Attenuation Calibration of the NOvA Detectors. In *The 38th International Conference on High Energy Physics (ICHEP 2016)*, 2024. URL https://nova-docdb.fnal.gov/cgi-bin/sso/ShowDocument?docid=15840. (cited on 03.2024).

[142] E. Aprile et al. Excess electronic recoil events in XENON1T. *Phys. Rev. D*, 102: 072004, . doi:10.1103/PhysRevD.102.072004.

[143] E. Aprile et al. Search for New Physics in Electronic Recoil Data from XENONnT. *Phys. Rev. Lett.*, 129:161805, . doi:10.1103/PhysRevLett.129.161805.

[144] M. Atzori Corona, W. M. Bonivento, M. Cadeddu, N. Cargioli, and F. Dordei. New constraint on neutrino magnetic moment and neutrino millicharge from LUX-ZEPLIN dark matter search results. *Phys. Rev. D*, 107:053001. doi:10.1103/PhysRevD.107.053001.

[145] M. Agostini et al. Limiting neutrino magnetic moments with Borexino Phase-II solar neutrino data. *Phys. Rev. D*, 96:091103. doi:10.1103/PhysRevD.96.091103.

[146] Amir N. Khan. Light new physics and neutrino electromagnetic interactions in XENONnT. *Physics Letters B*, 837:137650. ISSN 0370-2693. doi:10.1016/j.physletb.2022.137650. URL https://www.sciencedirect.com/science/article/pii/S0370269322007845.

[147] K. S. Babu, Sudip Jana, and Manfred Lindner. Large Neutrino Magnetic Moments in the Light of Recent Experiments. *JHEP*, 10:040. doi:10.1007/JHEP10(2020)040.

[148] L. B. Auerbach et al. Measurement of electron-neutrino electron elastic scattering. *Phys. Rev. D*, 63:112001. doi:10.1103/PhysRevD.63.112001.

[149] D. A. Krakauer et al. Limits on the neutrino magnetic moment from a measurement of neutrino - electron elastic scattering. 252:177–180. doi:10.1016/0370-2693(90)91100-P.

[150] L. A. Ahrens et al. Determination of electroweak parameters from the elastic scattering of muon neutrinos and antineutrinos on electrons. *Phys. Rev. D*, 41: 3297–3316, Jun 1990. doi:10.1103/PhysRevD.41.3297.

[151] P. Vilain et al. Experimental study of electromagnetic properties of the muon-neutrino in neutrino - electron scattering. *Phys. Lett. B*, 345:115–118, 1995. doi:10.1016/0370-2693(94)01678-6.

[152] Biao Wang. *Muon-Neutrino Electron Elastic Scattering and a Search for the Muon-Neutrino Magnetic Moment in the NOvA Near Detector.* PhD thesis. URL https://scholar.smu.edu/hum_sci_physics_etds/1.

[153] Wenjie Wu and Yiwen Xiao. Constraint of the Integrated Neutrino Flux from Neutrino-Electron Elastic Scattering in the NOvA Near Detector. NOVA Document 56383. URL https://nova-docdb.fnal.gov/cgi-bin/sso/ShowDocument?docid=56383. NOvA technical note.

[154] Athula Wickremasinghe, Wenjie Wu, and Yiwen Xiao. Status of the Measurement of Neutrino-Electron Elastic Scattering in the NOvA Near Detector. In *Neutrino 2022*. URL https://indico.kps.or.kr/event/30/contributions/738/.

[155] Barnali Brahma, Tyler Horoho, and Mu Wei. TechNote: Light Dark Matter Search with NOvA Near Detector. NOVA Document 59439. URL https://nova-docdb.fnal.gov/cgi-bin/sso/ShowDocument?docid=59439. NOvA technical note.

[156] Carlo Giunti and Alexander Studenikin. Neutrino electromagnetic interactions: A window to new physics. *Rev. Mod. Phys.*, 87:531–591, Jun 2015. doi:10.1103/RevModPhys.87.531.

[157] Boris Kayser. Majorana neutrinos and their electromagnetic properties. *Phys. Rev. D*, 26:1662–1670, Oct 1982. doi:10.1103/PhysRevD.26.1662.

[158] José F. Nieves. Electromagnetic properties of majorana neutrinos. *Phys. Rev. D*, 26:3152–3158, Dec 1982. doi:10.1103/PhysRevD.26.3152.

[159] Carlo Giunti, Julieta Gruszko, Benjamin Jones, Lisa Kaufman, Diana Parno, and Andrea Pocar. Report of the Topical Group on Neutrino Properties for Snowmass 2021. 9 2022.

[160] Nicole F. Bell, Mikhail Gorchtein, Michael J. Ramsey-Musolf, Petr Vogel, and Peng Wang. Model independent bounds on magnetic moments of Majorana neutrinos. *Phys. Lett. B*, 642:377–383, 2006. doi:10.1016/j.physletb.2006.09.055.

[161] Nicole F. Bell, Vincenzo Cirigliano, Michael J. Ramsey-Musolf, Petr Vogel, and Mark B. Wise. How magnetic is the Dirac neutrino? *Phys. Rev. Lett.*, 95:151802, 2005. doi:10.1103/PhysRevLett.95.151802.

[162] P. Vogel and J. Engel. Neutrino electromagnetic form factors. *Phys. Rev. D*, 39: 3378–3383, Jun 1989. doi:10.1103/PhysRevD.39.3378.

[163] E. Valencia et al. Constraint of the MINERνa medium energy neutrino flux using neutrino-electron elastic scattering. *Phys. Rev. D*, 100:092001, Nov 2019. doi:10.1103/PhysRevD.100.092001.

[164] Erin Ewart. Primary and Secondary Vertexing Update for February 2024 Collaboration Meeting. NOVA Document 61190, February 2024. URL https://nova-docdb.fnal.gov/cgi-bin/sso/ShowDocument?docid=61190. NOvA internal document.

[165] Leonidas Aliaga, Derek Doyle, Matthew Judah, Norm Buchanan, Linda Cremonesi, Mat Muether, and Jon Paley. Measurement of the Double-Differential Inclusive Electron-Neutrino Charged-Current Cross Section in the NOvA Near Detector. NOVA Document 37668, 04 2020. URL https://nova-docdb.fnal.gov/cgi-bin/sso/ShowDocument?docid=37668. NOvA technical note.

[166] Andreas Hoecker, Peter Speckmayer, Joerg Stelzer, Jan Therhaag, Eckhard von Toerne, and Helge Voss. TMVA: Toolkit for Multivariate Data Analysis. *PoS*, ACAT:040, 2007.